University College London

Department of Chemistry

Disorder in Superconductors in Reduced Dimensions

Author:

Nicolas George Nicolaou Constantino

Supervisor:

Prof. Paul A. Warburton

April 24, 2016

Thesis submitted in partial fulfilment of the requirements for the Degree of Doctor of Engineering of University College London

I, Nicolas George Nicolaou Constantino, confirm that the work presented in this thesis is my own. Where information has been derived from other sources, I confirm that this has been indicated in the thesis.

Abstract

Superconducting nanowires have been identified as dual elements to the Josephson junction. This duality is attributed to the existence of quantum phase slip (QPS) phenomena, where the magnitude of the superconducting order parameter fluctuates to zero. This has provided scope for equivalents to well-established applications of Josephson physics, such as a quantum current standard. Existing literature indicates an influence of disorder on the rate of QPS events in superconductors, but few studies have looked specifically at quantifying this disorder as dimensions are reduced for QPS materials.

We have investigated disorder in two superconductors of particular significance for QPS phenomena, Nb_xSi_{1-x} and NbN. We have engineered compositions of these materials and grown thin-films using magnetron sputter deposition. We developed a novel top-down nanowire fabrication technique to overcome factors limiting the minimum widths achievable using standard lift-off techniques and used this method to reduce our films to nanowires for the investigation of dimensional effects.

We present low-temperature transport behaviour in our superconducting thin-films and demonstrate the dependence of the critical temperature on both the sheet resistance and film thickness. These illustrate a trend in disorder from which we extract the Finkel'stein disorder parameter γ, the mean free path, and the BCS and Ginzburg-Landau coherence lengths in our films. As films are reduced to nanowires, we show the influence of noise on measurements of superconductivity in nanowires and demonstrate the importance of filtering. We demonstrate that the relationship between the critical temperature and dimension is also observable for a reduction in width of the superconductor when reduced to nanowire dimensions.

Finally, using characteristics we have extracted from our investigations, we present a feasibility study on the integration of these nanowires into a voltage-biased QPS junction circuit, dual to the current-biased Josephson junction. Using QPS

theory, we predict how our materials are expected to behave in such a circuit and present measurements of a prototype device.

Acknowledgements

I would like to express my gratitude to my supervisor, Prof. Paul Warburton, who offered me the opportunity to take on this project and who guided me over the course of this doctorate. I thank him not only for introducing me to the exciting field of nanoscale superconductors, but also for welcoming me as part of his group and encouraging a close-knit and friendly research environment to work in.

I am very grateful to have worked with my fellow members and friends in the QPS research team, Dr Jon Fenton who was a constant source of knowledge and support throughout, Mr Christopher Nash a truly calming and steadfast co-researcher at all times, and Dr Jonathan Burnett from whom I learnt a great deal about low temperature physics and the virtues of salted coffee.

I thank Dr Ed Romans for his encouragement and many an enlightening discussion (on matters scientific and otherwise) and Prof. Helen Hailes, Prof. Nora de Leeuw, Prof. Ivan Parkin and Dr Zhimei Du for coordinating the EngD program and their invaluable support until the end.

It has been a true privilege to work alongside, learn from and form friendships with my colleagues at the LCN, both in my group and beyond: Dr Arnaud Blois to whom I am indebted for his constant drive and relentless encouragement; Dr Marion Sourribes for her lessons in determination and vigour; Dr Ivan Isakov for his constant creativity and inspiration; Drs Jaqueline Edge, Nuruzzaman Noor, Atahl Nathanson and Matthew Shiers who began this process alongside me and remained close friends throughout; former PhD students Drs Huan Wang and Yuji Suzuki; the members of the semiconductor subgroup, Drs James Aldous and James Sagar, and soon-to-be-Drs Maddison Coke and Oscar Kennedy, for teaching me 'Zen and the Art of Vacuum System Maintenance'; and my wonderful write-up siblings (the very-soon-to-be-Drs) Thuong Thuong Nguyen, Nuno Braz, and Abubakar Adan, Mustafa Osman and Timothy Wootton all of whom provided the companionship that made the long days and late nights enjoyable.

I would also like to extend a special thanks to the wonderful members of the UCL Quantum Spin Dynamics group, headed by Prof. John Morton, who offered me the opportunity to use their dilution refrigerator and adopted me into their group: Drs Matias Urdampilleta, Jarryd Pla, Gary Wolfowicz and Cheuk Lo alongside the group's PhD students all of whom were willing to share their knowledge (and Friday evening drinks) and have become my very good friends.

In addition, I would like to express my deep gratitude to the members of the LCN Cleanroom, Steve Etienne and his team Mike Cresswell, Suguo Huo, Vijay Krishnan, Dave Malone and Dr Richard Thorogate for their constant efforts to keep the equipment running and research progressing.

Finally, my deepest gratitude goes to all my family, to my parents George and Mary, to my siblings Fanos and Christina and Ross Breakwell, for their unending love and encouragement, for their limitless support throughout life and in particular this doctorate, and for always believing that I could.

I dedicate this thesis to them.

Contents

List of Figures

Chapter 1

Superconductivity & Josephson Junctions

1.1 Introduction

Superconducting nanowires are structures of superconducting material measuring below 1 μm in width and thickness, whilst having a length that is long relative to the other two dimensions. The wires may be grown as standalone structures, or may be patterned from larger areas of superconducting material. They differ from constriction weak-links in that their length exceeds the Ginzburg Landau coherence length such that the supercurrent is guided through the wire and cannot tunnel across the gap bridged by the wire between the bulkier superconducting contacts, called banks.

Presently, the most popular use of superconducting nanowires is in single-photon detection [1, 2] where they are patterned as long meanders that form pixel structures for detection of cosmic radiation. These are subsequently cooled down and current biased close to their critical current. Photons incident on the pixel provide enough energy to break Cooper pairs resulting in a momentary hot spot and a measurable finite resistance.

Potential novel applications of superconducting nanowires that have been

theorised or are currently under development include a quantum based current standard [3], nanowire sensors dual to SQUIDs [4] and the Mooij-Harmans flux qubit, which was recently demonstrated by Astafiev *et al.* [5].

Each of these applications rely on the occurence of quantum phase slip (QPS) events. In superconducting materials, constant quantum fluctuations exert their influence on the amplitude of the wavefunction. In bulk, the effects of these fluctuations average out and have little impact on the behaviour of the superconductor. As the cross-sectional dimensions of superconductors are reduced towards the coherence length of the material and the 1D regime, these fluctuations are sufficient to momentarily reduce the amplitude of the order parameter to zero and drive the area of effect in the superconductor into the normal state. This break in superconductivity results in a slip of 2π in the phase of the wavefunction.

This phenomenon is the dual to the Josephson tunnelling effect, and as a result opens up a new area of investigation based on the reapplication of the physics related to Josephson junctions to superconducting nanowire QPS junctions. A key element to understanding QPS phenomena and the development of these promising QPS applications is the characterisation of the level of disorder as it is has been proposed as an important factor affecting QPS phenomena [5].

The present thesis will investigate the changes observed in the low temperature transport characteristics of two superconductors, Nb_xSi_{1-x} and NbN, as they are patterned down from bulk to thin films and subsequently into nanowire structures in order to assess the level of disorder and how it scales as dimensions are reduced. We subsequently investigate the feasibility of the incorporation of such structures as the active element one of these novel applications: the voltage biased QPS junction proposed by Mooij *et al.* [3].

We begin by providing an introduction to the fundamental physical theory and principles behind superconductivity in Section 1.2 of this chapter. This will form the foundations on which the studies presented in subsequent chapters will be built.

In Chapter 2 we review the reported state of the art in the fields of disorder in

superconductors and superconducting nanowires. Investigation into the interplay between disorder and dimension has already begun within the field of superconducting thin-films [6, 7, 8]. It has been demonstrated that the impact of disorder increases as the dimensions of superconducting structures are reduced from bulk material to thin-films [9, 10, 11, 12]. Critically in such delicate systems as nanowires, the role of disorder can be expected to play a more dominant role in wire behaviour as the dimensions of nanowires approach the Ginzburg-Landau coherence length of the material, amongst other limits. As such, it is of particular interest to better understand how disorder manifests itself in the superconducting characteristics of thin-film and nanowire systems if we are to create a range of reliably reproducible and predictable technologies using superconducting nanowires. The aim of this thesis is, therefore, to fabricate films and nanowires from superconducting materials and study this relationship and any related phenomena.

In Chapter 3 we discuss potential candidates of suitable superconducting materials for the study and our reasons for the final selections. We also consider design and process optimisation for the various stages of film and nanowire fabrication and measurement preparation, and include descriptions of fabrication and measurement equipment. The study into disorder and thin superconducting film structures is presented in Chapter 4. We use existing models to extract characteristic parameters and use these to demonstrate the relationship between disorder and dimension in our films. We focus particularly on Finkel'stein's model [6] which has been applied by fellow groups to thin films fabricated from other superconducting materials and present the first application to our knowledge in $Nb_{0.3}Si_{0.7}$ and NbN materials.

Upon reduction to nanowire dimensions, existing studies on superconductors have widely reported broadened superconducting transitions, finite resistances below T_c [13, 12, 14] and insulating behaviour [9, 13, 15]. A large body of early studies on nanowires was focussed on using thermal models to explain the behaviour near T_c. The behaviour of these wires closer to zero has proved, however, more challenging to model. The dominant mechanisms to which finite resistances are believed to

be quantum in nature [11]. A particularly strong theory is based on the idea of slips in the phase of the order parameter caused by quantum fluctuations. Now supported by experimental work [5, 16], this phenomenon is believed to contribute, if not be the dominant cause of, finite resistances as the temperature tends toward zero. Despite this, there have been only limited reports on quantifying disorder and its contribution to these phenomena in superconducting nanowire systems. In Chapter 5 we present the development of a novel and repeatable fabrication process for the top-down fabrication of nanowire structures from superconducting thin films, overcoming the challenges faced when using standard processes. We present the behaviour of these wires at low temperature in Chapter 6 and consider how it can be used to describe disorder in these wires.

In Chapter 7 we study the feasibility of the use of our superconducting nanowires for the observation of the quantum phase slip phenomena. This is based principally on the integration of superconducting nanowires into a circuit to create an exact dual to the Josephson Shapiro experiment. Using the parameters that we have gathered throughout this thesis for our materials alongside our recent work on high resistance CrO_x thin-film resistors [17], we model the relationships of the circuit elements to the characteristic energies and frequencies in the system, and use this to create our design. Finally we present a prototype of the realised circuit itself, characterised at 30 mK.

We conclude our work in Chapter 8 and discuss further possible work in the area, including wire network designs to increase yield and ways in which to maximise phase slip observations by tuning disorder.

1.2 Physics of Superconductivity

The theory of QPS that will be described in more detail in Chapter 2, is based on the fundamental physics behind superconductivity, which we introduce in the following sections.

1.2.1 Fundamentals of superconductivity

In the early 20th century, interest in the resistive behaviour of pure metals at low temperature led Dutch physicist Heike Kamerlingh Onnes to work on the liquefaction of helium as a cryogen for his investigation. His work was focussed on the proof of one of several schools of thought at the time which stated that the resistivity of a pure metal would tend to zero as its temperature tended towards absolute zero. The basis of this hypothesis was that, as the temperature was reduced, phonon activity would reduce in the lattice allowing free flow of electrons. Onnes successfully achieved liquefaction of helium and in 1911 during measurements of liquid mercury, a metal easy to purify due to its liquid phase, he observed a drop to zero in the resistivity of the material [18]. However, unlike his theoretical prediction, this transition was sharp instead of gradated. Further measurements identified a family of materials, at the time comprised solely of metals, that exhibited this behaviour. Onnes labelled this behaviour "superconductivity". His work on the liquefaction of helium and the investigation of the properties of matter at low temperatures was later recognised with the award of the Nobel Prize in Physics.

The phenomenon of superconductivity is the characteristic of selected materials to exhibit zero resistivity when cooled below a temperature threshold known as the material's critical temperature T_{c}. Since the first observation of the phenomenon, study in the field has led to the discovery of a range of related effects which will be discussed later in this section. These play a fundamental role, not only in many areas of low-temperature and quantum physics, but also in diverse applications ranging from medical imaging to superconducting magnetic energy storage devices for grid power.

Critical transition points In his continuing research, Onnes began looking at how superconductivity could be utilised in the production of high magnetic fields. On experimenting with superconducting solenoids, he quickly found that the magnetic field generated by the passage of sufficiently large supercurrent could

destroy superconductivity within the solenoid.

The results pointed to the existence of a critical magnetic field threshold, H_c, for superconductivity. In turn this field implied the existence of a third quantity, the critical current density, J_c. Much like the critical temperature, these limits are characteristic of the superconducting material.

In Figure 1.2 the three critical limits define a region within whose boundaries superconductivity is preserved. Outside this region, however, superconductivity is destroyed and the material behaves as a normal conductor with resistive characteristics.

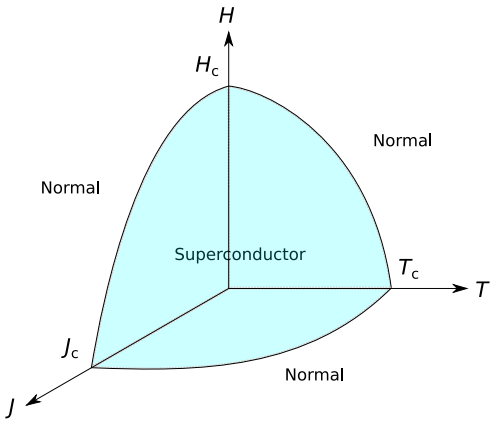

Figure 1.1: Phase diagram showing the fundamental critical transition points T_c, H_c and J_c in a superconductor along the axes of temperature T, magnetic field H and current density J. This characteristic accurately described superconducting materials, later identified as type I. A second range of superconductors, was identified years later due to its deviation from this behaviour. The difference between these two types of superconductor is discussed later in this chapter.

The Meissner-Ochsenfeld effect

In a perfectly conducting metal screening currents are induced at the surface of the material when an external magnetic field is applied. The resulting magnetic field generated in turn by these screening currents serves to counter the external field, causing it to decay exponentially at the surface. This ability to screen out external magnetic fields is known as diamagnetism.

The lengthscale of the field decay at the surface of these materials is described as the penetration depth, denoted λ. In superconductors, for a material with a superconducting electron density n_s, this depth is defined as $\lambda = \sqrt{m/\mu_0 n_s e^2}$ where μ_0 is the magnetic constant, m is the electron mass and e is the elementary charge. Provided that the external field is low enough, it will be completely cancelled by the induced fields and thus be excluded from within the superconductor. However, as the field is increased, superconductivity is destroyed when the field reaches the critical field limit H_c.

For years after the discovery of superconductivity, superconductors were thought of as perfect conductors, able to screen out externally applied fields whilst superconducting. According to the classical model of a perfect conductor, magnetic flux present within the material at the time of transition to the superconducting phase could be frozen inside. However, in 1933 Walther Meissner and Robert Ochsenfeld found that contrary to these expectations, any magnetic flux within a superconductor in its normal state would subsequently be expelled from the interior on cooling through T_c. This property became known as the Meissner effect.

The London equations

In 1935, Fritz and Heinz London proposed two equations that explain the Meisner effect in superconductors. The relationship for the penetration depth λ given above may be found through the application of the Drude Model for an electron in an applied electric field $\mathbf{E}$, with charge e, mass m and speed $\mathbf{v_s}$.

The motion of this electron may be described by the equation $m\,\mathrm{d}\mathbf{v_s}/\mathrm{d}t = e\mathbf{E} - m\,\mathbf{v_s}/\tau$. The time constant between collisions of the electron with fixed ions τ may be taken as infinite for a superconductor which reduces the second term in this equation to a negligible value. To find the first of the London equations we use this result and take the derivative of the current density given by $\mathbf{J_s} = n_s e \mathbf{v_s}$, with respect to time, giving:

$$\frac{d\mathbf{J_s}}{dt} = \frac{n_s e^2}{m}\mathbf{E} \tag{1.1}$$

Arranging the first London Equation in terms of the field $\mathbf{E}$, the result may be substituted into the Maxwell-Faraday equation $d\mathbf{B}/dt = -\nabla \times \mathbf{E}$ to give the derivative of the magnetic field applied to the superconductor with respect to time:

$$\frac{d\mathbf{B_s}}{dt} = -\frac{m}{n_s e^2}\nabla \times \frac{d\mathbf{J_s}}{dt} \tag{1.2}$$

where n_s is the density of the superconducting carriers, pairs of electrons or Cooper pairs as will be explained.

Using Maxwell's corrected version of Ampere's law, $\nabla \times \mathbf{H} = \mathbf{J} + d\mathbf{D}/d\mathbf{t}$, we assume that the displacement current caused by fixed ions and electrons in the lattice $d\mathbf{D}/d\mathbf{t}$ is negligible compared to the supercurrent density. Assuming that the relative magnetic permeability of superconductors is 1, the relationship may then be rewritten in the form $\nabla \times \mathbf{B} = \mu_0\mathbf{J}$. Taking the derivative gives $\nabla \times d\mathbf{B}/dt = \mu_0 d\mathbf{J}/dt$. This may then be used in conjunction with the relationship for the penetration depth λ to arrange Equation 1.2 as

$$-\frac{1}{\lambda^2}\frac{d\mathbf{B}}{dt} = \nabla \times \nabla \times \frac{d\mathbf{B}}{dt}. \tag{1.3}$$

Since $\nabla.\mathbf{B} = 0$, $\nabla \times \nabla \times d\mathbf{B}/dt = -\nabla^2 d\mathbf{B}/dt$, and Equation 1.3 may be reduced to:

$$\nabla^2\frac{d\mathbf{B}}{dt} = \frac{1}{\lambda^2}\frac{d\mathbf{B}}{dt}. \tag{1.4}$$

The solution to this equation at the boundaries of a superconductor gives a vanishing exponential dependence of the time dependent magnetic field, described by $d\mathbf{B}/dt = d\mathbf{B_s}/dt \exp^{-x/\lambda}$, where $\mathbf{B_s}dt$ represents the applied magnetic field variation and x represents the distance from the surface of the superconductor.

As discussed earlier, experiments by Meissner and Oschenfeld found that the

field was not only screened but actually expelled from within the superconducting material [19]. London and London therefore postulated that the relationship in Equation 1.4 held true for time-independent fields in the material as well, leading to the result that $\nabla^2\mathbf{B} = 1/\lambda^2 \times \mathbf{B}$ and ultimately the second London equation [20]:

$$\nabla \times \mathbf{J_s} = -\frac{n_s e^2}{m}\mathbf{B}. \tag{1.5}$$

London and London thus successfully deduced that even time-independent fields were excluded from the superconductor bulk under this model, finally providing an explanation for the Meissner effect.

The Ginzburg-Landau theory

In 1950 Ginzburg and Landau proposed a phenomenological theory to describe the macroscopic behaviour of superconductivity [21]. The Ginzburg-Landau theory was later shown to be derivable as limiting case of the BCS theory by Lev Gorkov [22]. It provides a less complicated way of describing phenomena in the temperature range near T_c for slow variations of the order parameter ψ and the magnetic vector potential $\mathbf{A}$.

The theory was based on observations of phase transitions in liquid helium [23]. The transition from helium I to helium II is considered to be second order due to the continuity in the first derivative of the Gibbs free energy in the system. Landau put forward a theory for second order phase transitions introducing the concept of an order parameter ψ for systems exhibiting such transitions [24]. He predicted that near the phase transition, the order parameter will be zero (indicating disorder) on the high temperature side of the transition and non-zero (indicating an ordered phase) in the low temperature side.

Ginzburg and Landau demonstrated a theoretical observation of such a transition in the dependence of the penetration depth on temperature as part of their theory and introduced a complex wave function for the order parameter ψ in super-

conducting systems. In the case of superconductors, the order parameter describes the density of carriers or Cooper pair by $n_{\mathrm{s}} = |\psi(x)|^2$. For a superconductor close to its critical temperature, with effective electronic charge $e^* = 2e$ and effective electronic mass $m^* \approx 2m$, the order parameter parameter is small enough to obtain a series expansion of the free energy density in the system f given by:

$$f = f_{\mathrm{n0}} + \alpha|\psi|^2 + \frac{\beta}{2}|\psi|^4 + \frac{1}{2m^*}\left|\left(\frac{\hbar}{i}\nabla - e^*\mathbf{A}\right)\right|^2. \tag{1.6}$$

Here the α and β are coefficients related to the effective penetration depth $\lambda_{\mathrm{eff}} = \sqrt{m^*/\mu_0|\psi|^2 e^{*2}}$ and critical field H_{c}. This form of the effective penetration depth is similar to the London penetration depth λ_L but can be seen to vary with the density of carriers. This relationship does not apply for superconductors in which the mean free path l is shorter than the BCS coherence length ξ_0 (or $\xi_0 > l$), known as the "dirty limit", in which case the effective penetration depth is described by the relation:

$$\lambda_{\mathrm{eff}} = \lambda_{\mathrm{L}}(T)\sqrt{1 + \frac{\xi'}{l}} \tag{1.7}$$

The coherence length parameter ξ' here varies with temperature taking the value ξ_0 for $T = 0$ and $0.75\xi_0$ near the critical temperature T_{c}. Using λ_{eff}, the Ginzburg-Landau theory defines the coefficients α and β to be [25]:

$$\alpha(T) = -\frac{2\mu_0 e^2}{m^* 4\pi} H_{\mathrm{c}}^2(T)\lambda_{\mathrm{eff}}^2(T) \approx \alpha_0\left(\frac{T}{T_{\mathrm{c}}} - 1\right) \tag{1.8}$$

$$\beta(T) = \frac{\mu_0^2 e^4}{2m^*\pi^2} H_{\mathrm{c}}^2(T)\lambda_{\mathrm{eff}}^4(T) \approx \beta_0 \tag{1.9}$$

for the range where T is close to T_{c}. Here, e and m have their free electron values. For $T > T_{\mathrm{c}}$ α is positive, $|\psi|^2$ is zero and the free energy density of the system f_{n0} is at its minimum. Where $T < T_{\mathrm{c}}$ α takes on a negative value and $|\psi|^2 = -\alpha/\beta$.

The superconducting system will adapt the configuration of its wavefunction

where perturbations such as fields, currents or gradients are present or absent, in order to minimise the free energy in the system. For the case where perturbations are present, the integral of the free energy (Equation 1.6) can be reduced to obtain the Ginzburg-Landau differential equations [25]:

$$\alpha\psi + \beta|\psi|^2\psi + \frac{1}{2m^*}\left(\frac{\hbar}{i}\nabla - e^*\mathbf{A}\right)^2\psi = 0 \tag{1.10}$$

$$J = \frac{e^*}{m^*}|\psi|^2\left(\hbar\nabla\psi - e^*\mathbf{A}\right). \tag{1.11}$$

Where a magnetic field is not present and $\mathbf{A} = 0$, we may take ψ from the differential relation for the free energy in Equation 1.10 to have spatially independent phase. Normalising the wavefunction by setting $f = \psi/\psi_\infty$ where $\psi_\infty^2 = -\alpha/\beta$, we can reduce the equation to:

$$\frac{\hbar^2}{2m^*|\alpha|}\frac{\mathrm{d}^2 f}{\mathrm{d}x^2} + f - f^3 = 0. \tag{1.12}$$

It is at this stage that Ginzburg-Landau introduces the characteristic length $\xi(T)$, known as the Ginzburg-Landau (GL) coherence length. This is equivalent to the square root of the coefficient of the second order derivative in Equation 1.12:

$$\xi(T) = \sqrt{\frac{\hbar^2}{2m^*|\alpha|}} = \sqrt{\frac{\Phi_0}{2\sqrt{2}H_c(T)\lambda_{eff}(T)}} \tag{1.13}$$

where Φ_0 is the flux quantum given by [25]:

$$\Phi_0 = \frac{h}{2e} = 2.068 \times 10^{-15}\,\mathrm{Wb}. \tag{1.14}$$

Substituting Equation 1.13 into Equation 1.12 the resulting equation may be rewritten:

$$\xi(T)^2\frac{\mathrm{d}^2 f}{\mathrm{d}x^2} + f - f^3 = 0. \tag{1.15}$$

It should be noted that the GL coherence length and the BCS coherence length are not the same entity. They are related through the flux quantum by $\Phi_0 = \sqrt{2/3}\pi^2\xi_0\lambda_{\mathrm{L}}(0)H_{\mathrm{c0}}$. The BCS theory is used to attain two approximations for the temperature dependence of the GL coherence length. These are defined for superconductivity in the clean and dirty limits as:

$$\xi(T) = 0.74\frac{\xi_0}{\sqrt{1-T/T_{\mathrm{c}}}} \text{ for the clean limit, where } l \gg \xi_0 \tag{1.16}$$

$$\xi(T) = 0.855\sqrt{\frac{\xi_0 l}{1-T/T_{\mathrm{c}}}} \text{ for the dirty limit, where } l \ll \xi_0. \tag{1.17}$$

To prevent confusion between notation in this thesis, we denote the GL coherence length as ξ_{GL}, and assume that the parameter's temperature dependence need not be explicitly indicated in the notation.

The BCS theory of superconductivity

In 1957 Bardeen, Cooper and Schrieffer published the first microscopic theory of superconductivity able to describe the observations made experimentally, also known as the BCS Theory [26]. The theory analysed the phenomenon of superconductivity using quantum mechanics, and built on Fröhlich's theory that superconductivity was related to electron-phonon interactions [27]. An in depth treatment of the theory is beyond the scope of this thesis; however we will present a summary of the fundamentals here.

The theory proposed that the superconducting phenomenon relied on the existence of bound pairs of electrons, known as Cooper pairs. Though two electrons mutually repel each other due to the Coulomb interaction, it was suggested that below T_{c}, this repulsive interaction could be overcome by a mutually attractive pairing interaction.

Cooper demonstrated that the pairing process was due to the mutual exchange of these virtual phonons between the two respective electrons. For a pair of electrons,

in initial states $\mathbf{k_1}$ and $\mathbf{k_2}$, if the electron in state $\mathbf{k_1}$ were to emit a phonon $\mathbf{q}$ it would scatter into a state $\mathbf{k_1'}$. Should the second electron absorb the phonon it would also change from state $\mathbf{k_2}$ to state $\mathbf{k_2'}$. Again, the momentum must be conserved and so $\mathbf{k_1} + \mathbf{k_2} = \mathbf{k_1'} + \mathbf{k_2'} = \mathbf{K}$, where $\mathbf{K}$ represents the total momentum of the pair. Cooper showed that the interaction between a pair of electrons in a metal at low temperature could result in a weak attractive force. Provided this net attractive potential energy, $-U_{\text{ph}}$, exceeds the Coulombic repulsive energy, U_{rep}, i.e. that $-U_{\text{ph}} + U_{\text{rep}} < 0$, a bond between the two electrons could form.

The conditions for this bond arise when the first electron's state transition perturbs the lattice [28]. The nearby ions crowd in on the electron, surrounding it in a cloud of positive charge. This distorted, positively charged lattice serves both to attract a second electron and overcome the Coulombic repulsive energy U_{rep}. Thus, two electrons with momentum $\mathbf{k}$ and $-\mathbf{k}$ become bound as a single pair.

The BCS theory also showed that there is a characteristic distance at which this bond between electrons may occur, known as the coherence length, ξ, that may extend to the micrometer range. As such, a Cooper pair does not behave as a point particle. Indeed if the pair encounters a non-superconducting defect that is smaller than the size of the pair itself, superconductivity will not be destroyed as the pair's phase coherence will be maintained across the defect. This allows superconductivity to exist even in the presence of disorder.

Whilst the individual electrons that form a pair must obey the Pauli exclusion principle, Cooper pairs themselves are bosons and thus do not. Within the separation between two electrons in a Cooper pair, other Cooper pairs may exist and their areas of influence overlap substantially. The overlap between the waves of the electrons in a pair and in turn between the waves of the different pairs, produces a coherence that results in what is known as the condensed state of the superconductor. The BCS theory describes the existence of a macroscopic quantum ground state, due to the existence of the electron pair interaction. As a result, it was shown that Cooper pairs in the superconductor can be described by a single

electron-pair wavefunction.

The significance of the pairing mechanism to the superconducting state in terms of this theory can now be considered. Electrical resistivity is caused by the scattering process that causes a change in the momentum of electrons, due to interactions with either phonons or lattice defects. The BCS theory suggested that the formation of electron pairs could give rise to a superconducting current due to the fact that if a phonon were to try to scatter one electron from state $\mathbf{k_1}$ to $\mathbf{k_2}$, the existence of a secondary phonon with the correct momentum would be necessary to simultaneously scatter the second electron from state $-\mathbf{k_1}$ to a state $-\mathbf{k_2}$. The probability of such an event occurring is extremely small, and thus the electron pair continues to travel through the lattice, unperturbed, unless the phonon energy is sufficient to separate the Cooper pair. In terms of energy, this represents an energetic interaction that is twice the size of the superconducting energy gap Δ between the condensed state and the excited quasipartical state.

It is for this reason that superconductivity is sustained at lower temperatures, where lattice vibrations are suppressed and the phonon energy is typically lower, reducing the number of high energy phonon interactions. Indeed Δ tends to its maximum as $T \to 0$. For classical superconductors that follow the BCS theory, the energy gap Δ is approximated by $\Delta(0)/k_{\mathrm{B}}T_{\mathrm{c}} = 1.764$ [25].

As $T \to T_{\mathrm{c}}$, the influence of thermal fluctuations increases with sample temperature, resulting in an increasing number of Cooper pairs becoming uncoupled. Close to T_{c} the influence of temperature gains significance and the energy gap may be approximated by [25]:

$$\frac{\Delta(T)}{\Delta(0)} \approx 1.74\sqrt{1 - \frac{T}{T_c}}. \tag{1.18}$$

As the temperature increases, the number of broken pairs will reach a significant threshold at the critical temperature T_{c}. At this point the magnitude of the energy gap Δ rapidly decreases and the material reverts to its normal state.

The energy gap may be used to provide the BCS coherence length by:

$$\xi_0 = \frac{\hbar \nu_{\mathrm{F}}}{\pi \Delta(0)} \tag{1.19}$$

where ν_{F} is the Fermi velocity for the respective material. This relationship holds true for pure materials, seen to be clean superconductors. We will later introduce equations for the estimation of the coherence length in disordered or dirty superconductors.

Characteristic coherence lengths

We have already introduced the Ginzburg-Landau and BCS coherence lengths, ξ_{GL} and ξ_0 respectively. Prior to the proposal of the BCS coherence length, Pippard [29] introduced another characteristic length for superconductivity. This length described the distance to which changes of a magnetic vector potential would affect the supercurrent [30]. An in-depth explanation of the relevance of the Pippard coherence length would go beyond the scope of its use in this thesis. This length was labelled ξ_0 and continues to be used as such in the literature. For our purposes and to avoid confusion, we will refer to the Pippard coherence length as ξ_{p}, while ξ_0 will be reserved to refer to the BCS coherence length.

Pippard proposed that only electrons within $k_{\mathrm{B}}T_{\mathrm{c}}$ of the Fermi energy and with momentum $\sim k_{\mathrm{B}}T_{\mathrm{c}}/\nu_{\mathrm{F}}$ make major contributions to the transition to superconductivity [25]. Using this uncertainty-principle argument he was able to predict that the value of ξ_{p} in a pure metallic superconductor could be estimated using:

$$\xi_{\mathrm{p}} = a\frac{\hbar \nu_{\mathrm{F}}}{k_{\mathrm{B}}T_{\mathrm{c}}} \tag{1.20}$$

where a denotes a constant, later approximated to 0.18.

As with the relationship between ξ_0 and ξ_{GL}, the ξ_{p} coherence length describes a different aspect of the superconducting phenomenon and must be distinguished from the others. ξ_{p} is independent of temperature whereas ξ_{GL} is temperature

dependent.

Although not directly related, the Pippard coherence length provides an important approximation of the BCS coherence length. It was shown that, since $\Delta(0) \approx k_{\mathrm{B}}T_{\mathrm{c}}$, applying this substitution into Equation 1.19 for ξ_0 gives a result similar to Equation 1.20. Indeed, at $T = 0$ the two lengths are equivalent with a small correction provided when the value of the prefactor in Equation 1.20 is set to $a = 0.18$. This give an approximation for the BCS coherence length in pure metals based on a corrected Pippard estimate to be:

$$\xi_0 = 0.18\frac{\hbar\nu_{\mathrm{F}}}{k_{\mathrm{B}}T_{\mathrm{c}}}. \tag{1.21}$$

The two types of superconductors

In the 1930s Shoenberg began examining the behaviour of very small superconducting particles. He found that for sufficiently sized particles magnetic flux penetration would occur in a significant fraction of the samples [31]. This was found to result in a reduction of the magnetic susceptibility and hence the sample exhibiting behaviour that was less diamagnetic than would be expected in larger samples. Others, such as London, noted this shift away from classical superconducting behaviour, with Shubnikov *et al.* reporting particular instances in alloys [32]. Superconductors were divided into two types; those exhibiting classical behaviour were labelled type I whilst the materials exhibiting this new behaviour came to be known as type II superconductors.

(i) Type I For the classical type I superconductor, the coherence length ξ is larger than the penetration depth λ. Here the transition between superconductivity and normal conductivity is observed when the critical field H_{c} is reached. Below this point, the Meissner effect excludes all magnetic fields from inside the bulk of the material.

(ii) Type II Abrikosov, expanding on the experimental observations by Shubnikov *et al.*, proposed that for type II superconductors the ratio λ/ξ exceeds

$\sqrt{2}/2$ [33]. The transition separates into two distinct phases phases, one where flux is completely excluded from the bulk (below a lower critical field H_{c1}) and one where it exists within regions of the superconducting material. Above H_{c1}, the formation of vortices of quantised flux $\Phi_0 = h/2e$ through the material allows the magnetic field to pass. These normal regions of conductance are screened from the superconducting bulk by the action of the currents set up by the magnetic field around the vortices. The number of vortices in the material increases as the applied external field increases until the point where the entire bulk is filled with vortices. The field at the point where the superconductor reverts to a normal conducting state is referred to as the upper critical field limit, denoted by H_{c2}.

1.2.2 The Josephson effect

In 1962, Josephson proposed that, as with individual electrons, electron pairs should be capable of tunnelling through a potential. He predicted that, for an appropriately sized barrier between two superconducting metals, the wave functions of the superstates on either side should have sufficient overlap that Cooper pairs could tunnel across the barrier, even where no bias was applied to the junction. His theory, later observed experimentally by Anderson *et al.* [34], remains one of the most fundamental contributions to the field of superconductivity and the structures in which the phenomenon could be observed became known as Josephson junctions (JJ).

Whilst this thesis presents investigations that focus on other superconducting structures, knowledge of the theory behind Josephson junctions will become useful in later chapters where we consider the similarities between Josephson junctions and superconducting nanowires. As we will discuss later, as the superconductors are confined to nanowire dimensions, their behaviour becomes dual to that of Josephson junctions.

Types of Josephson junctions

Josephson's proposal was initially a prediction for quantum mechanical tun-

nelling of Cooper pairs through a barrier layer. Physically this type of junction is know as a Superconductor-Insulator-Superconductor junction (SIS). As more instances of the Josephson effects were observed, it became clear that the effects applied, not just to barrier separation of superconducting electrodes, but in any case where two superconducting electrodes are separated by a weak link [25].

One such junction structure is where electrodes are separated by a thin normal metal layer, known as a Superconductor-Normal Metal-Superconductor (SNS) junction. Here the normal metal layer is made weakly superconducting by its proximity to the superconducting layers. A second type of junction where tunnelling of Cooper pairs is observed is a constriction in the superconductor bulk. Here, superconductivity is weakened in the region of the constriction and acts as a barrier. Such superconductors are known as Superconductor-constriction-Superconductor (ScS) junctions or popularly labelled micro and nanobridges due to the typical scale of the transverse dimensions of the constriction.

The Josephson equations

The Josephson effect may be used to describe four separate aspects of Cooper pair tunnelling. These are the dc Josephson effect, phase dependent Josephson inductance, the ac Josephson effect and the inverse ac Josephson effect. A fifth section is added to cover the subject of Shapiro steps and the Josephson voltage standard. We discuss each separately [35].

(i) Zero bias: The dc Josephson effect

In the dc case, Josephson predicted that for a junction where two superconducting electrodes are separated by a thin insulating barrier a dc supercurrent I_{s} will flow between the two electrodes, such that:

$$I_{\mathrm{s}} = I_c \sin\phi \tag{1.22}$$

where I_{c} is the maximum zero-voltage current the junction can support whilst maintaining a superconducting state, otherwise the junction critical current. In addition,

ϕ is the phase difference $\theta_2 - \theta_1$ between the wavefunctions of superconducting states either side of the barrier, whose time dependence is defined as:

$$\frac{d\phi}{d\mathrm{t}} = \frac{2e}{\hbar}V(\mathrm{t}). \tag{1.23}$$

Here V is the potential difference between the two electrodes.

This variation of this phase difference between the two sides of the junction is responsible for driving the supercurrent across the barrier in the absence of an applied external bias. Equations 1.22 and 1.23 are known as the Josephson equations.

(ii)Phase-dependent Josephson inductance

A Josephson junction behaves as a non-linear inductance that is phase-sensitive. The non-linear nature originates from the accumulation of a junction potential energy, known the Josephson energy, which will be discussed later in this section. The phase at $t = 0$ is ϕ_0, the corresponding current $I_0 = I_\mathrm{c}\mathrm{sin}\phi_0$ from Equation 1.22. If we consider small variations of the phase difference around ϕ_0 we obtain the relation $\mathrm{d}I = I_\mathrm{c}\mathrm{cos}(\phi_0)\mathrm{d}\phi$. Using Josephson's second relation in Equation 1.23, $\mathrm{d}\phi$ may be replaced and the relationship rearranged to get the junction voltage:

$$V = \frac{\hbar}{2eI_\mathrm{c}\mathrm{cos}\phi_0}\frac{dI}{dt}. \tag{1.24}$$

The voltage across an inductor L is known to take the form $V = L\mathrm{d}I/\mathrm{dt}$ [36]. By analogy, $L_\mathrm{J}(\phi_0) = \hbar/2eI_\mathrm{c}\mathrm{cos}\phi_0$ and the voltage across across the junction may be rewritten as $V = L_\mathrm{J}(\phi_0)dI/dt$.

The phase dependent junction inductance parameter $L_\mathrm{J}(\phi)$ is known as the Josephson inductance and may be written in either of the forms:

$$L_\mathrm{J}(\phi_0) = \frac{\hbar}{2eI_\mathrm{c}\mathrm{cos}\phi_0} = \frac{\Phi_0}{2\pi I_\mathrm{c}\mathrm{cos}\phi_0} \tag{1.25}$$

with the second form obtained using Equation 1.14.

(iii) Application of a dc Bias: The ac Josephson effect

In addition to the dc current induced across the junction by the phase difference between the two sides at zero applied bias, the Josephson effect may be used to consider the case of a junction under an applied bias. The ac equation relates to the flow of a sinusoidal or ac tunnelling current across a junction with an applied dc voltage V_{dc}.

Using Equation 1.23 we assume a dc voltage and take the integral for the range $0 \leq \mathrm{t}$. From this we obtain $\phi = \phi_0 + \frac{2e}{\hbar} V_{\mathrm{dc}} t$. The resulting current may be found by inserting this result into Josephson's first relation, Equation 1.22, and is described by:

$$I_{\mathrm{s}} = I_c \sin(\phi_0 + \omega_{\mathrm{J}} \mathrm{t}) \tag{1.26}$$

where the substitution $\omega_{\mathrm{J}} = 2eV_{\mathrm{dc}}/\hbar = 2\pi V/\Phi_0$ has been applied. As can be seen, the supercurrent varies sinusoidally at an amplitude I_{c}. Converting ω_{J} into Hz we obtain the frequency $f_{\mathrm{J}} = \omega_{\mathrm{J}}/2\pi = V/\Phi_0 = V2e/h = V \times (4.836 \times 10^{14})\,\mathrm{Hz}$ known as the Josephson frequency. For a dc voltage $V = 10\,\mu V$ we expect an oscillation frequency of 4.836 GHz. Thus a dc applied voltage drives an ac supercurrent that oscillates at a frequency of $1/\Phi_0$ times the applied voltage.

(iv) Application of an ac bias and the Shapiro spikes phenomenon: The inverse ac Josephson effect

We now consider the case where a Josephson junction is biased using a combined dc and ac voltage bias. Inserting $V = V_0 + V_{\mathrm{rf}} \cos(\omega_{\mathrm{rf}} t)$ into Equation 1.23 gives:

$$\phi = \phi_0 + \omega_{\mathrm{J,dc}} t + \frac{\omega_{\mathrm{J,rf}}}{\omega_{\mathrm{rf}}} \sin(\omega_{\mathrm{rf}} t). \tag{1.27}$$

where $\omega_{\mathrm{J,dc}} = 2eV_{\mathrm{dc}}/\hbar$ and $\omega_{\mathrm{J,rf}} = 2eV_{\mathrm{rf}}/\hbar$. Substituting this into Equation 1.22 and following manipulation using a harmonic expansion, the supercurrent may be described by:

$$I_{\rm s}(t) = I_{\rm c} \sum_{v=-\infty}^{v=+\infty} (-1)^v J_v \left(\frac{\omega_{\rm J,rf}}{\omega_{\rm rf}} \right) \sin(\phi_0 + (\omega_{\rm J,dc} + v\omega_{\rm J,rf})t). \qquad (1.28)$$

where v is an integer number. Thus the ac voltage results in a dc current response with amplitude set by the Bessel function J_v. Where the Josephson frequency is equal to a multiple of the ac frequency a supercurrent of $|I_{\rm s}| = I_{\rm J} J_v(\omega_{\rm J,rf}/\omega_{\rm rf})$ flows. This supercurrent manifests as spikes generated in the dc $I-V$ at a separation of $\mathrm{d}V = \hbar\omega_{\rm rf}/2e$ and are known as Shapiro spikes. At all other points a dc response of $|I_{\rm s}| = V_{\rm dc}/R$ will be seen, where R is the resistance of the junction.

(v) Shapiro steps and the Josephson voltage standard

If an ac bias current is applied to the same junction steps known as Shapiro steps become visible in the continuous $I-V$ for the junction. The precise nature of the Josephson frequency-voltage relationship $\omega_{\rm J} = 2eV/\hbar$ led Hamilton *et al.* [37] to create the highly accurate Josephson junction voltage standard. By matching the frequency of incident rf radiation with the Shapiro steps in a large array of Josephson (1480 pairs of junctions in the initial device), it is possible to define the quantity of one volt to an accuracy of ten parts per billion.

Modelling real junctions: The Resistively and Capacitively Shunted Junction (RCSJ) model and junction quality

The preceding theories predominantly apply to ideal case Josephson junctions. The RCSJ model was developed in order to describe real case, non-ideal weak-link and constriction junctions. Figure 1.2 shows the equivalent circuit of a Josephson junction using the RCSJ model. In a real junction, the presence of quasiparticle populations in tunnel junctions and bridge resistance in constriction junctions, adds a noise current $I_{\rm n}$ component that requires consideration. In addition, any changes in electric field will generate a displacement current $I_{\rm d}$. These currents are approximated in the model as the currents through a shunt capacitance and shunt resistance and are represented alongside the junction critical current $I_{\rm J}$ in the circuit diagram.

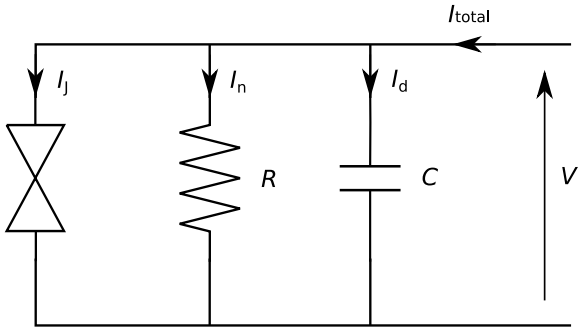

Figure 1.2: Equivalent circuit diagram for an RCSJ Model for a Josephson junction. The ⋈ symbol is used to denote a Josephson junction.

The model ignores spatial variations and assumes a uniform barrier thickness or junctions of small surface area [38]. The total current through the junction is given by [39]:

$$I = \frac{C\mathrm{d}V}{\mathrm{d}t} + \frac{V}{R} + I_c \sin(\phi) \tag{1.29}$$

where V is the potential difference across the junction. Using Equation 1.23 we may describe V in terms of ϕ giving:

$$\frac{I}{I_\mathrm{c}} = \frac{C\Phi_0}{2\pi I_\mathrm{c}} \frac{\mathrm{d}^2\phi}{\mathrm{d}t^2} + \frac{\Phi_0}{2\pi R I_\mathrm{c}} \frac{\mathrm{d}\phi}{\mathrm{d}t} + \sin(\phi) \tag{1.30}$$

At this stage, two parameters are introduced for simplification. The plasma frequency ω_p describes the characteristic frequency of the junction and is given by $\omega_\mathrm{p} = \sqrt{2\pi I_\mathrm{c}/C\Phi_0}$. The second parameter is the junction quality factor Q used as a measure of the quality of the junction. This determinant is given by $Q = \omega_\mathrm{p} RC = \sqrt{\beta_\mathrm{c}}$. The term β_c is the Stewart-McCumber parameter given by $\beta_\mathrm{c} = 2\pi I_\mathrm{c} R^2 C/\Phi_0$. These parameters allow Equation 1.30 to be simplified to:

$$\frac{I}{I_c} - \sin(\phi) = \frac{1}{\omega_p^2}\frac{d^2\phi}{dt^2} + \frac{1}{\omega_p Q}\frac{d\phi}{dt}. \tag{1.31}$$

For junctions where $Q \ll 1$ the junction is said to be overdamped. The capacitance in the junction becomes negligible and thus the time constant of the RC element is not significant enough to impact on junction response. The $I-V$ characteristics of such a junction appear without any hysteresis. Where $Q \gg 1$, the junction is underdamped and hysteresis manifests in the $I-V$ curve due to the now significant contribution by the RC elements. Here a trapping and retrapping characteristic becomes visible in the behaviour of the junction.

The Josephson tilted washboard potential

Equation 1.30 for normalised current in the RCSJ model takes a form analogous to the equation of motion for a ball of mass m in a potential U surrounded by a viscous medium of viscosity v:

$$m\frac{d^2x}{dt^2} + v\frac{dx}{dt} + \frac{dU}{dx} = 0 \tag{1.32}$$

where x is the position on the axis of motion for the mass. This is illustrated in Figure 1.3 The analogy becomes clear when Equation 1.30 is rewritten with the form of Equation 1.34 to give:

$$\left(\frac{\hbar}{2e}\right)^2 C\frac{d^2\phi}{dt^2} + \left(\frac{\hbar}{2e}\right)\frac{1}{R}\frac{d\phi}{dt} + \frac{d}{d\phi}\left(E_J\left(1 - \cos\phi - \frac{I}{I_c}\right)\right) = 0. \tag{1.33}$$

Here, E_J is the Josephson coupling energy, given by:

$$E_J = \frac{\hbar I_c}{2e}. \tag{1.34}$$

This energy arises due to current flow in the junction and the Josephson inductance L_J introduced earlier. A real inductance would be associated with a

magnetic field generated by such a current flow. However, the superconducting nature of a junction means that this inductance results in the accumulation of potential energy in the junction.

The resulting benefit to the use of the washboard analogy is that characteristic parameters can be interchanged to better understand the behaviour of the system. This interchangeability is best summarised in Table 1.1.

RCSJ Model	Tilted Washboard Model	Parameter Relation
Capacitance C	Mass m	$(\frac{\hbar}{2e})^2 C \leftrightarrow m$
Current (bias) I	Washboard Tilt θ	$I \leftrightarrow \theta$
Phase ϕ	Position x	$\phi \leftrightarrow x$
Potential Energy U	Potential Energy U	$E_\mathrm{J}\left(1 - \cos\phi - \frac{I}{I_\mathrm{c}}\right) \leftrightarrow U$
Tunneling Conductance $1/R$	Viscosity v	$\frac{\hbar}{2e}\frac{1}{R} \leftrightarrow v$

Table 1.1: Table summarising the interchangeability of parameters between the RCSJ model and the tilted washboard equivalent.

Instances of the tilted washboard

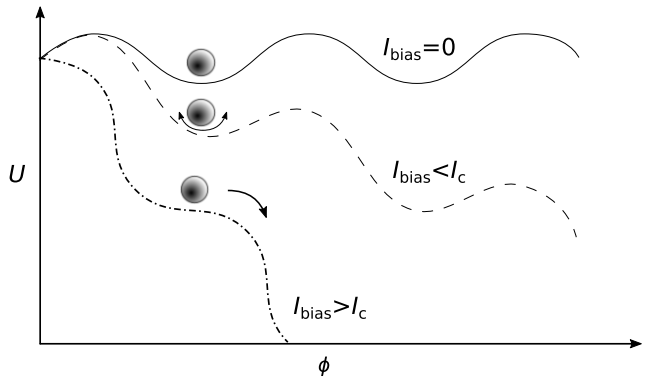

Figure 1.3: Illustration of the tilted washboard analogue of the Josephson junction. The potential energy of the junction is shown here as a function of the phase for the cases where $I_\mathrm{bias} = 0$, $I_\mathrm{bias} \leq I_\mathrm{c}$ and $I_\mathrm{bias} > I_\mathrm{c}$.

The washboard potential analogy may be applied to two particular instances of the RCSJ model, those of equilibrium and non-equilibrium, as illustrated in Figure 1.3. If a bias current is applied to the junction such that $I_\mathrm{bias} \leq I_\mathrm{c}$ the

tilt of the washboard is such that the ball remains trapped in one of the potential wells. Should the applied bias current increase such that $I_{\text{bias}} > I_{\text{c}}$, the tilt of the washboard potential will be increased such that the ball is no longer trapped in a potential well and begins to 'roll' down the washboard. This latter instance manifests with a non-zero phase variation $\mathrm{d}\phi/\mathrm{d}t$, a change in the potential energy U and a resulting voltage and resistance across the junction.

The tunnelling conductance of the junction is analogous to the viscous medium surrounding the ball and washboard. Earlier in the section we discussed the significance of overdamped and underdamped junctions and the relevance of the value of the Q factor as an indicator. The damping of the junction is related to the viscosity of the medium in the washboard potential. In the case of an overdamped junction, where $Q \ll 1$, we would expect a high viscosity and hence conductance. Here the washboard becomes 'sticky' and the ball becomes quickly trapped in a well provided that $I_{\text{bias}} < I_{\text{c}}$. In the instance where $Q \gg 1$ and the junction is underdamped, the viscosity of the medium would be negligible, thus even for a relatively low bias current or degree of tilt, we would expect the ball to have enough kinetic energy to escape from the potential wells and continue rolling.

1.2.3 Summary

In this section we have provided an overview of the fundamental physical theories and principles that govern the superconducting phenomenon in order to establish a basis for the work to follow. We have provided a summary of the BCS theory explaining the mechanisms behind the superconducting phenomenon for low temperature superconductors. We discussed the relevance of critical transition points in the phase characteristics of a superconducting material and introduced and explained the relevance of fundamental characteristic lengths such as the London Penetration depth and the coherence length for both BCS and the phenomenological GL theory of superconductivity. A concise foundation of the theory and physics governing the Josephson tunnelling phenomenon and related effects in Josephson junctions was also provided in preparation for use as an analogue where appropriate

for the understanding of work in superconducting nanowires to follow.

In Chapter 2, we focus more on the physics relevant to the study of QPS in nanowires in particular by reviewing the literature on the current state of the art, theory and experiments in the field. We also consider relevant work to date describing disorder in superconducting systems, particularly as dimensions are reduced.

Chapter 2

Quantum Phase Slip Phenomena and Disorder in Superconductors: Reviewing the State of the Art

2.1 Introduction

In the previous chapter we studied the physics of superconductors and Josephson junction theory that will be required for the analysis of our work in this thesis. In Chapter 2 we look at the evolution of work to date in the fields of phase fluctuations in superconducting nanowires and disorder in conductors and superconductors. We begin by providing an overview of superconductivity in nanowires, beginning with initial works by Little *et al.* [40], through to the introduction of phase slip phenomena and in turn more recent works demonstrating nanowires as functional elements to demonstrate flux tunnelling [5, 16]. We follow by providing a foundation in the theory behind disorder in conductors and superconductors. We discuss selected models from the field and look at how these have been applied to thin film superconductors and 1D regimes.

2.2 Superconducting Nanowires and Phase Slip Phenomena

The superconducting nanowire structure has been proposed for use in the investigation of quantum effects on the superconducting state. In addition, the sensitivity of the structures to these effects has led to the suggestion of novel applications. Of particular interest is the proposition that the wires behave as the dual to the Josephson junction, implying that they could become the key element in the development of a current standard [3], analogue to the Josephson voltage standard.

Finite resistance on the path to 1-dimensional superconductors

Superconducting nanowires may be classified as weak superconducting links. It is unsurprising that such structures should share similarities with the well studied Josephson junction structure.

As the cross-section of a superconductor is reduced and the superconductor is brought towards the 1D regime,a finite resistance has been observed to manifest. This finite resistance does not disappear even at $T = 0\,\mathrm{K}$, and is attributed to the influence of strong fluctuations affecting the weakened superconducting state in these structures.

At finite temperatures below T_c, these fluctuations are believed to be predominantly thermal in nature, whilst at the limit of zero temperature, the finite resistance is attributed to quantum fluctuations.

Phase slips

This finite resistance obsereved as superconducting nanowires tend towards the 1D regime is a property that is in agreement with the Mermin-Wagner theorem, which prohibits phase transitions in 1D systems[1][41]. From the perspective of superconductivity, a wire whose transverse dimensions are equal to or smaller than

[1]More specifically that in a systems of $d \leq 2$ dimensions at a finite temperature, continuous symmetries cannot be spontaneously broken.

the superconducting coherence length is considered to be in the one-dimensional regime. Such a wire made of superconducting material cannot undergo a phase transition to a fully superconducting state at a non-zero temperature.

The mechanism through which fluctuations cause this finite resistance is known as phase slippage (PS), and each individual event itself is referred to as a phase slip.

Thermally activated phase slips

As discussed earlier in this section, at finite temperatures, phase slip phenomena in the nanowire are attributed to thermal fluctuations. Such phase slips are referred to as thermally activated phase slips (TAPS).

In the 1960s, Langer and Ambegaokar [42], followed by McCumber and Halperin, put forward a theory to describe the effect of thermally activated phase slips, which later became known as the LAMH model.

Each TAPS event is described as a thermodynamic fluctuation that extends over a length $\sim 2\xi(T)$. This event drives the order parameter $\psi =\mid \psi \mid e^{i\phi}$ to zero at the point at which the TAPS event occurs. At this point the phase is indeterminant. For each phase slip event, the change in phase across the wire is $d\phi = \pm 2\pi$. Figure 2.1 illustrates the action of a phase slip in a length L of wire.

According to the Josephson relation [44] that was introduced in Equation 1.23 (repeated here as Equation 2.1), a fluctuation in the order parameter will cause a non-zero potential difference across the wire and give rise to a measurable resistance.

$$\frac{d\phi}{dt} = \frac{2eV}{\hbar}. \tag{2.1}$$

The free energy barrier of a TAPS event is given by $\Delta F(T) = (8\sqrt{2}/3)V_{\mathrm{PS}}H_{\mathrm{C}}^2(T)/8\pi$. Here, $H_{\mathrm{C}}(T)$ is the critical field and V_{PS} is the volume across which the phase slip occurs, equivalent to $V_{\mathrm{PS}} = \xi(T)A$, where A is the wire cross-sectional area. The phase slip attempt frequency is given by:

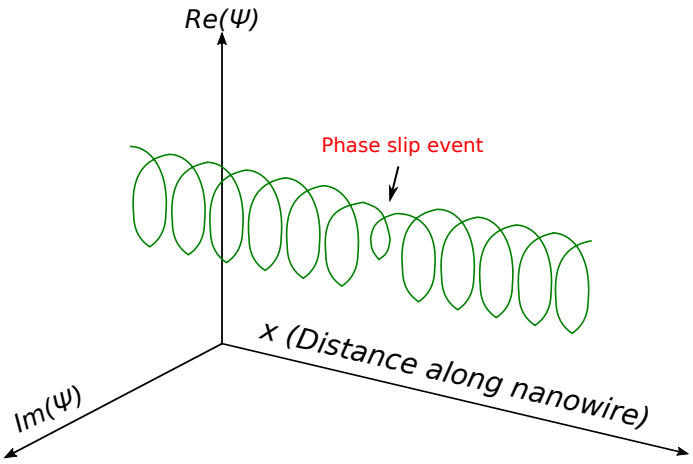

Figure 2.1: Illustration of a phase slip event in which the order parameter goes to zero at the point of action in the wire. Here x is the distance along the wire. The number of loops in the spiral is proportional to the supercurrent. Where a phase slip occurs, the spiral loses a loop and the supercurrent is reduced [43]

$$\Omega = \frac{8k_{\mathrm{B}}(T_{\mathrm{C}} - T)}{\pi h} \frac{L}{\xi(T)} \sqrt{\frac{\Delta F}{k_{\mathrm{B}}T}} \tag{2.2}$$

where k_{B} and $\hbar$ have their usual definitions and L is the length of the wire. It should be noted that the first term of this relationship is equivalent to the inverse if the relaxation time of the time-dependent Ginzburg-Landau theory, $\tau_{\mathrm{GL}} = \pi\hbar/8k_{\mathrm{B}}(T_{\mathrm{C}} - T)$. The resulting rate of thermally activated phase slip is given by:

$$\Gamma_{\mathrm{TAPS}} = \Omega e^{-\Delta F(T)/k_{\mathrm{B}}T} \tag{2.3}$$

For a non-zero bias current I, a voltage $V = (\hbar\Omega/e)\exp(-\Delta F/k_{\mathrm{B}}T)\sinh(I/I_0)$. Here, $I_0 = 4ek_{\mathrm{B}}T/h$. Since $R = V/I$ we obtain the relation for the temperature dependence of the wire to be:

$$R_{\mathrm{LAMH}}(T) = R_{\mathrm{q}} \frac{\hbar\Omega}{k_{\mathrm{B}}T} e^{-\Delta F/k_{\mathrm{B}}T} \tag{2.4}$$

where R_q is the quantum of resistance defined as $R_q = h/(2e)^2$.

Quantum phase slips

In the limit of zero temperature, well below T_c, thermal fluctuations are believed to be supressed and the influence of quantum fluctuations on the behaviour of the wire becomes the dominant mechanism by which phase slips occur.

These quantum phase slips (QPS) have the same suppressive effect on the order parameter as was illustrated in Figure 2.1. For such events, the order parameter does not rely on thermal fluctuations to overcome the energy barrier. Instead quantum phase slips describe the event in which the order parameter tunnels through the barrier, as indicated in the washboard model illustrated in Figure 2.2.

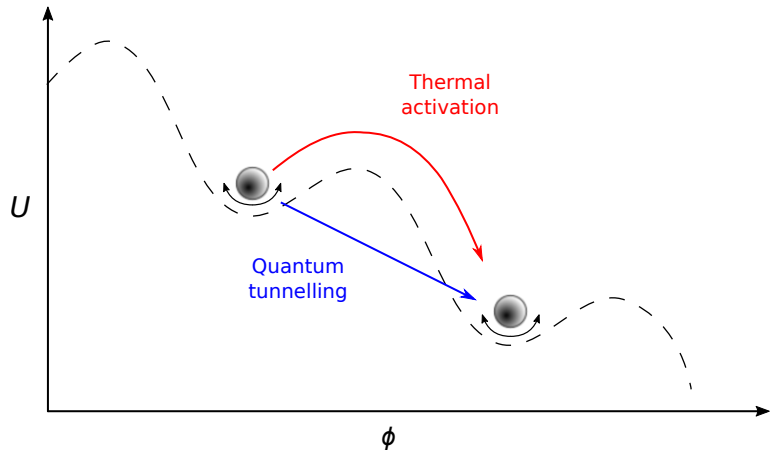

Figure 2.2: Illustration of a thermally activated and quantum phase slip events using the tilted washboard model. The particle can overcome the barrier and traverse to the lower energy minima through thermal activation or quantum tunneling.

In Giordanos' Macroscopic Quantum Tunneling (MQT) model[45], the rate of phase slip events driven by quantum fluctuations that occur in a nanowire is given by:

$$\Gamma_{qps} = B\Omega_{qps} e^{(-a\Delta F_{qps}\tau_{GL})/h} \tag{2.5}$$

where $\Omega_{\mathrm{qps}} = (L/\xi_{\mathrm{GL}})\sqrt{\Delta F_{\mathrm{qps}}/k_{\mathrm{B}}T}$ is the quantum tunnelling attempt rate, and a and B are fitting constants. The resulting resistance attributed to quantum tunneling events is given by:

$$R_{\mathrm{qps}} = BR_{\mathrm{q}}\frac{\hbar\Omega_{\mathrm{qps}}}{\left(\frac{\hbar}{\tau_{\mathrm{GL}}}\right)}e^{(-a\Delta F_{\mathrm{qps}}\tau_{\mathrm{GL}})/\hbar}. \tag{2.6}$$

It should be noted that if the constants are ignored, Equation 2.6 is a simple conversion from R_{LAMH} that can be made by replacing the thermodynamic dependence $k_{\mathrm{B}}T$ with $\hbar/\tau_{\mathrm{GL}}$.

Early observations of fluctuation effects on the temperature dependence of superconducting nanowires

The presence of phase slip phenomena in superconducting nanowires has been investigated since the late 1960's. In 1967, Little [40] reported that thermal fluctuations destroyed persistent current in one-dimensional superconducting rings. However, Little claimed that this only occurs where these fluctuations drive the amplitude of the order parameter to zero, effectively severing the loop.

Further to Little's work and supporting evidence offered by Parks *et al.* [46], Langer and Ambegaokar put forward a theoretical explanation of current-reducing fluctuations in narrow superconducting channels [42]. Using Ginzburg-Landau theory, these thermodynamic fluctuations were shown to act over a length equal to that of the superconducting coherence length and result in a phase slip of 2π.

Langer and Ambegaokar proposed that these thermal fluctuations cause deviation from the material's critical current, resulting in intrinsic resistive transitions at temperatures just below the T_{c} of the bulk material.

McCumber and Halperin expanded Langer and Ambegaokar's theory ultimately forming the Langer, Ambegaokar, McCumber and Halperin (LAMH) model of thermally activated phase slips, otherwise known as TAPS. Confirmation of the models' accuracy was demonstrated by experiments such as those by Lukens *et al.*, who reported observing thermally activated phase slips during measurements on

single crystal tin whiskers [47].

To date, thermally activated phase slips are considered the cause of a broadening of the transition observed in the resistive curve in the vicinity of T_c [48]. However, there has been increasing evidence that for $T < T_c$, thermal fluctuations become less prominent and the dimensions of the nanowires dictate that phase slip may also be induced by quantum effects.

In 1988, Giordano published an investigation into the superconducting to normal transition in In wires of 40-100 nm diameter [45]. Giordano reported that, whilst the LAMH model was consistent with results for temperatures within 0.2 K of T_c, at lower temperatures it failed to describe the behaviour of his nanowires. He observed that as the temperature decreased, the size of the free energy barrier relative to the thermal energy $k_B T$ increased and that this would lead to a rapid reduction in the thermal activation rate. Evidence for this is illustrated in Figure 2.3 adapted from the original paper [45], where the experimental data diverges from the theoretical model as the difference $T - T_c$ exceeds 200 mK. Giordano seconded the suggestion made by A. J. Van Run *et al.* [49], that as T→0 K, phase slip becomes a Macroscopic Quantum Tunnelling (MQT) phenomenon.

The quantum nature of the suggested effects dictates that the dimensions of the conductors were of particular importance to achieving experimental evidence. In order for the influence of the effect on the electrical properties of the wires to be observable, the dimensions of the wires had to be quasi one-dimensional. The phenomenon would be most easily observed in ultra-thin superconducting wires. Zaikin *et al.* predicted the ideal thickness for nanowires in which quantum fluctuations would be significant to be in the range of 10 nm [50].

In 2000 Schön published an article [51] on superconducting nanowires alongside work by Bezryadin and Tinkham documenting quantum suppression of superconductivity in thin MoGe nanowires [13]. In the article Schön echoes Giordano asserting that close to absolute zero, the thermal energy is lower than the characteristic energy of the phase slip process $\hbar\omega_c$, where $\hbar$ is the reduced Planck's constant

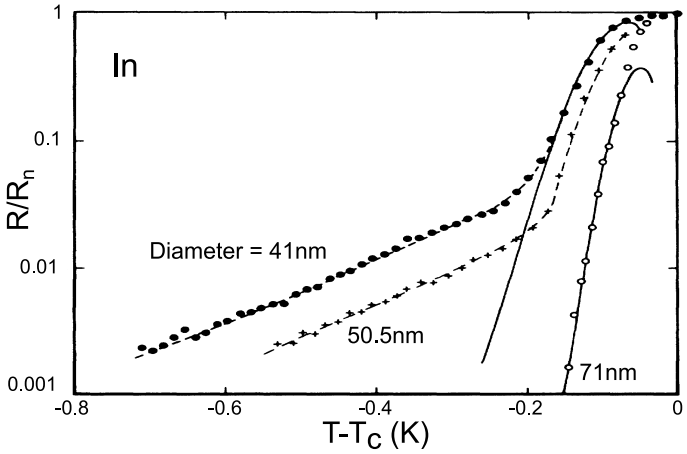

Figure 2.3: Graph showing the resistance, normalised by the normal state resistance as a function of temperature for three In nanowires of diameter 41nm (•), 50.5 (+) and 71nm (○). The solid curves are fits to the thermal activation theory whilst the dashed curves are fits to a theoretical total rate RT which is the sum of both thermal activation and MQT rates. Adapted from Giordano [45]

---

and ω_c is the characteristic frequency of the system. In this theory, quantum effects dominate as phase slip events are caused by quantum tunnelling through the potential barrier as opposed to thermal activation over it.

Schön discussed the strength of the work by Bezryadin and Tinkham who, after successfully fabricating homogeneous MoGe nanowires of less than 10 nm, found that the wires became superconducting only if the normal state resistance of the nanowire is lower than a critical resistance. The critical value of resistance corresponds to R_q, the quantum resistance for Cooper pairs, at a value of 6.45 kΩ. These findings agree with earlier predictions by Zaikin *et al.* [50]. Where the normal state resistance of the wires was higher, the wires remained resistive even approaching 0 K.

The theory of what became known as the Quantum Phase Slip (QPS) phenomenon, continued to gather credibility. In 2001 Lau, in collaboration with Bezryadin and Tinkham, published more evidence indicating the quantum influence on superconductivity in nanowires [52]. This gave further strength to the accuracy of models which accounted for both the influence of thermally activated phase slips

in the region of the T_c and quantum phase slip as $T \rightarrow 0\,\mathrm{K}$.

In 2005, Zgirski and Arutyunov [12] published an article in which they presented an overview of the mechanisms governing the behaviour of superconducting nanowires. They also attempted to prove the size dependence of the phenomenon by tracing the crossover point between thermally activated and quantum phase slips. Within the article, the authors provide a definition of a one-dimensional superconducting wire as one in which the smallest transverse dimension $\sqrt{\sigma}$ is smaller than the ξ_{GL}. Within this limit, any fluctuation will drive a fraction of the wire into a normal state. With only one path through which the supercurrent can flow under these dimensions, the events cause voltage spikes due to the momentary passage of a normal current, and thus a finite and measurable resistance.

Zgirski observed a clear broadening of the transition phase as the cross sectional area of his sample was reduced, as can be seen in Figure 2.4. He found that, whilst $R(T)$ dependencies agreed with the model of thermally activated phase slips for diameters of wire $\sqrt{\sigma} \geq 15\,\mathrm{nm}$, thinner wires exhibited considerably wider transitions and did not necessarily tend to zero resistance as T approached 0 K. He identified this deviation from the model as the manifestation of quantum phase fluctuations or phase slips.

In 2007, Zgirski and Arutyunov highlighted an important consideration critical to proving the existence of quantum phase slips [53]. They warned that much of the work on phase slips until then had not taken account the experimental fact that the T_c of many superconducting materials is dependent on the cross sectional area. As the size of these superconductors is reduced, the influence of material inhomogeneity and disorder increases and could thus be a factor in the broadening of the superconducting transition phase in ultra-narrow wires.

In order to eliminate this uncertainty Zgirski and Riikonen *et al.* repeated the experiments characterising superconducting Al nanowires as theirs cross-sectional dimensions were progressively reduced using broad beam ion milling [54]. In these experiments they chose to work with aluminium, based on experimental evidence

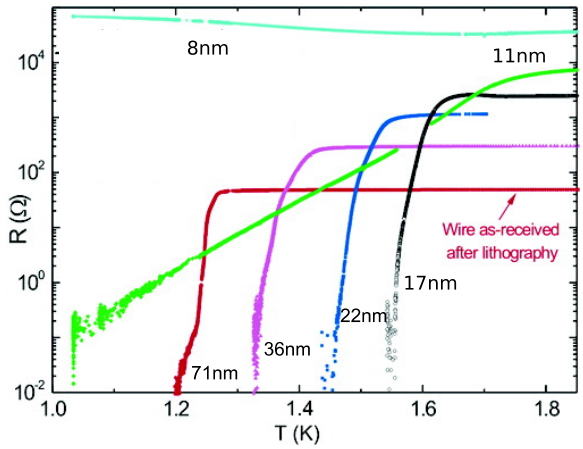

Figure 2.4: $R(T)$ characteristic of an Al wire of length L=10µm after size reduction across repeated Ar+ ion sputtering sessions. Particularly striking is the difference between the data for the two thinnest wires from the thicker ones. Adapted from [12].

---

that the T_c of aluminium increases as its wire diameter decreases, as noted in [12]. This meant that broadening of the $R(T)$ dependencies below the bulk T_c could not be interpreted as being caused by geometrical imperfections.

Their experiments found a persistence in the observed broadening of the transition in sub 15 nm wires originally attributed to quantum fluctuations. They could not completely rule out the impact of inhomogeneity of the samples on the $R(T)$ dependencies. An ideal of atomically flat and infinitely long wires is suggested as the only true means of eliminating all doubt. However, Zgirski *et al.* do argue the validity of the QPS model based on the agreement between the model and the experimental data.

Efforts to confirm the QPS phenomenon continued with work such as that published by Bae *et al.* in 2009 [55], in which the authors describe two methods of identifying phase slips in nanowires. The measurements were carried out on both MoGe and Al nanowires created by sputtering the superconductors onto polymer scaffolds stretched across a void.

Firstly, they fit measurements of the nanowires $R(T)$ curves to established

models for thermal and quantum activated phase slips. TAPS phenomena were modelled using the Arrhenius-Little fit (AL-TAPS) [13], whilst the Khlebnikov theory (KQPS) [56] was used to fit to the curves in the suspected QPS regime across the lower temperature data points. One final theory, that of Golubev and Zaikin (GZQPS) [57, 50], forms the basis of the last fit which considers dissipation by QPS. For the MoGe nanowires, the KQPS model proved a relatively accurate fit to the sharp drop in resistance at lower temperature, but the TAPS or AL model provided a closer fit for both lower and higher values of temperature, leaving the results inconclusive. In the case of the Al nanowire, TAPS offered the worst fit to the data at lower temperatures and whilst the fit for KQPS was closer to the curve it still did not provide adequate approximation. However, the GZQPS fit offered a surprisingly close approximation of the resistive tail, indicating that it could indeed originate from QPS.

The second analysis used was to take measurements on the nanowires under microwave radiation. At appropriate frequencies, this will induce voltage plateaus in the $I - V$ curves, namely Shapiro steps. These steps, which may be predicted using Josephson's ac relation, can be used to interpret current-phase characteristics (CPR) in the wires. The authors state that when the step width does not go to zero for any microwave power, the CPR is multi-valued, whilst the opposite applies to single-valued CPR. In turn and quite critically, Khlebnikov's theory suggests that, TAPS-dominated wires display multi-valued CPR whilst single-valued CPR indicates QPS dominated wire.

Based on this theory the authors found that the step widths did not reach zero for the MW powers used, suggesting multi-valued CPR for the MoGe wires, and indicating TAPS dominated behaviour. The Al wire could also yield no direct proof of QPS using the microwave analysis, however it is suggested that due to the resistive tail off in the $R(T)$ measurements, QPS could yet be active in the wire. Indeed they suggest that sufficiently long wires under analysis using the Shapiro method could be the key to yielding direct evidence for the existence of QPS in

superconducting nanowires.

The Josephson-QPS duality

In 2005, Mooij and Harmans proposed a QPS based qubit structure [58]. The structure, formed of a superconducting ring interrupted by a nanowire, was predicted to sustain two states of circulating persistent current with equal energy, one clockwise, the other anticlockwise. With an applied magnetic flux of $\Phi_0/2$, the direction of the persistent current was predicted to change with the occurrence of quantum phase slips. Thus a new form of flux-qubit could theoretically be possible. In the publication Mooij *et al.* suggest the use of $Nb_0.42Si_{0.58}$ due to its high normal state resistance and calculate the rate of QPS events for such a wire and how this would scale with coherence length.

Following the proposal of the QPS flux-qubit, Mooij and Nazarov looked in detail at the parallels between Josephson junctions and superconducting nanowires [3], which they redefined as QPS Junctions. In this pivotal document the authors derived a series of relationships for the characteristics of QPS junctions according to this dual equivalence to the known Josephson relations, most importantly the prediction and definition of a critical voltage feature V_c. Mooij *et al.* proceeded to propose equivalent circuits and describe their potential use in experiments proposed to mirror milestones achieved in Josephson physics for the equivalent variables in the QPS junction. Of particular importance was the prediction for the potential observation of dual Shapiro steps that could lead to a new quantum based current standard. A more in depth overview of the relationships and circuits proposed in this publication is provided as part of Chapter 7.

Direct observation of QPS

In 2012, three works of considerable significance to QPS were published. These provided proof of the QPS phenomenon and were heavily based on the duality predicted by Mooij and Nazarov [3]. The first of these, by Hongisto and Zorin [59], reported on the successful fabrication and characterisation of a QPS transistor, the

predicted dual to the dc SQUID. Two devices were reported on, both fabricated from two Nb_xSi_{1-x} nanowires isolated from the environment by two larger regions of superconductor forming inductive elements and by high value (0.4MΩ) Cr thin film resistors. Capacitive gates were used to control the channel between the nanowires. Figure 2.5 **a.** shows the device in full detail with the equivalent circuit show in **b.**.

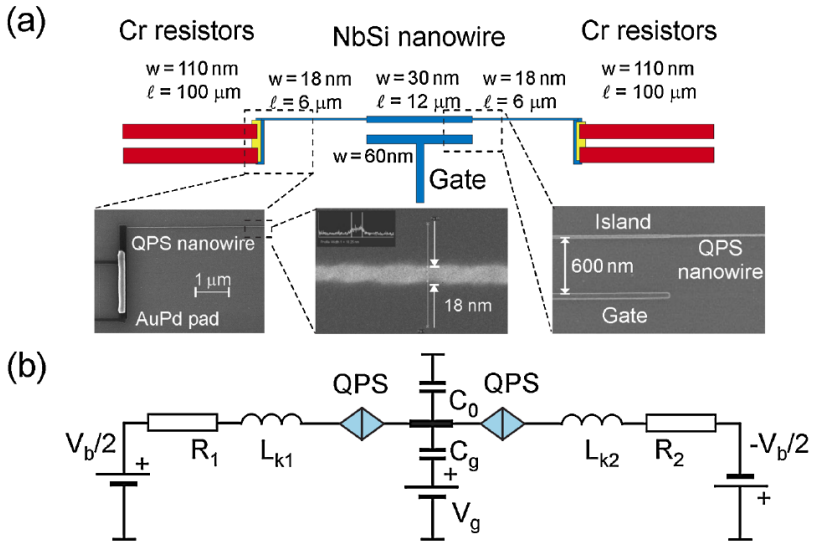

Figure 2.5: **a.** Layout and SEM images of the QPS transistor with its constituent elements. **b.** Equivalent circuit utilising voltage biased QPS Junctions. From [59].

From the equivalent circuit diagram, it can be seen that the device is formed of two series-connected voltage biased QPS junctions as proposed by Mooij and Nazarov [3]. Given the predicted duality, in the place of the phase sensitivity and critical current observed in dc SQUIDs, a charge sensitivity coupled with a critical voltage feature could be expected. Hongisto *et al.* performed low temperature sweeps of both devices and were able to confirm a voltage threshold both in current bias and voltage-bias regimes. The results of the voltage-biased measurement are shown in Figure 2.6.

Following the demonstration of a QPS transistor, Arutyunov *et al.* published evidence for the observation of QPS in superconducting nanorings [60]. It has been

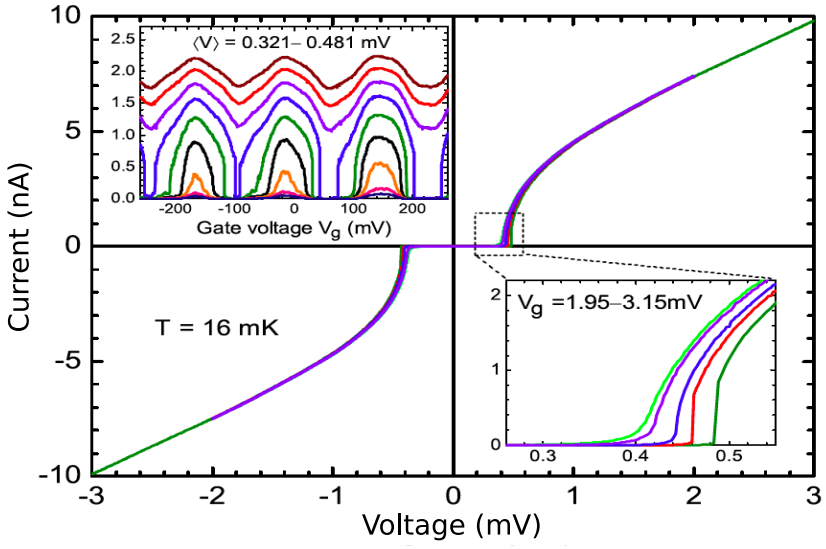

Figure 2.6: Critical voltage feature in a QPS transistor at $T = 16\,\mathrm{mK}$. Upper left inset: Dependence of the current on applied gate voltage measured for $0.321 < V_\mathrm{b} < 0.481\mathrm{mV}$. Lower right inset: Indications of a Coulomb blockade corner with scaling of the gate voltage. Adapted from [59].

---

well established that a superconducting ring can sustain a persistent current that is sensitive to the flux through the ring. As flux is increased above the critical current of the ring, the persistent current will drop. In 2002, Matveev *et al.* had predicted that, for superconducting rings this behaviour would be considerably altered. The presence of QPS was predicted to cause the amplitude of the flux induced current modulations to become exponentially small [61] and undergo a rounding effect, changing from sawtooth to sinusoidal in characteristic. In addition, the energy levels were expected to split. Arutyunov *et al.* demonstrated that this could be observed in Al and Ti nanorings both in comparison between rings of larger and smaller track widths and for rings whose track-width was successively reduced using ion milling.

Following these publications, Astafiev *et al.* demonstrated the successful realisation [5] of the Mooij-Harmans QPS-qubit predicted in 2005 [58]. The device was fabricated from $\mathrm{InO_x}$ as an alternative disordered superconducting system to $\mathrm{Nb}_x\mathrm{Si}_{1-x}$. Attempts to fabricate a successful device in Ti and Al had been

reported but failed to exhibit qubit behaviour. Astafiev *et al.* suggest that the proximity of the InO_x nanowires to their superconductor to insulator transition and the very disordered nature of the superconductor could be responsible for the material's success. The device comprised the proposed loop structure interrupted by an embedded 40 nm×400 nm nanowire, as can be seen in Figure 2.7.

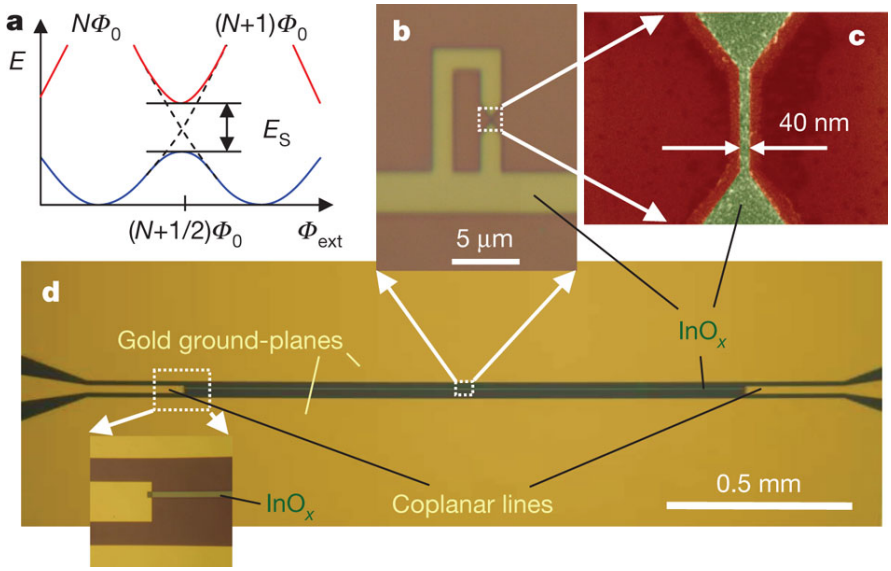

Figure 2.7: The QPS Qubit demonstrated by Astafiev *et al.*. **a.** shows energy level splitting in the loop for ground (blue) and excited (red) states. **b.** InO_x loop with **c.** embedded nanowire. **d.** Resonator structure and contacts. From [5].

The loop is connected to a step impedance resonator through which it is controlled. Astafiev *et al.* fabricated a range of similar loops, though only this particular configuration of loop dimensions and resonator exhibited the desired response demonstrating energy splitting in spectroscopic measurements.

In 2013, Webster *et al.* reported the observation of Coulomb blockade and a critical voltage feature indicating the influence of QPS in $Nb_{0.45}Si_{0.55}$ nanowires [62]. Based on predictions by Mooij *et al.* [3], the aim of the investigation was to implement a voltage biased phase slip junction with the ultimate goal of observing Shapiro step equivalent features dual to those used in the Josephson voltage standard. The device incorporates a superconducting nanowire embedded in a high

impedance environment consisting of an inductive region of wider superconductor and CrO_x thin film resistors. The authors reported critical voltage features in confirmation of QPS phenomena but did not observe steps in the $I-V$ characteristics under applied microwave radiation. They subsequently demonstrated through heating models that the electron temperature in the CrO_x resistors was elevated well above the substrate temperature. They proceeded to model the response of the system to related Johnson noise confirming that at these levels, any features in the $I-V$ characteristics would undergo considerable smoothing, before presenting pulsed biasing as a viable solution to the issue of heating in the resistors.

Peltonen *et al.* subsequently published work demonstrating the observation of flux tunnelling through superconducting rings with NbN nanowires [16]. Using similar device design to the earlier InOx device, this time with multiple loops on a single resonator, Peltonen *et al.* were able to measure the energy gap (or phase slip energy E_S) by probing the transition frequencies between the ground state and two lowest excited states in different coupled loops. They also used these measurements to investigate the dependence of E_S on wire width finding an exponential characteristic defined by $E_s = E_0 \exp(-k\bar{w})$. E_0 is given by $\rho\sqrt{l/\bar{w}}$ for strongly disordered superconductors, $\bar{w}$ is the mean wire width and k^{-1} is the width at which the wire becomes a 1D channel. Figures 2.8 **a.** and **b.** show the results for both of these dependencies.

To date, there is thus significant evidence in support of quantum phase slip as an influential phenomenon on the behaviour of superconductors in the quasi-1D and 1D regimes. There has also been significant progress in demonstrating how this phenomenon can be harnessed in making novel devices for use in quantum computing, flux sensing and a quantum based current standard. An outcome of the large body of work in this field is that it becomes increasingly clear that these effects occur in the region close to the superconductor to insulator transition [5] particularly in highly disordered superconductors that are typically poorly described by the BCS theory [16, 63].

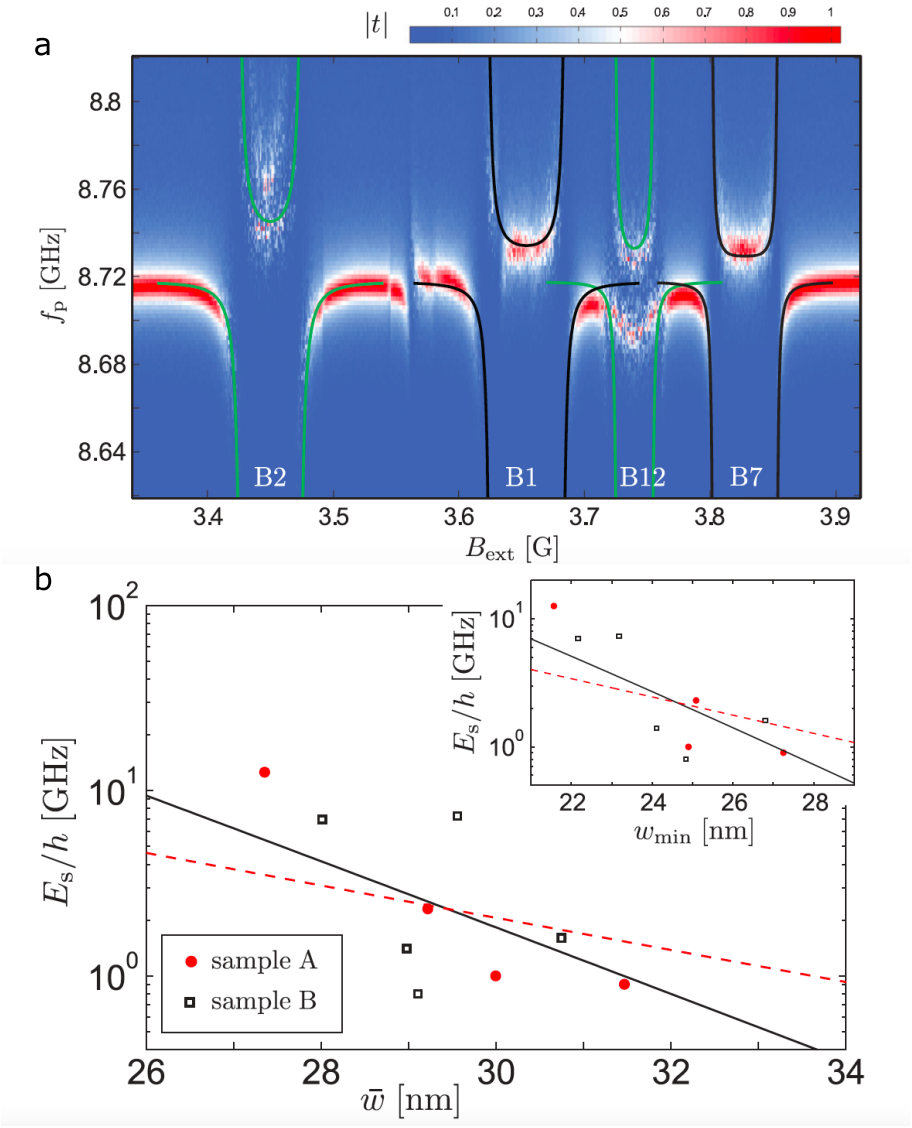

Figure 2.8: **a.** Spectroscopic measurement results of transmission t in NbN qubit structures at 40 mK. The lines show the transition frequencies between ground and the excited energy levels of the coupled qubits. B2, B1, B12 and B7 refer to qubit structures containing nanowires of different widths. **b.** shows the dependence of the phase slip energy gap E_S on average nanowire width. The red circles and black squares indicate nanowires in InO_x qubit loops on two separate samples A and B. The lines indicate exponential fits to the data. Inset: The same dependence of E_S on minimum nanowire width w_{min}. Adapted from [16].

For this reason, it is of considerable importance to understand how the impact of disorder in superconducting materials manifests in their behaviour, particularly as dimensions are reduced from the bulk down to the 2D and 1D regimes, which is a subject left largely unexplored by the current literature and is the focus of the present thesis.

In the next section we provide an overview of the relevant aspects of disorder in conducting and in superconducting materials to provide a basis for our investigations.

2.3 Disorder in Superconducting Materials: Fundamentals, Literature Review and State of the Art

In its most basic definition the term "disorder", when applied to a many particle system, pertains to the absence of symmetry. An ordered system is one in which one or more degrees of freedom is permitted. These degrees of freedom could be translational allowing a crystalline order, rotational allowing ferroelectric polarisation and ordering, and spin-state magnetic ordering.

For the purposes of these investigations we refer primarily to translational order and disorder in superconducting materials. An inference can then made that the only case of a pure, translational, long-range ordered system occurring in a solid, is where lattice periodicity exists. In such a solid, the structure of the lattice may be described as a repeating occurrence of some base arrangement of particles, namely the unit cell. This type of solid is referred to as crystalline in structural form. By retrospective definition, a system that is polycrystalline or amorphous will have limited or no translational order and may thus be considered to exhibit some degree of disorder. As such, disorder may exist in varying degree in any material that is not a perfectly pure crystalline structure, a form that is impossible to achieve for reasons that will be explained in the next section. This disorder may manifest in form from a limited number of foreign atoms in an otherwise perfect crystal structure, to systems of strong disorder such as amorphous alloys or glass

structures. Thus, the first identifier of disorder in a system is its structural form.

Entropy

Entropy is described as a measure of disorder in a system. It is a measure of the number of possible configurations in which a thermodynamic system may be arranged. As an example, a material in its superconducting state has less entropy than when in its normal state, as an inherent characteristic of Cooper pairs is their long-range phase order in contrast to conduction electrons.

While a superconductor will have zero resistance in its superconducting state, its entropy is not zero. Above absolute zero the population of charge carriers in the system comprises of both paired and unpaired electrons. Since the normal state electrons in the system do not contribute to the supercurrent and within the temperature range $0 < T < T_c$ lattice vibrations will still exist to influence these, a degree of entropy will exist within the system.

For the present thesis, our interest is in the manifestation of quantum behaviour in disordered superconductors. Since entropy describes disorder in material systems using a thermodynamic approach, it will not be further included in our analysis.

Defects & impurities

The number of defects in a system is the second largest contributor to the level of translational disorder in an electronic system, after its structural form. The term defect is used to describe any arrangement or physical presence or absence in the lattice, that causes the material to deviate in form from a perfect crystalline structure. These can be broken down into four sub types based on dimensionality [64]. These are point, line, area and volume defects. A point defect is either an interstitial atom or a vacancy or missing atom or in the lattice. An interstitial atom is an additional atom within the lattice, either of the same elemental composition as the material, or an impurity atom. In the context of material science, an impurity in a material is any atom which differs from the elemental composition of the material. All naturally occurring materials contain impurities. Although it is possible to

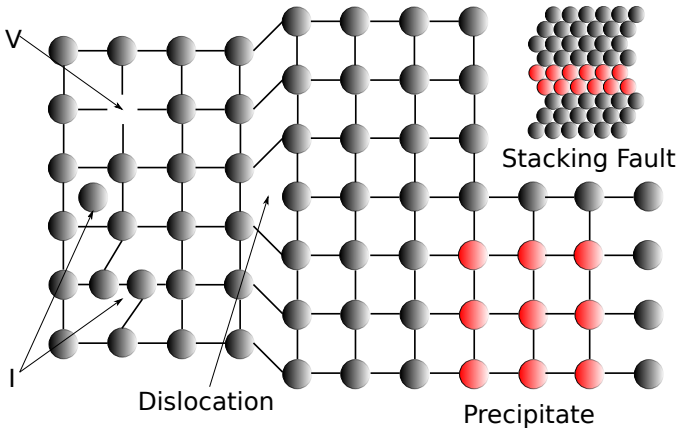

Figure 2.9: Simplified representation of common defects in a 2D lattice. V and I represent Vacancy and Interstitial type point defects. The dislocation represents a typical line defect, while the stacking fault and the precipitate are area and volume defects respectively. Adapted from Plummer [64]

considerably limit the amount of impurity in a system it is nearly impossible to completely exclude all impurity from a material.

Line defects or dislocations are caused when one region of the lattice adjoins another region which has an extra plane of atoms. The mismatch between the differing lattices results in a dislocated row of atoms, which would propagate into the plane of the illustration in Figure 2.9. 2D area defects or stacking faults are also associated with dislocations. They are formed along planes and occur with the insertion or removal of a plane to the lattice. The surrounding planes are shifted to accommodate them, resulting in dislocations along the edges of the added plane or its neighbours when it is removed.

Finally volume or 3D defects are formed by agglomerates of interstitials or vacancies. These take the form of crystalline grains, amorphous collections of interstitial atoms, or large voids in the overall lattice. A precipitate is one example of a crystalline volume defect. The diagram in Figure 2.9 illustrates this as a crystal of impurity atoms, each occupying a site in the lattice. It is assumed that this would propagate into the plane to form a 3D defect volume of material within the

lattice.

Surfaces are of particular significance for defects in all dimensional systems. Defects exist at surfaces due to unlinked atoms and thus dangling bonds. This is particularly important as dimensions are reduced, as the ratio of the surface area to the bulk material of a structure is increased. For nanoscale structures, this ratio is at a maximum in comparison to large two and three dimensional structures from the same material.

The Drude model of conduction

To understand why disorder and defects in a material are significant we first consider the mechanisms of conduction in an electronic system. Paul Drude [65] proposed the first model of conduction. The Drude model treats electrons as a "gas of particles" moving through an ionic lattice and applies Boltzmann statistics to analyse their behaviour. This early model assumed that electrons do not undergo any long-range interactions with each other or with lattice ions but only interact in the form of instantaneous collisions with ions, from which they scatter [66]. Drude proposed that these collisions were separated by an average time period or relaxation time τ. For n electrons with charge e and mass m, that travel within a field $\mathbf{E}$ that is both uniform and constant, the model predicts the dc current density to be given by [67] :

$$\mathbf{J} = \left(\frac{ne^2\tau}{m}\right)\mathbf{E} = \sigma\mathbf{E} \tag{2.7}$$

where the bracketed term provides the conductivity σ of the material.

Of primary significance in this work was the approximation of the relaxation time. However the model was later found insufficient as it overestimates the contribution of electrons to thermal conductivity κ in metals, assuming no dependence on temperature or contribution from phonons.

The Drude-Sommerfeld or Free Electron model

In 1933, Sommerfeld replaced the Drude model's Boltzmann distribution de-

pendency using quantum mechanics [66]. Whilst the Drude-Sommerfeld model is a fundamental model in solid state physics, an in-depth treatment of the model is beyond the scope and purpose of this review. Only a brief summary of its significance will be provided here.

Sommerfeld's new model sustained the assumption that conduction electrons travel through a lattice as a free electron gas, assuming no interaction between themselves or the ions in the lattice. However, it differed in two significant principles. First, the negative charge of the electrons needed to be balanced by the assumption that they travel through a smeared uniform positive charge from the lattice ions. This charge does not exert a field on the electrons, but serves to maintain neutrality. Secondly, electrons were to be treated as fermions, particles with half-integer spin. As such, the free electron gas must meet the requirements of the Pauli exclusion principle where no two fermions can exist simultaneously occupying the same state, location and time.

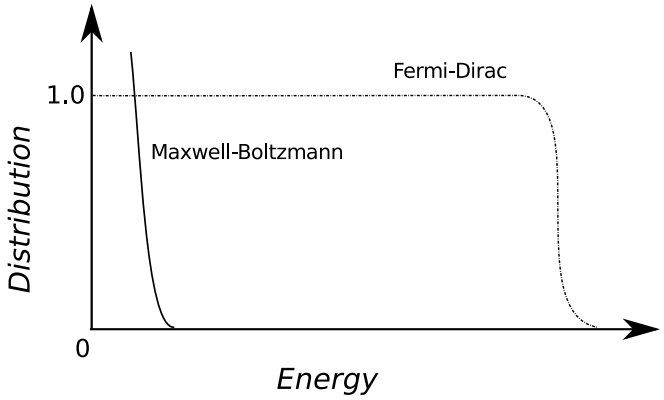

Figure 2.10: **a.** Simplified comparison of Maxwell-Boltzmann and Fermi-Dirac distribution functions for a metal at room temperature, where m and v are electron mass and velocity, and T is the temperature of the metal. **b.** The Maxwell-Boltzmann distribution function in full scale. The plots illustrate why the Maxwell-Boltzmann dependant Drude model fails to describe thermal conductivity in metals. Adapted from [66]

The Drude-Sommerfeld model recognised that the energy levels of electrons are

discrete. By treating electrons as fermions, and introducing the dependence on Fermi-Dirac distribution, the Sommerfeld model is able to predict the density of states for a conduction electron by solving Schrodinger's equation for an electron in a 3-dimensional space. It demonstrated that only electrons near the Fermi energy would be able to absorb energy applied to the system, much reducing the electronic contribution to conduction. The thermal conduction approximation in the Drude model was adjusted accordingly. Figure 2.10 illustrates the overlay between the application of Maxwell-Boltzmann and Fermi-Dirac distributions to thermal conductivity in metals. The Sommerfeld electronic contribution $k_{\mathrm{B}}T/E_{\mathrm{F}}$, where E_{F} is the Fermi energy, can be seen to be considerably smaller when compared to the Drude value. The large concentration of low energy filled states in the Maxwell-Boltzmann distribution illustrates why the classical Drude model could not be used to accurately describe the thermal properties of metals.

The model provides an explanation as to why electrons do not scatter from ions that occupy regular lattice spaces and only collide with impurity ions. This is because the wavelike characteristic of an electron passing through the lattice causes it to diffract from an ideal crystal [68], due to the crystal's translational symmetry. Electrons passing through a material would only scatter from imperfections or defects in the lattice.

Thus, the greater the disorder in a material caused by larger numbers of imperfections, the greater the reduction in translational symmetry. This results in increased scattering and a considerable reduction in the mean free path of the electrons, leading to higher resistivity in the material.

Anderson localisation

The Sommerfeld-Drude model provides a sufficiently accurate explanation for the existence of metals, however it fails to explain conduction in semiconductors, or the lack thereof in insulators. It also could not explain the observation of metal-insulator transitions in materials. In 1958, Anderson [69] highlighted that

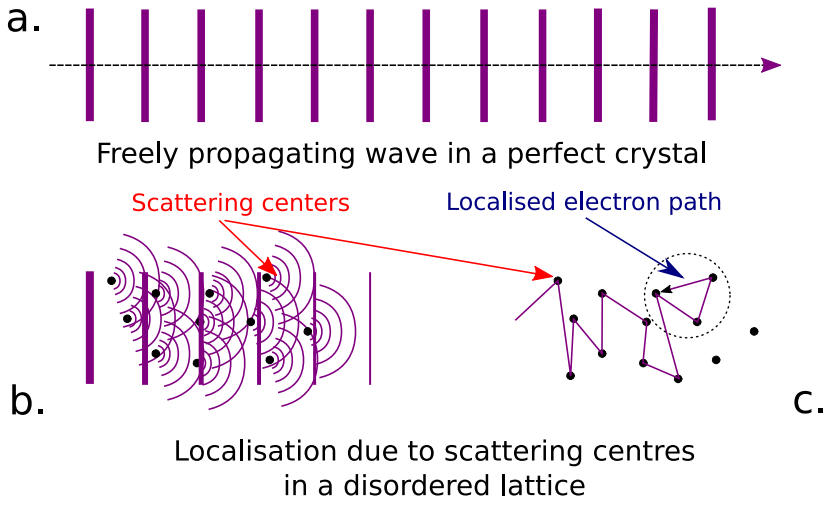

Figure 2.11: **a.** A wave based interpretation of Anderson localisation. Shows a freely propagating wave in a perfect crystal. **b.** The propagation of a similar wave in a disordered medium with interference leading to localisation. **c.** Localisation of an electron path in a similarly disordered lattice.

the relationship between disorder and mean free path in materials other than perfect crystals was not continuous.

Anderson looked at the effects of the random potential arising from disorder in the material and calculated the probability of a particle returning to its origin. This work made the argument that at some critical threshold of disorder, the aforementioned probability is non-zero and thus diffusive conduction in a host material [2] will simply cease rather than continue to scale. Based on this he found that, depending on how strongly disordered or randomised the potential is, the electron wavefunction could be considerably altered [70]. Anderson put forward the principle of localisation, whereby electrons[3] remain localised to a region around some site. For low temperatures, as electrons begin to behave more like waves than classical particles, quantum interference generated by the scattering of electrons as

[2] Anderson's original publication discussed conduction in semiconductors

[3] In the paper Anderson refers to quantum mechanical particles moving from one energy site to another site but stipulates that the theory could be applied to electrons with regards to electron spins

waves begins to dominate transport in materials.

This is illustrated in Figure 2.11. Rather than having a freely propagating wave with an extended wavefunction as one might expect in a perfect crystal, Anderson proposed that the wave becomes localised, due to interference from the repeated scattering of the electron. For systems of sufficiently strong disorder, this interference can be destructive to the propagating wave. It increases the probability that the electron will return to its point of origin decreasing the propagating conduction wavefunction, causing an exponential decay of its envelope around some point, and the material to become increasingly more resistive or transition into an insulator phase. Shortly afterwards, Ioffe and Regel [71] predicted this transition from metal to insulator would occur when $l \leq \lambda_{\mathrm{dB}}$, where l is the electron mean free path in the material and λ_{dB} is its de Broglie wavelength.

The role and characterisation of structural disorder in superconductors

In the following year, Anderson published a theoretical treatment of dirty superconductors [72]. His expressed interest was the fact that superconductivity had been demonstrated to persist in the presence of considerable impurities with little variation in characteristics when compared to the pure material counterpart. He highlighted that this was observed to be the case for non-magnetic impurities but only so to a limited degree in the case of magnetic impurities citing work by Matthias *et al.* [73].

Anderson divided superconductors into two groups. The first group was for relatively pure superconductors which exhibit a sharp response to the introduction of impurities. The second was for the so-called "dirty" superconductors, that were already heavily disordered, where the addition of further scattering centres has little effect on their behaviour. He then proceeded to present his explanation based on the idea that each pair of electrons is formed of one electron state and its exact time reverse. This explained the reason for which superconductivity

could be destroyed in the presence of considerable magnetic impurities as magnetic scattering is capable of destroying time-reversal symmetry. Since the pair phonon exchange coupling is of short range in space, weakly disordered systems, where the mean free path is much greater than the average pair separation in the lattice, were shown to have no effect in lowering T_{c}.

Works by both Anderson and Gor'kov on the theory that superconductivity was unaffected by all but magnetic impurities did not take into account instances of the phenomenon in the presence of strong disorder. Such cases of strong disorder are typically characteristic of alloy materials where atoms from two elements randomly occupy sites in the lattice to varying degree of periodicity if any. Support for the inapplicability of theory to such systems began with work by Maekawa *et al.* [74, 75] in the two-dimensional regime. The authors present corrections to Anderson's model for dirty superconductors based on Fermi energy E_{F} and the electron scattering time τ. The corrections supported a dependence of T_{c} on disorder, with a suppression of the former as disorder is increased.

In 1987, Finkel'stein built on these works when he reviewed the mean field theory of the superconducting transition for homogeneously disordered thin-films [6]. He demonstrated that in these reduced dimensions, disorder caused diffusive transport which enhanced Coulomb repulsion between electrons. According to the BCS theory discussed in Section 1.2, the net attractive potential energy must exceed the Coulombic repulsive energy for a bond to form between electrons. As such, an increase in Coulombic repulsion due to disorder would result in reduced pairing, suppression of T_{c} and a reduced superconducting energy gap Δ [76]. Finkel'stein proposed further adjustments to the theories developed by Maekawa *et al.* and put forward a corrected relationship between T_{c} and sheet resistance $R_{\square}$ in thin films given by

$$\frac{T_{\mathrm{c}}}{T_{\mathrm{c0}}} = \exp^{\gamma} \times \left(\frac{\frac{1}{\gamma} - \sqrt{\frac{t}{2} + \frac{t}{4}}}{\frac{1}{\gamma} + \sqrt{\frac{t}{2} + \frac{t}{4}}} \right)^{\sqrt{1/2t}}, \tag{2.8}$$

where $t = R_{\square}\left(e^2/\pi h\right)$ and γ is a fitting parameter related to the elastic scattering time τ by

$$\gamma = \ln\left(\frac{h}{k_B T_{C_0}\tau}\right). \tag{2.9}$$

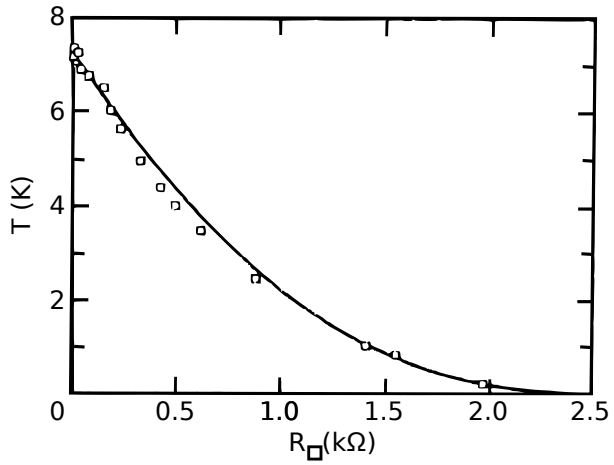

Figure 2.12: Application of the Finkel'stein model to MoGe thin-films. Recreated from original plot by Finkel'stein *et al.* [6]

As can be seen in Figure 2.12, Finkel'stein originally applied this relationship to thin films of MoGe, but applicability has been demonstrated in recent works on amorphous pure materials [77], alloys [78, 79] and compounds, [80]. Of particular interest is the fitting term γ. This has been used as a measure of disorder in the system and can be used to estimate the mean free path through the scattering time.

There is an added significance of the Finkel'stein equation. As can be seen in Equations 2.8 and 2.9, Maekawa and Finkel'stein's work provided a tangible link between a material's sheet resistance, $T_{\rm c}$, the transition temperature of the bulk material $T_{\rm c0}$, and scattering time as a physical measure of disorder in the materials. However, the theory is commonly and successfully applied to describe variation in $T_{\rm c}$ as a result of the evolution of $R_{\square}$ with film thickness, d. Thus the relationship provides a dimension dependent link between disorder and superconductivity which

could be used to characterise disorder in reduced dimensions.

1D disorder and Quantum Phase Slip phenomena

It has been suggested that phase slip phenomenon in 1D superconductivity is influenced by the level of disorder in the host material. Much of the literature on QPS already supports the importance of disorder in the investigation of phase slip phenomena [81, 11, 5]. Materials with a higher degree of disorder will have larger populations of localised electrons, environments in which stronger fluctuations will be observable.

Further to this a one to one ratio between ξ_{GL} and the localisation length ξ_{loc} is believed to maximise fluctuations [5]. In the first experimental demonstration of coherent quantum phase slip, Astafiev explains that the impact of fluctuations is characterised by the inverse number of Cooper pairs in a volume ξ_{GL}^3 of superconductor. This inverse is known as the Ginzburg parameter G_i given by $G_i = (\xi^3 \nu \Delta)^{-1}$ where ν is the electron density of states and Δ is the superconducting energy gap.

Given the link between 2D materials and the increased influence of disorder as thickness is reduced, one would expect a similar dimensional dependence in 1D superconductors. The understanding of the interplay between disorder and superconductivity in 1D is a relatively recent area of investigation and very open to study. Of particular relevance was work published by Graybeal *et al.* [82]. In the same year that Finkel'stein published his corrections to the Maekawa model for 2D superconductors, Graybeal *et al.* presented an investigation into the impact of disorder when moving to the 1D regime. They demonstrated a link between the reduction in the width of narrow superconducting nanowires and the suppression of T_{c} as a manifestation of disorder.

A proponent of the Maekawa form of the Finkel'stein model in 2D, Graybeal *et al.* believe that similar dependencies could be observed for nanowires. Their work demonstrated a link between the normalised variation of T_{c} and nanowire widths w for fixed thicknesses. Continuing the 1/d relationship explained by Ebisawa

et al. [83] the work identifies a dependence on $1/w^2$. Graybeal *et al.* argue two points. First, that superconductivity will be destroyed by the presence of disorder at a characteristic length scale defined by the extrapolation of the trend to the dimension axis. Second, that the $1/w^2$ appears inconsistent with expectation of 1D behaviour, given that in the normal state, the measure of disorder is taken to be resistance per characteristic length [82]. Based on this analysis, they stated that their samples appear to exist on the crossover point between the 2D and 1D regimes. Thus the search for a dependence between T_c and characteristic dimensions in nanowires could not only describe the impact of disorder in the materials in these dimensions, but also provide an indication of whether the dimensions truly fall into a 1D limit.

2.4 Conclusion

Having covered the literature presented in this two-part review, we propose to study two strongly disordered superconductor materials that have demonstrated particular promise in the ongoing investigation into QPS. In particular, we have seen how disorder can be linked to resistivity and ultimately the mean-free path in materials. In Chapter 1 we discussed how the mean-free path can be used in the determination of ξ_{GL}. Thus the mean free path can be used not only to provide a measure of disorder but describe any changes in impact of disorder on superconductivity as dimensions are reduced.

Following a detailed account of the fabrication and measurement methods used in the next chapter, we proceed to present our investigation of disorder in these systems in successively reduced dimensional regimes by applying and extending, where applicable, the theory and models we have discussed in this chapter.

Chapter 3

Materials, Methods & Apparatus

3.1 Introduction

As discussed in Chapter 1 the experiments in this thesis cover thin films, nanowires and nanoscale circuits. As such, the reliable and reproducible fabrication of nanowires from superconducting thin films represents a considerable milestone for the overall thesis. In the previous chapter we considered novel techniques in the field of nanowire fabrication and discussed the benefits of electing to focus on top-down methods. In this chapter we detail the stages and methods used to fabricate our samples during these investigations. Explanations of the supporting techniques and apparatus is included covering Photolithography, Electron Beam Lithography (EBL) and Focused Ion Beam (FIB) as the lithographic processes used to achieve successively smaller features from our films, wires and circuits.

3.2 Substrate Preparation

The choice of substrate material and its preparation for subsequent process can have considerable impact on the success of subsequent fabrication stages. Assessment of the suitability of the material will depend on many factors, but mainly on final goal. For the creation of crystalline films, smooth surfaces and

a gofod lattice match between substrate and functional layers are imperative to achieving crystalline growth. For amorphous film growth, lattice matching is considered for purposes of film adhesion and often where the lattice spacing of one material is insufficiently matched with another, an intermediary material is used as an adhesion layer between substrate and functional material. In this section we describe the substrate selection and preparation used which was the nominally identical for all three investigations presented in our thesis. Any deviations specific to a task are stated.

3.2.1 Considerations in substrate selection

The goal of this thesis is to investigate the impact dimensional confinement on the effects of disorfder in highly disordered superconducting materials. As such, the fabrication processes must create suitable substrates for the creation of uniform films and subsequently nanowire structures. Given the amorphous nature of the films and structures we intend to create, lattice matching between substrate and the deposited superconductor does not take priority. Of primary concern is the adhesion of the deposited materials to the substrate and a smooth surface to allow for uniform structures to be created. The latter is of particular importance where the top-down creation of nanowires is concerned as excessive variation in the surface of the substrate could lead to breaks in these structures.

We describe the three types of substrates that were used for the experimental work in this thesis.

(i) Glass substrates

Lab grade glass slides were used for all work requiring the assessment of film deposition rates and the development of material processes.

(ii) Al_2O_3 substrates

Sapphire die of 10 mm×10 mm were used as substrates in the creation of thin films samples for XPS characterisation of the superconducting films once recipes

had been established.

(iii) Si substrates

All remaining films for the creation of test structures, nanowires and circuit components were deposited on die cut from phosphorous-doped (n-type), 2" single-sided silicon wafers. These are quoted with a resistivity of 8-30 $\Omega\,$cm and are polished to $< 5\,$Å surface variation.

No oxide was grown on the surface of these substrates however a limited native oxide is presumed present. Conductive substrates were selected to provide added protection from Electro-Static-Discharge (ESD) which could damage any nanostructures fabricated on their surface. Substrate conduction was confirmed to be frozen out below the 50 K limit.

3.2.2 Substrate cleaning

All substrates were pretreated using a solvent clean of 60 s sonication in acetone solution followed by an isopropanol rinse and nitrogen dry for 20 s. No oxygen plasma ash was employed at this stage.

3.3 Deposition, Development and Characterisation Techniques for Thin Superconducting Films

For the first step in our investigation, we studied disorder in superconducting thin films. In this section we describe the techniques and procedures used in the creation of thin films of Nb_xSi_{1-x} and NbN. We discuss the equipment used, give an overview of our film development, present fabrication parameters and give the details of our material characterisation.

All films used for the investigations documented in this thesis were deposited using magnetron sputtering. Magnetron sputtering is a physical vapour deposition technique capable of creating nanometer range thin films in a controlled and repeatable manner. The process itself is isotropic in nature which makes it ideal for the deposition of amorphous films whilst affording the user fine control over the thickness of the film.

3.3.1 DC magnetron sputtering

The primary method of deposition used during this thesis is DC magnetron sputtering. Sputtering uses energetic ions to strip atoms from a source target and accelerate them towards a substrate. Once the process chamber is pumped down, the inert gas argon is fed to the vicinity of the target to be sputtered. A voltage is generated between the anode (sample mount) and the cathode (here the magnetron gun), generating a plasma of energetic species from atoms in the process gas. Positive argon ions are accelerated toward the target cathode, where they collide and dislodge atoms from the surface of the source material, provided they collision is sufficiently energetic. The dislodged (sputtered) atoms of the source material travel toward the substrate forming a beam in the direction of the sample mount. They deposit at the surface of the material as part of a growing layer of material adhering to the substrate surface. The deposition rate of the process is dependent on the energy the accelerated ions, in turn dependent on the potential difference between the two electrodes.

Whilst the sputtered atoms form a beam during deposition, the high process pressure involved in sputtering can result in a number of collisions prior to the atoms reaching the sample substrate. These collisions cause broader variation in the angle of incidence at which the sputtered atoms arrive at the surface of the substrate. The resulting characteristic is that sputtering is ideal for the deposition of non-crystalline films and structures. It is also well suited to applications where uniform coverage of stepped features is required, such as in the creation of interconnects and multi-layer device fabrication.

3.3.2 Deposition in SVS-V6000 sputterer

Deposition of films was carried out using an in-house DC magnetron sputter system manufactured by Scientific Vacuum Systems (model V6000). The model features four magnetron sputter sources controlled by two separate power supplies. This setup allows for co-deposition of two materials simultaneously. The system is

dedicated to non-magnetic materials, and is reserved particularly for the deposition of superconducting materials (Al, Nb, Ti), with a Au source for the deposition of contacts.

Substrates are mounted on a rotating water anode stage perpendicular to the magnetron sources. The system does not feature substrate heating, but the sample stage is water cooled to maintain an even temperature throughout deposition. The chamber is pumped down to a base pressure of 4×10^{-7} mbar for all deposition processes.

A 150 W pre-sputter is run for 5 minutes before any deposition process, serving to clear oxide and impurities from the surface of the sources (sputter targets). No material is deposited on the substrates during this period as the sample mount is shielded from the beam by its own shutter.

Once the sources are clean, the substrate shutter is opened to allow deposition. The duration of the deposition is calculated based on the rate of deposition which is ascertained independently for each material. Details of the individual deposition parameters for the required materials are given in subsequent sections according to their related fabrication process. When the required duration is complete, the sample shutter is activated, the beams shut down and the substrates are unloaded.

3.3.3 Developement and deposition of Nb_xSi_{1-x} thin films

Nb_xSi_{1-x}, a binary alloy type II superconductor, has been recommended as a material for use in the investigation of phase slips [58, 3]. Investigations into this material for these purposes have already begun with particular interest in the composition range $x = 0.4$ to $x = 0.45$ [84, 59, 62]. In the paragraphs that follow, we document the development of our own films of Nb_xSi_{1-x}.

Film deposition

The composition of films was approximated using a thickness tuned method of deposition. Glass substrates were patterned with an alcohol based ink to protect an area from deposition. Films of Nb and Si were then deposited onto glass substrates

at a range of magnetron gun sputter powers. Following deposition, the substrates were gently rinsed in isopropanol solution to remove the ink, leaving a trough feature in a procedure similar to that of standard lift-off techniques. The features were then measured using a Dektak XT step profilometer to determine the thickness of the films, and in turn, the deposition rate for each sputter power. Iteration of this process was used to achieve the desired ratio of niobium to silicon by tuning the deposition rate of the constituent materials by thickness, a technique popularly employed in the literature [85, 86, 59]. When the relationship between magnetron power and deposition rate was identified for each material, the final alloy was created using co-sputtering of the two materials at the desired powers. Subsequent measurements were made to ascertain deposition rates of the co-sputtered films.

The finalised alloy compositions were sputtered concurrently onto 10mm x 10mm die of p-type Si(100) and Al_2O_3. As stated before an oxide layer was not deliberately grown prior to deposition of the superconductor. However, since the substrates were previously stored in atmosphere, an insulating native oxide layer can be expected to be present on the surface of Si substrates. All samples were stored in a desiccator cabinet between fabrication and measurements.

Sputter deposition rates in film alloy development Figures 3.6 and 3.2 show the results of the deposition rate measurements for Si and Nb respectively. The data points are the mean average of 7 measurements across each feature for each film. The error bars indicated in the graphs correspond to the standard deviation from the mean. In both cases there is a clear linear dependence of deposition rate on magnetron power, a trend characteristic for this type of deposition method.

Power settings for the magnetron guns were selected to achieve the desired compositions based on the rate of deposition. Table 3.1 shows the power settings and corresponding deposition rates for the alloy compositions developed.

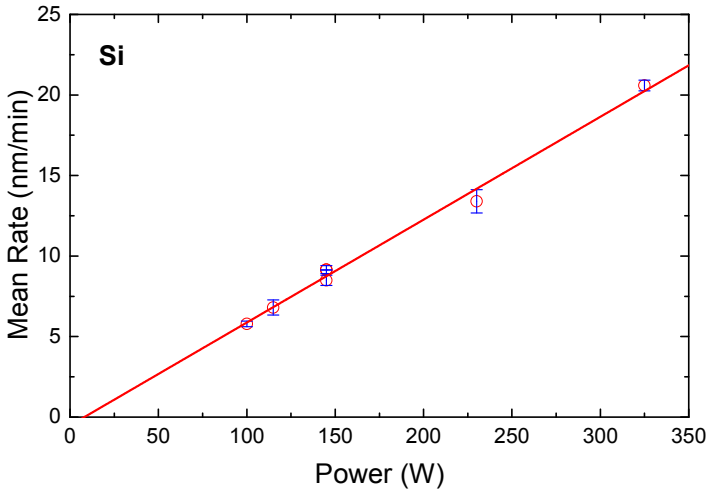

Figure 3.1: Dependence of deposition rate on magnetron power for Si

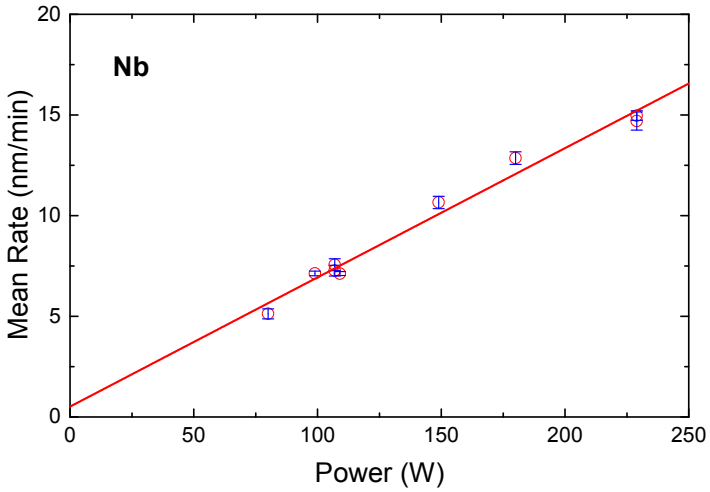

Figure 3.2: Dependence of deposition rate on magnetron power for Nb

Nominal Nb Composition, x (%)	Si Magnetron Power (W)	Nb Magnetron Power (W)	Deposition Rate (nm min^{-1})
44	145	110	15.8 ± 0.6

Table 3.1: Power settings & corresponding deposition rates for sputtering deposition of Nb_xSi_{1-x}

3.3.4 Developement and deposition of NbN thin films

NbN presents an attractive candidate for investigation of dimensional reduction effects. The superconductor has been shown to exhibit values of T_c $16K$ well in excess of pure Nb [87] and has been demonstrated to be relatively uncomplicated to fabricate through a range of methods [87, 88], including sputtering. In addition to its attractive superconducting and fabrication characteristics, it has also recently been demonstrated to exhibit QPS phenomena when patterned into nanowire dimensions [16]. In this section we present the adaptation of a method submitted for review and the resulting films achieved.

Sputter deposition of NbN films

The development of a NbN material composition was based on recipes proposed by Glowacka *et al.* [88] for sputtered NbN. As such, all films were developed and deposited in the SVS-V6000 in house system as with the Nb_xSi_{1-x} films.

Development of NbN thin films

Glowacka *et al.* [88] published a method for the fabrication of NbN whereby the introduction of a small flow of nitrogen (N_2) gas during the presputter stage of deposition induces nitridation of the magnetron target itself. The authors propose several process steps that they have found exert an influence on both the resistivity of the films and the T_c measured.

Typically, higher flow rates of N_2 gas during the deposition process are presented to generate higher resistivity in the sputtered films. However the authors emphasis is a N_2 gas flow 'sweet-spot', that they have identify through cycling the nitrogen flow beyond the intended flow rate until a saturation of the target voltage is observed. This has been shown by Glowacka *et al.* to generate a slight hysteresis in the dependence of target voltage on N_2 flow. Sustained pre-sputter at this point before returning to a recommended N_2 flow rate of 0.7 sccm at an Ar partial pressure of 4 mTorr on the downturn of the hysteretic trend was found to generate films with the highest T_c (14.6 K).

We adapted this method to our own sputter system over the course of several depositions. The saturation of target voltage and hysteretic behaviour were observed in our deposition runs. However, we found that cycling of the N_2 flow exhibited limited benefit for our films. Figure 3.3 shows the temperature dependence of two films of NbN with an identical film thickness of d= 18 nm. One film was sputtered according to our adaptation of the Glowacka method using N_2 cycling whilst film **b.** was sputtered with the prescribed nitridation of the target but without any N_2 gas flow cycling. As can be seen in the plot, film **b.** clearly exhibits a higher value of T_c than the cycled counterpart, albeit with a lower resistance.

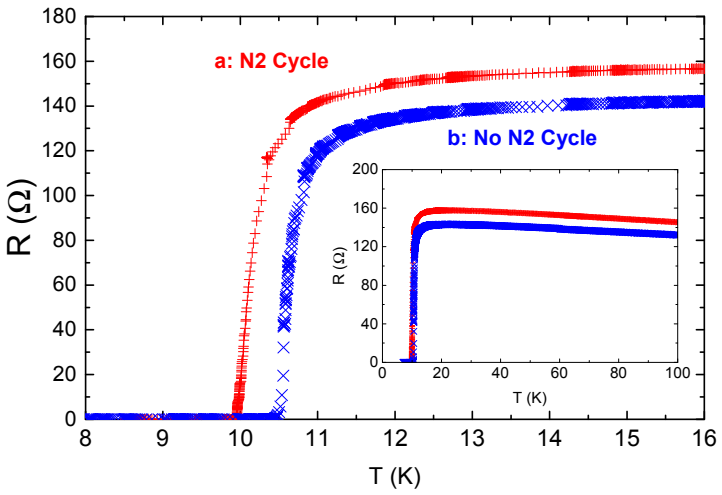

Figure 3.3: Comparison of the effect of N_2 gas flow cycling during the pre-sputter stage in the deposition of NbN thin films. Plot **a.** corresponds to a film deposited using cycling, whilst plot **b.** corresponds to a film deposited without the use of cycling.

N_2 cycling was subsequently omitted from our deposition process. The resulting process parameters were standardised for our NbN films. All films used in this investigation were deposited after pumping to a base pressure of 4×10^{-7} mbar. A Nb target of 99.999% purity is used. The target plasma is ignited with an Ar gas flow before N_2 is added at a 50:50 ratio to a combined gas pressure of 6×10^{-3} mbar. Pre-sputter nitridation of the target is implemented at 150 W sputter power, for

10 mins with the target shutter closed and subsequently 1 min with the target shutter open. The combined gas pressure is then decreased to 5×10^{-3} mbar with a followup pre-sputter of 2 min with the target shutter closed and 30 s with the target shutter open. The sample shutter is then opened for the desired sputter time. The recipe has been confirmed to deposit the nitride at a rate of 9 nm/min, an average confirmed across six readings with a Dektak surface profilometer.

3.3.5 Composition analysis of Nb_xSi_{1-x} and NbN films

The final composition of the films was analysed using X-ray Photon Spectroscopy. The measurements where kindly performed Ms Maddison Coke, a fellow research student in our group, on a Thermoscientific K-Alpha XPS system.

Composition of Nb_xSi_{1-x} Thin FIlms

Element (Primary XPS response orbital)	Nominal Composition in $Nb_{0.45}Si_{0.55}$ Film
Si (2p)	71.33 ± 0.58
Nb (3d)	28.67 ± 0.58

Table 3.2: Mean XPS compositional values for Si and Nb in x= 44 Nb_xSi_{1-x} sputtered films. The analysis here is given as a relative comparison between Si and Nb content.

Table 3.2 shows the mean measured Nb and Si compositions of the Nb_xSi_{1-x} alloy prepared. The original value for x was calculated by volume to be $x = 0.45$. The XPS data indicates values closer to $x = 0.3$. This falls short of the by-volume estimate.

We have considered several reasons for this disagreement. It could be argued that the XPS scan mode used for the analysis was a surface scan and that impurities in the composition at the surface have skewed the result. However, the estimated penetration depth of the surface scan with the administered beam energy of 3 keV is approximately 5 nm. For a film of 20-30 nm thickness, this penetration depth is well into the body of the film. The substrate of the samples measured is Al_2O_3, which would be easily be differentiated and so will not have affected the results. In this case a deep etch scan could give more accurate results, however based on the

thickness of our samples we believed the process to be unsuitable for application here[1].

The difference between the by-volume and XPS compositions given may also be explained by the fact that the by-volume estimate is affected by the interaction of the two elements with the sputtering gas and each other during the co-sputtering process. For the efficient transfer of energy, the atomic mass of the sputtering gas should be matched with the atomic mass of the material. As stated, Ar was used for the sputtering process[2]. The atomic mass of Ar is 39.948 **u**. This value is relatively close to the mass of Si at 28.085 **u**, but only a third of the mass of Nb at 92.90637 **u**. It is plausible that the co-sputtering process resulted in more favourable deposition of Si for this reason.

Despite this difference, Nb_xSi_{1-x} films have been reported to exhibit higher values of resistivity as the fraction of Nb is reduced [89]. Since the literature supports that materials exhibiting higher resistivity provide more favourable environments for QPS phenomena to occur [84], we elected to keep to this composition of film for our investigations. Based on the XPS analysis, the alloy will hereafter be referred to by the composition given by the XPS analysis $Nb_{0.3}Si_{0.7}$ (30%) alloys.

Composition of NbN thin films

Element (Primary XPS response orbital)	Nominal Composition in NbN Film
N (1S)	36.7 ± 1.2
Nb (3d)	63.3 ± 1.2

Table 3.3: Mean XPS compositional values for N and Nb in NbN sputtered films

Table 3.3 shows the mean measured N and Nb compositions in the NbN compound prepared. The results indicate a composition of approximately 63% or $Nb_{0.63}N_{0.37}$[3]. Glowacka *et al.* do not provide a compositional analysis for the films

[1]Deep etching is better suited to thicker samples as, with such thin-films, the resolution and usefulness of a deep etch scan would be very limited. In addition and depending on the material, the ion sputtering used to remove layers during the scan can alter the composition of the sample through selective sputtering.

[2]Only Ar and N are available as process gases on the SVS6000 system used.

[3]An analysis of the relative material composition versus depth was not performed using XPS.

created with their recipe in their publication [88]. However, we have included an XPS analysis for our films for comparison and repeatability in any future works.

3.3.6 Photolithography & pattern transfer

Following deposition, further patterning to create test structures for electrical characterisation was carried out on the Si substrate samples. The Al_2O_3 substrate samples were retained unprocessed for XPS analysis of film composition and crystallinity.

Film measurement substrates were spin-coated in a 500 nm layer of S1805 positive tone photoresist supplied as part of the Microposit S1800 range. The resist was applied at a spin rate of 4000 RPM for a duration of 45 s and was subsequently baked at 115°C for 60 s on a hotplate.

A chrome on soda-lime glass mask manufactured by JD-PhotoTools was used to pattern the measurement structures. Patterns were exposed using a Karl Suss MJB3 Mask Aligner system using a UV light dose of 15 mJ/cm^2. Exposed samples were developed in MF-26A solution for 60 s to reveal the structure pattern.

3.3.7 Reactive Ion Etching of samples

Following the application of the photoresist mask, the unprotected areas are etched away. To remove unwanted material, the sample is exposed to reactive ion etching. RIE is a dry etch technique that employs the use of energetic species generated in a plasma from a mix of precursor gases. A primary difference between RIE and ion beam milling is that the gases used are a mixture of inert and chemically reactive gases that are chosen to tune the etch step to allow for a more selective etch. In certain RIE models a secondary voltage may also be applied to accelerate charged species towards the sample. The application of such a voltage is used to generate a more directional etch characteristic, similar to ion beam milling. All our samples were etched in an Oxford Instruments Plasma Technology NGP80 RIE.

However, the literature supports that it should remain consistent through the film. Cabanel *et al.* [90] found that N content profiles remain consistent in sputtered samples of NbN between the surface of the film and the substrate. In addition, Baunemann *et al.* [91] provide evidence of stable relative compositions of Nb and N with respect to film depth in NbN films prepared using MOCVD. Both studies note a small increase in O at the surface of the films.

Reactive Ion Etching

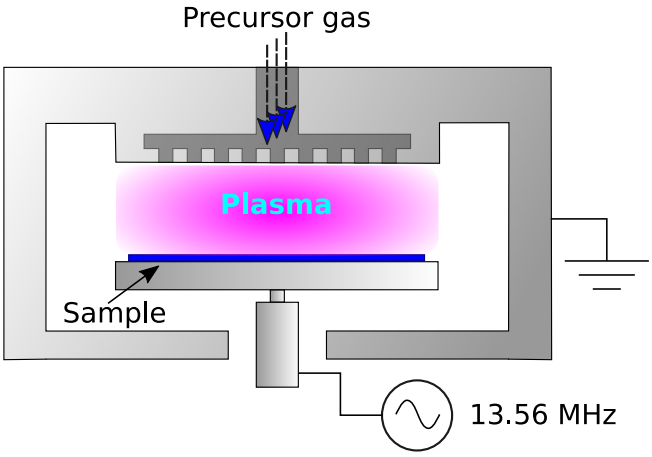

Figure 3.4: Diagram illustrating a typical reactive ion etching setup. Precursor gases are ionised in an applied potential to create energetic species used to etch away material from samples within the chamber.

Figure 3.4 illustrates a typical RIE setup. The sample is mounted on a water-cooled graphite sample plate within a vacuum chamber. The chamber is evacuated and purged with N_2 gas before being pumped to base pressure. The selected gases are pumped into the chamber at their respective pressures. An rf generator is used to create an oscillating electric field of 13.56 MHz between the sample plate and a second plate at the top of the chamber. The field serves to ionise the gas mixture and generate a plasma of reactive species above the sample.

Electrons in the plasma are accelerated between the plates by the rf field. Those that strike the upper grounded plate are absorbed. Those that strike the isolated sample plate generate a large negative charge on its surface. Large ions in the plasma are attracted to sample platen where they react chemically with the material on the sample surface. In addition to the chemical nature of the etch, the interaction will involve a physical component similar to sputtering or ion beam milling, whereby material is knocked off the surface by ions with sufficient

momentum.

Recipes and etch rates

The etching recipes were chosen based on selectivity between materials. For our purposes, we required an etch recipe that would selectively etch Nb based layers whilst minimising the etch rate of the mask materials, S1805 (for photolithographic steps) and PMMA (an electron beam resist whose relevance will be discussed later in Section 3.4). SF_6 gas is popularly used in the RIE etching of Nb [92, 59]. The recipe parameters used, adapted from recommendations by Oxford Instruments are shown in Table 3.4.

Parameter	Set-point
SF_6 flow	14 (SCCM)
CHF_3 flow	35 (SCCM)
Ar flow	0 (SCCM)
O_2 flow	0 (SCCM)
Process pressure	100 (mTorr)
RF power	14 (W @ 13.56 MHz)
Sample temperature	18 (°C)

Table 3.4: RIE recipe parameters for Nb based films.

In order plan the etch process correctly, the etch rates of the recipe must be understood for the different materials to be etched on the sample. The etching rates for Si, Nb, NbN, Nb_xSi_{1-x}, PMMA electron beam resist and S1805 photoresist were ascertained in successive runs on test samples. These etching rates are presented in Table 3.5. The Dektak XT step profilometer was used to measure the thickness of the individual materials before and after etching.

Material	Nominal thickness (nm)	Etch rate ($nm\,min^{-1}$)	Time to etch through layer (min)
NbN	10	23	0.5
$Nb_{0.3}Si_{0.7}$	30	15	2
PMMA	100	53	2
S1805	500	19	26

Table 3.5: Table showing the nominal layer thickness and average etching rates for materials of interest according to the recipe parameters in Table 3.4. The expected time required to etch through each layer is provided for comparison.

The table gives the nominal thicknesses of the respective layers used in each of the materials. Of particular importance is the comparison between the etching times required to etch through the superconductors and the resist materials. We require the process to completely etch away exposed areas of superconductor before the resist mask has been completely etched away and the superconducting structures begin to suffer erosion. Comparing the rates in Table 3.5, both $Nb_{0.3}Si_{0.7}$ and NbN layers will be etched away before the photoresist mask is completely removed. In the case of the PMMA electron beam resist mask, NbN will again be completely etched before the mask. The etch rate of $Nb_{0.3}Si_{0.7}$ is less favourable but should only result in negligible surface etching of the structures by the time the exposed material has been etched away. The resulting structures were twin 90 µm x 2400 µm thin film bars flanked either side by larger contact pads as shown in Figure 3.5.

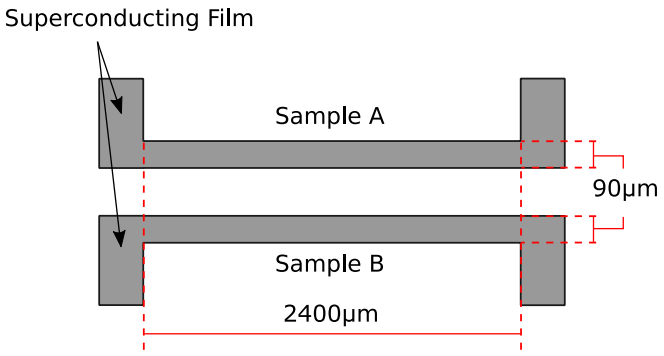

Figure 3.5: Illustration showing structures used for thin-film measurements and and their relative dimensions.

3.3.8 Low temperature electrical characterisation of thin-films

Samples were characterised using a Quantum Design manufactured Physical Properties Measurements System (QD-PPMS). The PPMS is a dry cryostat with field capabilities and a ^{3}He insert that facilitates measurements at temperatures down to 300 mK. Four-point DC electrical measurements of the sample resistance

and were taken through the range 0.5 K - 300 K. A bias current of 0.01 μA was applied to the sample whilst voltage was measured. Field dependence was not investigated.

3.4 Fabrication and Characterisation of Superconducting Nanowires

The second stage of our investigations into understanding the interplay between dimensions and disorder in superconducting materials for QPS is the investigation of nanowires. We fabricated our nanowire devices using top-down, etch based fabrication techniques on the superconducting Nb_xSi_{1-x} and NbN films described in Section 3.3. Existing principles for etch based fabrication methods place an inherent limit on the minimum width dimensions achievable in the fabrication of nanowires. We developed our own method of etch-based fabrication that inverts the traditional process to overcome this limit. We document the reasoning and development of this method in detail in Chapter 5. In this section we describe the fabrication steps and techniques required for its implementation.

Thin films of Nb_xSi_{1-x} and NbN were patterned to nanowires in four main steps. The first, a photo-lithographic step, was used to define a resist mask over an area of thin film to create contact pads and a central region of film. Next, the films are etched using RIE to remove unmasked material. This leaves a large scale structure formed of the contact pads connected to the 'active' central region of superconductor. The third step is the use of electron beam lithography, EBL (discussed later in this section) to define a number of nanowire devices in a resist mask over the active region of the photolithographic structure. The EBL pattern is etched in a further RIE step to electrically isolate nanowires from the bulk material that remains.

3.4.1 Photolithographic definition and etching of large scale patterns

Large scale features are well suited to definition by photolithography. The base structure is a large scale pattern comprising 10 micrometer scale contact pads that allow connection to the active region. Following sputter deposition of the film, samples are coated in S1805 photoresist and exposed according to the recipe described in Section 3.3.6. On development, the remaining resist forms a protective mask that covers the macroscale design structure.

Following the application of the photomask, the samples are etched using RIE according to the recipe parameters given in Table 3.4. The removal of the superconductor layer in the unmasked regions of each sample is confirmed with a continuity check using a handheld voltmeter.

The remaining mask material is removed from the samples using in Microposit Remover 1165 solution bath at 70 °C for 5 minutes. Samples are then rinsed thoroughly with deionised water and dried with nitrogen gas.

3.4.2 Electron Beam Lithography in defining nanowires

The next step in the fabrication process is the isolation of material in the active central region of the large scale patterns to create nanowires.

The cross-sectional dimensions of a nanowire prevent its fabrication using standard UV lithographic techniques. At the time of writing transistor gate widths of 22 nm are reported as industry standard in current microprocessor fabrication by manufacturers such as Intel. However, photolithography to this standard requires the use of unmanned cleanrooms, highly optimised masks and ultra-deep UV machines that are all beyond the capabilities of the facilities available to us. In addition, smaller minimum features will be required for the observation QPS than such processes could afford. There are, however, many alternative top-down techniques that have been used in the fabrication of nanowires, a review and state of the art of which is presented in Chapter 5. Electron Beam Lithography,

abbreviated simply to EBL, is a popular tool in the fabrication of nanowires, in both superconducting and non-superconducting materials.

Electron Beam Lithography

EBL is a lithographic process in which a focused beam of electrons is used to transfer energy into an electron sensitive layer of resist. Unlike photolithographic techniques which indiscriminately expose large areas, EBL is used to directly write patterns into the resist layer, with no requirement for a photomask.

In comparison to photolithography, which is limited by the wavelength of the visible light used (typically UV light in the 365 nm range for a mercury lamp), electrons can have a wavelength of picometer range and, as such, can overcome the diffraction limits experienced with optical lithography. With high resolutions of less than 10 nm reported attainable, e-beam lithography is an attractive tool in the fabrication of very fine featured structures.

A typical EBL system will operate in a similar way to a Scanning Electron Microscope (SEM). A beam of electrons is generated by an electron gun and accelerated towards the sample stage. The acceleration is dependent on the EHT voltage set by the user. The beam passes through arrays of electrostatic magnets that control beam parameters including beam size, stigmation and shift.

The magnet array is also used to deflect the beam within a limited range known as the Write Field (WF). Exceeding the deflection range that determines this field results in aberrations. Any exposure pattern larger than a single write-field is fragmented into a series of write-fields. Since the beam column is fixed and the beam deflection limited to a particular range, a laser interferometer controlled stage is used to move between write-fields during exposure or when traversing the sample.

Process considerations

When designing patterns and using EBL there are several factors that should be kept in consideration in order to optimise results. These are:

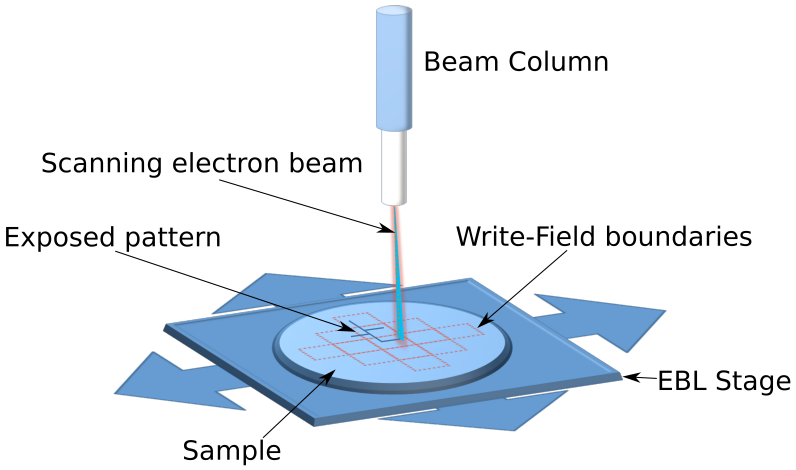

Figure 3.6: Write field pattern fracture for EBL exposure. Patterns are broken down into single exposure fields in accordance with the deflection capabilities. A piezo motor stage is used to traverse between fields during exposure.

(i) Beam energy and proximity exposure

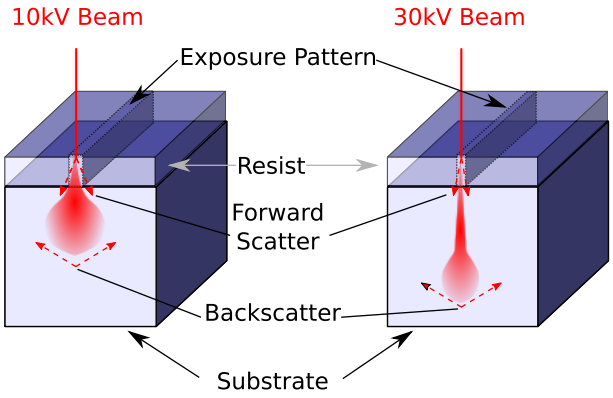

Figure 3.7: Beam scatter and exposure broadening effects for two beam energies. At higher beam energies less scattering is observed resulting in a narrower exposure characteristic.

The selected process voltage will determine the beam energy during exposure. Typical EBL voltage specifications dictate beam energies of between 5 keV and 100 keV. At these energies, the electrons will travel long distances greater before

coming to rest, dissipating their energy through elastic and inelastic interactions within both the resist and the substrate.

The resulting characteristics of the exposure are affected by the selected beam energy, particularly the minimum exposure width that can result. Figure 3.7 illustrates the difference in exposure as beam energy is increased. Elastic collisions can result in electron scattering in the substrate at angles greater than 90°, known as backscattering. In turn, the inelastic interactions can generate secondary electrons which will then also travel into adjacent regions of the resist. A sufficient dose of backscattered or secondary electrons can serve to expose regions adjacent to the desired area, causing what is known as the "proximity effect". Higher energy beams tend to generate less forward scattering whilst simultaneously penetrating the substrate to a greater depth without as much back scattering.

Should lower beam energies be required for more sensitive samples, these effects can be limited through the use of prior experimentation or modelling to optimise exposure by modifying the exposure dose or the pattern design.

(ii) Throughput limitations

Unlike optical lithography, that is capable of exposing areas, E-Beam tools typically expose resist using a pixel-by-pixel serial process. Each pixel of resist requires a minimum number of electrons to be exposed. Given that the electron source can provide a finite current density, the technology has an intrinsic limit as to how quickly a beam can be scanned to expose a pattern.

$$N = \frac{SI^2}{q} \tag{3.1}$$

Eq. 3.1 gives the minimum number of electrons N needed to expose a pixel, where S is the resist sensitivity, I_P is the pixel dimension and q the electron charge.

In turn, for a given dose D, the time needed to expose an area A, using an electron beam current of I, is given by

$$T = \frac{DA}{I}. \tag{3.2}$$

In addition to the minimum exposure requirements, coulomb repulsion of the electrons in the beam at higher intensities can defocus the beam and limit the attainable resolution. This again places upper limit restraints on the use of higher beam intensities to increase throughput. Several approaches have been developed to help overcome these limitations. These include the use of multiple beam sources to allow parallel exposures, broadening and shaping beams of higher intensity to expose full rectangular features as oppose to pixels, and increasing the sensitivity of the resists used.

Although EBL is not suited to high throughput processes due to its pixel by pixel nature, it is an important tool in the fabrication of finely detailed experimental devices and in the small batch processing of special purpose chips.

(iii) Charging

The process of patterning using a beam of negatively charged particles can result in the problem of substrate charging. If the substrate is not well grounded to provide the electrons with a low resistance path to ground, it will slowly become negatively charged. Such an effect serves to defocus the pattern due to repulsion between the substrate and the electrons that form the beam. As such surrounding areas may experience a light exposure due to the defocused beam.

Although modern systems account for this effect, with wafer mounts electrically grounded once in position beneath the beam column, charging may still occur if the wafer itself is not in sufficient contact with the wafer mount.

High resolution electron beam resists and developers

Lithographic resists are typically polymeric solutions whose solubility in a developer is proportional to their molecular weight. Exposure to an electron beam will cause cross linking of polymeric chains for a negative tone resist, resulting in a higher molecular weight, or chain scission for a positive tone resist resulting in a

lower molecular weight.

(i) PMMA (Polymethyl Methacrylate)

PMMA is the most commonly used high resolution electron beam resist. At lower exposure doses it can be used as a positive tone resist, however modifying the dose factor by one order of magnitude in line dosing allows PMMA to be used as a negative tone resist.

Depending on the tone, exposure to an electron source increases or decreases susceptibility to the resist developer, typically a 1:3 methyl isobutyl ketone (MIBK): isopropanol (IPA) solution. More recently, studies have shown that a 3:7 solution of water to IPA can be used to achieve even higher resolution than was previously achieved using the MIBK/IPA mixture. Yasin *et al* reports a $\sim$ 40% increase in sensitivity and exposure dose latitude, along with a $\sim$ 20% improvement to contrast, achieving minimum feature size of 16 nm in grating structures[93].

(ii) ZEP

The ZEP series is a range of high resolution, positive tone resists released by the Zeon Corporation. The series offers superior sensitivity and etch resistance to PMMA and in turn shows promise in matching and surpassing the highest resolution reported for PMMA. Developers for the ZEP520 family are typically n-Amyl acetate and o-Xylene for higher resolution, whilst higher sensitivity may be achieved using a 4:6 mixture of 2-Butanone/Methyl Isobutyl Ketone[24]. The ZEP7000 family is suited to applications including 50kV processes. Developers for this family are ZED 400 for high sensitivity and ZED450 for fine patterning, the complication with the later being the necessity for spray application [25].

(iii) HSQ (Hydrogen Silsesquioxane)

HSQ is a negative tone resist in which exposure to an electron beam causes cross-linking. The resist has a reported minimum feature size of 6nm [26]. Like PMMA and ZEP it is spun onto a sample before being set on a hotplate. Film thicknesses of between 30 and 180nm may be achieved dependent on the concentration of the

solution and the spin speed. The resist may be thinned using methylisobutylketone (MIBK) and is typically developed in tetramethyl ammonium hydroxide (TMAH). Electron beam penetration into the resist may be modulated between 35 nm to more than 175 nm by modulating beam energies between 200 eV to 100 keV.

Substrate preparation for EBL

Prior to exposure, all substrates must be prepared through cleaning and deposition of the resist layer. Following the removal of the photoresist layer described in Section 3.4.1, substrates cleaned with an acetone-IPA wash as per described in Section 3.2.2 prior to a dry bake on a hotplate for 2 minutes at 180° Celsius. They are subsequently coated in a 2% PMMA 950 using spin-coating. The resist is applied to substrates and spun at 2000 rpm for 45 s. The coated substrates are subsequently baked on a hotplate at 180° Celsius for 5 minutes to expel the solvent and harden the resist. The process creates a 100 nm layer of resist in accordance with recommendations by the resist supplier, Microchem.

The Raith150$^{\mathbf{TWO}}$ Electron-Beam Lithography system

All EBL exposures for this thesis were performed in the in-house Raith150$^{\mathrm{TWO}}$ EBL System. This is a highly automated, ultra-high resolution direct-write lithography tool, capable of defining features below 10nm. The system incorporates a Laser Interferometer Stage capable of positioning down to 1nm, and a wafer capability of up to 8", on electrically grounded wafer mounts.

The entire system is housed within a temperature controlled, electrostatically shielded and counterbalanced enclosure, to limit environmental influences, such as mechanical vibrations, that may adversely affect the system during exposure.

Electron beam exposure

An exposure pattern is prepared that defines tracks over the active central region of the photolithographically defined structures. These tracks will be etched to electrically isolate regions of the superconductor in order to create nanowires. The pattern used and its development are discussed in more detail in Chapter 5.

Dedicated design features are incorporated into both photolithographic and EBL patterns for the purpose of alignment between the two process layers. The EBL contains predefined alignment procedures that allow it to identify these features and optimise the accuracy of the exposure overlay.

Based on the sample dimensions, the EBL divides the pattern into write fields and calculates the related exposure paths and times required to expose the pattern. The pattern is then exposed in the resist layer on the sample. Although settings will vary depending on exposure, Table 3.6 illustrates the typical exposure parameters for designs exposed during this investigation.

Parameter	Typical Setting
EHT (kV)	30
Beam Aperture (μm)	30
Beam current (pA)	276
Spot size (nm)	20
Working distance (Focal distance in mm)	7.5
Write field dimensions (μm)	100 x 100

Table 3.6: Typical exposure parameters used in the exposure of our nanowire devices.

Exposure development and etching

After exposure, all samples were developed according to the manufacturer's recommendations. Samples are developed in a 1:3 MIBK/IPA solution for 30 seconds. The developed samples are then rinsed with IPA to stop any further action of the developer, before being dried using nitrogen gas.

Samples were subsequently etched using RIE according to the etch parameters in Tables 3.4 and the etching times shown in 3.5 to define the nanowires in the film. The remaining PMMA was then removed in a Microposit Remover 1165 bath at 70°C for 5 minutes. Finally, the samples were rinsed thoroughly in deionised water to remove any solvent residue and dried using nitrogen gas.

3.5 Fabrication of an Integrated QPS Nanowire Circuit Device

In Chapter 7, we present a study into the feasibility of incorporating our nanowire devices into an circuit device adaptation of Mooij's voltage-biased QPS junction [3]. A detailed discussion of the considerations supporting the final design of the circuit, including models to support the selection of feature dimensions is included in Chapter 7. A significant amount of design and process optimisation was undertaken to achieve the final results presented both here and in Chapter 7.

A circuit diagram of the QPS nanowire circuit device that we fabricated is shown in Figure 3.8 **a.**. The circuit comprises four measurement lines that connect to a central inductor channel. At a point half the distance between the two central connections, the width of inductor line is reduced across a nominal length-scale of 1 μm to form a nanowire region. The final design for our chips comprised two columns of twelve such devices, with two four-point material characterisation structures at the top of each column.

Here we detail the fabrication process steps for the device, as illustrated by the diagrams in Figures 3.8 **b.** to **d.**.

3.5.1 Fabrication of the thin-film CrO_x meander resistors

The first step in device fabrication is the fabrication of the resistor structures, as indicated in Figure 3.8 **b.**. Each connection to the inductor line and nanowire region is made through a high impedance thin film series resistor. The significance in the use of high series impedance to the observation of QPS phenomena is demonstrated in the characteristics of simulated data in Section 7.3. It has also been proposed that a high impedance environment will drive superconducting nanowire systems into a weakly superconducting state [94, 59] close to the superconductor to insulator transition (discussed in Chapter 4). In this regime, QPS phenomena are expected to be more easily observable [5].

The thin film resistors were fabricated using a lift-off procedure with EBL. We

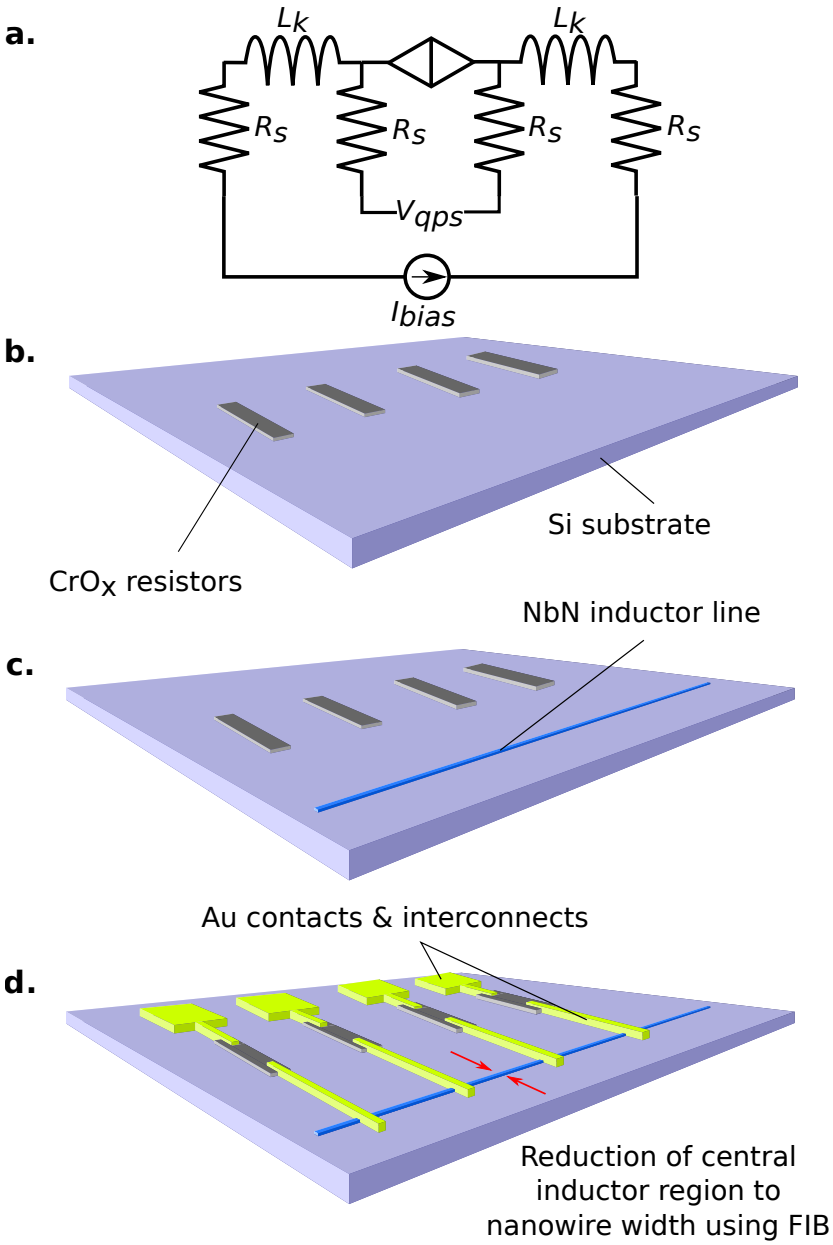

Figure 3.8: **a.** Circuit diagram for the QPS nanowire circuit device and **b.-d.** diagrams illustrating the successive stages involved in the fabrication of the QPS Circuit device.

designed meander thin film resistors using a Matlab algorithm to maximise the area coverage within a single EBL write field. We elected to use a meander pattern for our resistors instead of a bar structure in order to maximise the resistor surface area. This was done to reduce thermal power dissipation and the subsequent device heating associated with high impedance structures, according to $P = (I^2R)/A$. The meander pattern also served as a means by which we can maximise the use of chip space in comparison to standard bar structures.

Substrates were coated with PMMA 950K A2 electron beam resist prior to exposure of the resistive structure. Given the large dimensions of the meander resistors, the resistor pattern layer was exposed using a 10 kV, 60 µm large aperture EBL exposure. Samples were subsequently developed in 1:3 MIBK:IPA solution for 30 s before drying with N_2 gas.

We have used CrO_x as the resistor material for our samples. The high impedance nature of the film and performance at He temperatures makes it an attractive material for on-chip resistors. We document the low temperature transport characteristics and fabrication details of the film in [17]. CrO_x thin-films were deposited to a depth of 100 nm at an O/Cr ratio of 0.37 according to the recipe documented in our report [17]. The deposited films were then developed in Microposit Remover 1165 solution bath at 70 °C for 5 minutes. Remover residue was cleared using deionised water and the samples were dried using N_2 gas. The resulting resistor structures had values 100 kΩ by design.

3.5.2 Fabrication of the NbN inductor line

The second stage in the process was the fabrication of the inductor line. This is illustrated in Figure 3.8 **c.**. Each device incorporated a 900 µm × 100 nm inductor line, defined using EBL. The inductor pattern was exposed in 100 nm PMMA 950 A2 using a 10 kV beam with a 30 µm aperture. The samples were developed as detailed in Section 3.5.1.

A NbN thin-film layer was deposited using magnetron sputtering to a depth of 10 nm, according to the recipe described earlier in this chapter in Section 3.3.4.

Our reasons for the selection of this material and the thickness of the film are given in Section 7.3.4 of this document. The unwanted film was subsequently removed using lift off in Microposit Remover 1165 as described in Section 3.5.1, leaving the inductor line.

3.5.3 The Au interconnections

The final two steps are illustrated in Figure 3.8 **d.**. Before the reduction of the inductor line to nanowire dimensions, a final EBL step was used to define the Au interconnects and connection pads on the device. Whilst features as large as connection pads would normally be fabricated using a photomask, we executed this step using EBL for the purpose of creating our prototypes. The interconnect layer was exposed in 300 nm of PMMA 950 A4 resist using a 10 kV beam voltage with a 120 µm aperture in order to reduce exposure times. Samples were developed in MIBK:IPA as described in Section 3.5.1.

Gold was sputtered to a depth of 120 nm using magnetron sputter deposition to ensure step coverage of existing features. The unwanted film layer was removed using lift off in Microposit Remover 1165 as described in Section 3.5.1.

3.5.4 Reduction of the inductor line width using neon FIB

The nanowire features for the circuit were created using focussed ion beam milling on a Carl Zeiss Orion Nanofab Multibeam tool. Figure 3.9 illustrates a typical FIB system setup. The principle of the FIB is similar to that of the SEM. A beam of ions, Ne or He for the Orion, is generated at the source and accelerated through a series of electrostatic lenses. The first lens serves to form the beam and control the beam current. After collimation through a physical aperture, the ion beam passes through a second lens magnet array which is used to deflect the beam, allowing it to be scanned across the sample. The octopoles within the column are magnet arrays that are used for beam forming, the adjustment of beam stigmation and alignment. As the ions strike the sample, they dislodge atoms from it's surface in a sputter-like process. Using this process, the FIB allows for fine detailed machining of samples, with sub-5 nm feature sizes reported as standard.

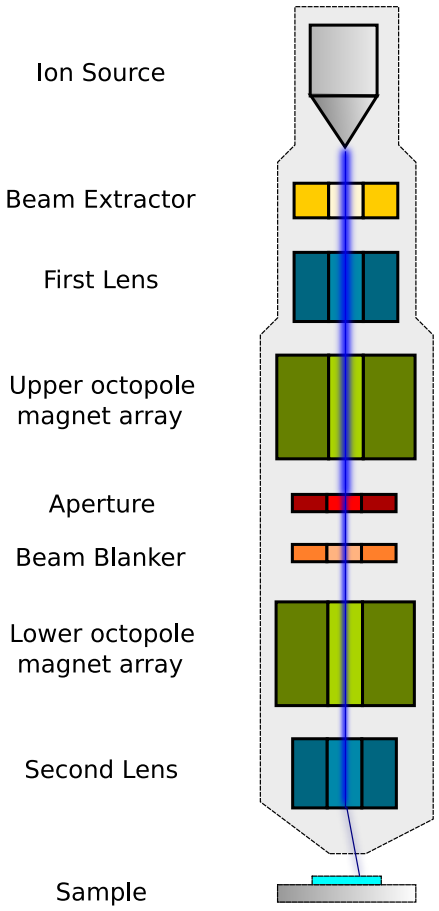

Figure 3.9: Illustration showing a typical FIB system. A beam of ions is generated and accelerated through a series of electrostatic lenses towards a sample.

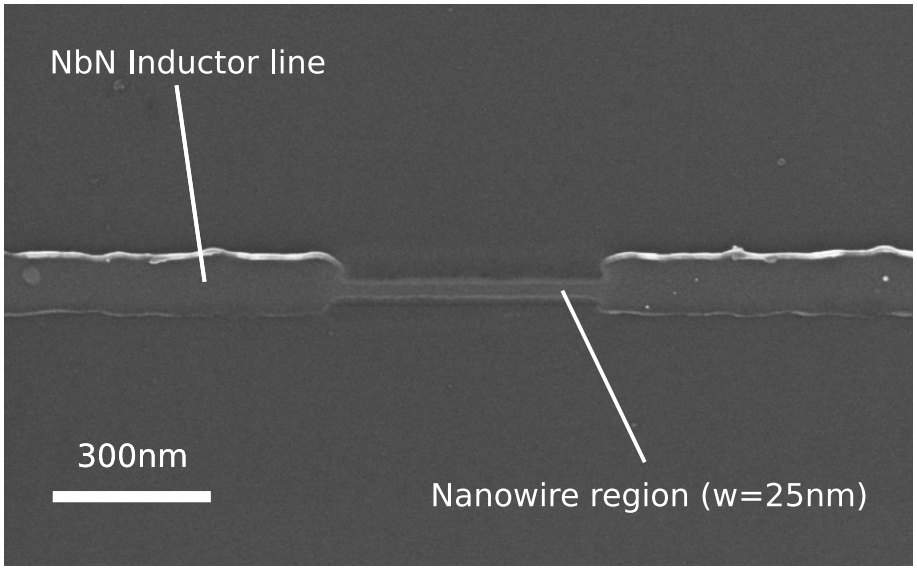

Figure 3.10: He FIB image of a 25 nm× 1µm section of inductor line after reduction using a Ne focussed ion beam.

The reduction to nanowire width was performed with the kind assistance of Dr James Sagar, UCL. Samples were prepared using a 200 W low power Ar ashing step for 30 s to remove organic debris before loading into the system. A Ne beam was used to create wires ranging 20 nm to 35 nm in width. Figure 3.10 shows an example of a section of inductor line after reduction.

3.6 Summary

In this chapter we have provided an overview of the fabrication techniques, methods, design and development processes that were used during our investigations. We have discussed the development of our superconducting thin film compositions, detailed how these were reduced to nanowire structures and then subsequently discussed the method used to fabricate our prototype devices.

In the chapters that follow we document the characterisation and measurement of our superconductors in thin-film, nanowire and integrated circuit form at low temperature.

Chapter 4

Low-Temperature Characteristics of Disorder in 2D Films of Nb_xSi_{1-x} & NbN

4.1 Introduction

A thin-film is defined as a sheet of material whose thickness is small in comparison with its length and width. A two-dimensional thin film is one where thickness is lower than a characteristic length. In superconductivity the coherence length is often used as the benchmark for this characteristic length. Within such films it is possible to observe interesting deviations from bulk transport characteristics and superconducting behaviour as this limit is approached.

Superconducting thin films are used to fabricate the fundamental components of Josephson junctions and Superconducting Quantum Interference Devices (SQUIDs). As such, the physics of these films supports both metrology in the Josephson voltage standard, and magnetometry. The sensitivity of these films to electromagnetic radiation has seen their incorporation into bolometers as a replacement for metal absorptive layers [95, 96, 97, 98].

As discussed in Chapter 1, one of the fundamental characteristics that becomes

more dominant as dimensions are constrained is disorder. In order to predict and optimise the impact of disorder in a one-dimensional system, we look first at disorder in a two dimensional system. Whilst previous studies have focussed on single element metallic films such as Al and Ti [12, 11, 99] as simpler systems with less disorder, considerable interest has been given to alloys and nitrides as a means of enhancing disorder. In this chapter we investigate the impact of disorder in thin-films of Nb_xSi_{1-x} and NbN, the superconductors selected for our purposes in Chapter 2. The recipe development of these materials and how they were patterned into measurement structures are detailed in Section 3.3.3.

We look at the interplay between disorder and the electrical characteristics of the materials and apply known models to extract parameters such as the mean free path, the Ioffe-Regel parameter and coherence lengths in the material.

4.2 Temperature Dependence of Resistance in Nb_xSi_{1-x} and NbN Thin Films

In this section we extract estimates of disorder in superconducting non-metallic thin films using the theories we have introduced in Chapter 2. Here, we use non-metallic in reference to the insulator like behaviour exhibited by the films prior to their superconducting transition. One of the simplest ways to characterise disorder as dimensions are reduced is to consider how this reduction affects the temperature dependence of the material's resistivity. We do this for a range of films in two materials of interest, $Nb_{0.3}Si_{0.7}$ and NbN. We then analyse the dependence of T_c on sheet resistance and film thickness d to extract parameters leading to estimates of the mean free path for our materials.

Thin superconducting films undergo transitions at temperature T_c which is typically lower than that of the bulk T_{c0}, due to enhanced quantum and thermal fluctuations [7]. As T decreases from T_{c0} and tends toward T_c, the order parameter is believed to increase. However fluctuations due to vortex flow or thermal influences

still prevent long range order being established within the system. When T falls below T_c vortex-antivortex pairs are formed, reducing or nulling the corresponding fluctuations. Furthermore, as T tends to 0 K thermal effects are also suppressed. In this section we discuss the dependence of resistance in these superconductors on temperature and focus particularly on their behaviour near and below the critical temperature T_c.

4.2.1 Temperature dependence of sheet resistance $R_\square$ in Nb_xSi_{1-x} thin films

Figure 4.1 shows the variation in sheet resistance with temperature for the $Nb_{0.3}Si_{0.7}$ alloy developed in Chapter 3. The evolution of this dependence is presented for films of various thickness, and for temperatures ranging through the superconducting transitions of the films.

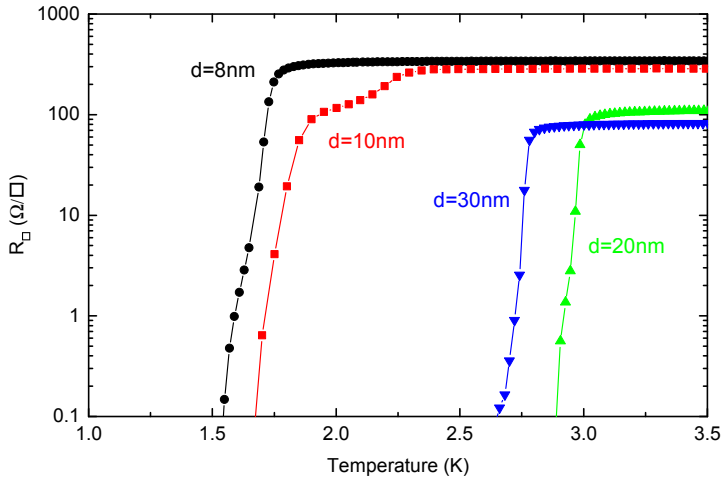

Figure 4.1: Variation of temperature dependence with film thickness d for thin film structures of $Nb_{0.3}Si_{0.7}$ with d=8nm, 10nm, 20nm and 30nm.

The sheet resistance in the normal state $R_\square$ just prior to the superconducting transition, scales with thickness d. This may be explained by considering a thin square sample of the superconductor with dimensions $l \times w \times d$ and resistivity ρ, where the resistance R of a sample is given by $R = \rho l/wd$.

For the case of a square piece of the material $l = w$. The sheet resistance of the film is therefore inversely proportional to the sample thickness, since the resistivity of the material is expected to remain constant here, and is given by $R_{\square} = \rho/d$.

The onset of the superconducting transition and the critical temperature T_{c} itself also scale with the film thickness. This is true for films apart from the 20 nm and 30 nm samples. Interestingly, Figure 4.1 shows that the T_{c} for $d = 20$ nm is higher than where $d = 30$ nm. This could be due to defects that were introduced in the corresponding run of deposition for the 30 nm film or an excess of Nb in the 20 nm. In the following section we explain that it is in fact the 20nm film samples here that exhibit values of T_{c} higher than those expected. It should be noted that criteria used to extract T_{c} are susceptible to non-ideal characteristics in data. Here, we define T_{c} to be $(T_{R=0.9R_{\mathrm{N}}} - T_{R=0.1R_{\mathrm{N}}})/2$. Such a definition may be affected by features such as the 'shoulder' in the temperature dependence of the 10 nm film in Figure 4.1[1].

A broadened transition characteristic may be seen for the film samples in Figure 4.1. A theoretical transition from the normal state to a superconducting one is very sharp. Experimentally, however, this is typically only observed in measurements of relatively pure bulk 3D superconductors. The broadening of the transition here is interpreted as an indicator of impurities in the samples measured [35]. Work presented by Ponta *et al.* models 2D granular systems and discusses the role of disorder in superconductors with different intergrain couplings. In their model, disorder leads to a distribution in I_{c} in the material. Whilst modelling strong-links, the grains in the system are seen as regions of varying I_{c}, which are said to govern the behavour of the temperature dependence. However, in Ponta *et al.*'s modelling of weak link systems, the temperature dependence is believed to be governed by variations in coupling between the physical grains. The results of the study suggest that in such systems, broad, smooth transitions are indicative of strongly defined

[1] At this stage we are unsure of the origin of this feature although this may be that processing of this sample introduced impurities causing variation in the T_{c} for different regions of the d=10nm structures.

current paths whilst stepped transitions, such as those observed for the 8 nm and 10 nm $Nb_{0.3}Si_{0.7}$ films, suggest intra-grain weak-links along the current path [100]. Such an explanation could indicate that these films exhibit a higher level of disorder than samples by other groups with the same alloy composition. We can expect that the influence of intra-grain weak-links would be more prominent in measurements on films with smaller thickness d.

4.2.2 Temperature dependence of sheet resistance $R_{\square}$ in NbN thin films

Figure 4.2 shows the resistive transitions in the graphs of temperature dependence of resistance in NbN thin films. Details of processing and measurement for these films are detailed in Section 3.3.4 of Chapter 3.

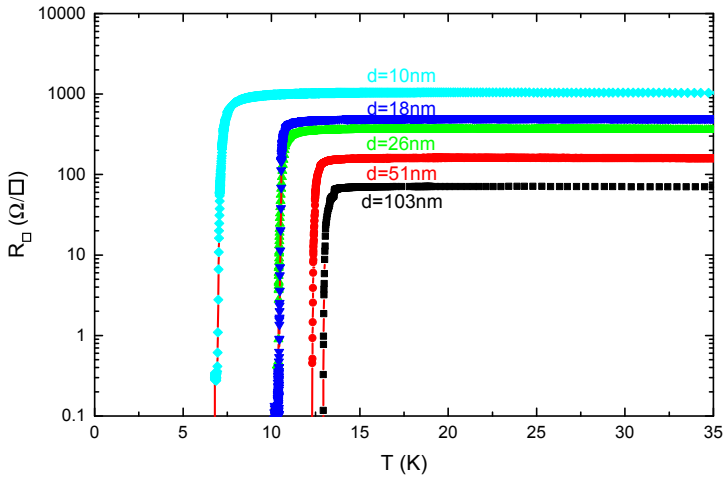

Figure 4.2: Variation in the temperature dependence of resistance with film thickness, d, for thin films of NbN. The samples with d=103nm, 51nm and 18nm are from un-patterned films whilst the samples with d=26nm and 10nm show the dependence in films of the same composition after patterning into bar structures.

The plot shows the temperature dependence for five films. Three of these were un-patterned thin films in an "as deposited" state, 4-point connections wire bonded directly to film. The measured resistance data of these films was converted into sheet resistance using conversion factors described by Smits [101]. The remaining

two, with thickness d of 26 nm and 10 nm, were patterned bar structures of the same composition. These were measured after patterning into 90 µm×2400 µm twin bar structures identical to those used with the Nb_xSi_{1-x} alloys. A range of film thicknesses was investigated and presented in the plot. All films show a clear scaling of T_c and $R_\square$ with film thickness[2].

The NbN films exhibit sharper superconducting transition characteristics than those observed with Nb_xSi_{1-x} films, with no crossover between film samples at lower temperatures, as was observed in Figure 4.1. The high values of T_c represent an attractive material attribute for the purpose of investigating low dimensional behaviour as these make it experimentally easier to work in a temperature range well below the region near T_c where thermal fluctuations have a more prominent influence on material behaviour than quantum.

4.3 Dependence of the Superconducting Transition on Film Thickness in Nb_xSi_{1-x} and NbN Thin Films

4.3.1 The quantum of resistance and the superconductor to insulator transition

It has been proposed [5] that a material tuned close to its Superconductor-to-Insulator Transition (SIT) provides a favourable environment for the observation of QPS phenomena. An SIT is characterised by a change of sign from positive to negative for the gradient of the curves at temperatures below T_c. This gradient is referred to as the Temperature Coefficient of Resistance, (TCR), as described by Schneider *et al.* [102]. The parameter is defined by $T_{CR} = dR/dT$ [77, 79]. By definition a $TCR < 0$ is characteristic of samples in the insulating phase whilst a $TCR > 0$ is indicative of the metallic phase [79].

Superconductor to insulator transitions have been documented in different

[2]It is noted that T_c and $R_\square$ do not appear to scale as expected between the 18 nm and 26 nm thick films. An mismatch in the Smits conversion of the data for the 18 nm sample could have indeed skewed the $R_\square$ values for the sample but would not have impacted on the onset of T_c. It is possible that either of these samples exhibit a slight deviation in their composition in comparison to the others in this set.

materials [9] and more recently for other compositions of Nb_xSi_{1-x} [79]. This disorder induced phase transition is accessed either by tuning the thickness of the film or by introducing greater disorder in the material itself. Fisher describes that this threshold becomes a purely quantum critical point [7] as the temperature tends to absolute zero. His phase diagram, adapted for Figure 4.3 indicates that the threshold of disorder scales with temperature T and applied magnetic field B.

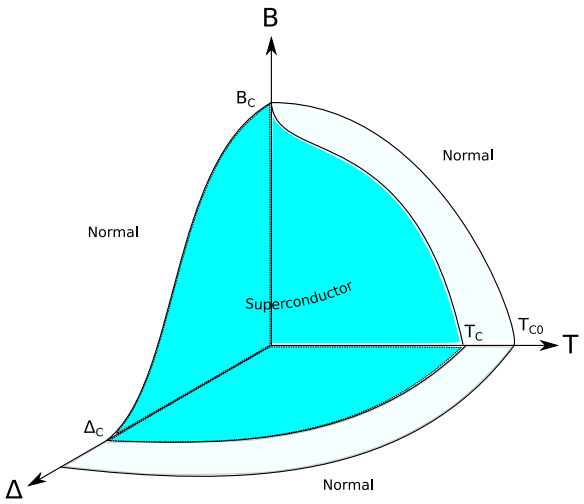

Figure 4.3: Adaptation of Fisher's phase diagram for a disordered superconductor. Here, Δ is used to denote disorder in the material whilst T and B are temperature and applied magnetic field respectively. As disorder is increased, both the critical temperature of reduced superconductor T_c, and the critical temperature of the bulk material, T_{c0}, are seen to scale towards the origin [7].

It was traditionally theorised that such SITs were exclusively observed when the normal state sheet resistance of a thin film, just above the critical temperature, exceeded the quantum of resistance given by the relationship $R_q = h/4e^2 = 6.455\,k\Omega$.

Figure 4.4 plots the temperature dependence of $R_\square$ for **a.** $Nb_{0.3}Si_{0.7}$ and **b.** NbN thin films. Here we do not observe a SIT but both materials do show a tendency towards SIT behaviour as d is reduced. The thinnest films for each material exhibit values of $R_\square$ below the quantum of resistance. As such, the fact

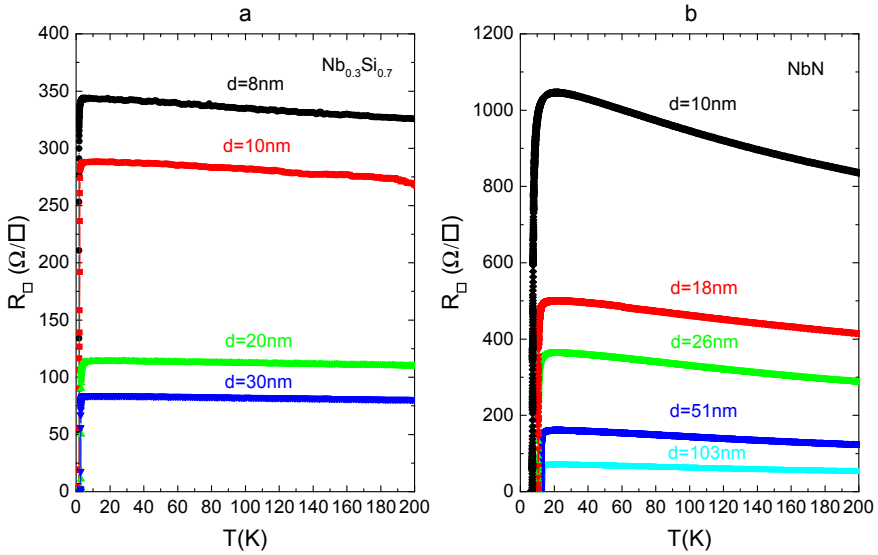

Figure 4.4: Plots showing increasingly insulating behaviour in the temperature dependence as film thickness is reduced for **a.** $Nb_{0.3}Si_{0.7}$ films and **b.** NbN films.

---

that we do not observe an SIT in these films is consistent with what has been suggested in the literature regarding R_q, since the sheet resistance of the thinnest films is approximately $1\,k\Omega/\square$ [3]. These two points indicate that, whilst the film thicknesses characterised here are still within the superconducting phase of the material, the films are nearing a thickness range where an SIT might occur. Further analysis in the following sections will provide an indicator to predict how close these films are to the value of d_c for this composition of the NbN compound and the respective SIT.

4.3.2 Dependence of the critical temperature T_c on film thickness d in Nb_xSi_{1-x} films

The critical thickness d_c is the point at which the dimension comes within the length scale of the Ginzburg-Landau coherence length and, as such, is an important

[3] It should be noted that this is a direct comparison of a sheet resistance value to a value of sample resistance. This is done following comparisons made in the literature for similar studies [77]. However, we acknowledge that such a comparison will have its limitations

estimator of ξ_{GL} and a measure of disorder.

A well established method in the literature for the purpose of identifying d_c [103, 104, 105, 106, 79] is the study of the evolution of T_c with d for a particular film composition. The critical temperature of thin superconducting films has been found to scale inversely with thickness in 2D systems [9, 77, 79] . Plotting T_c against 1/d for separate film compositions can be used to predict both d_c and T_{c0} (the critical temperature in bulk films of the material) for films of set composition. Here T_c is defined as the temperature corresponding to the maximum in the derivative of the $R(T)$ curve.

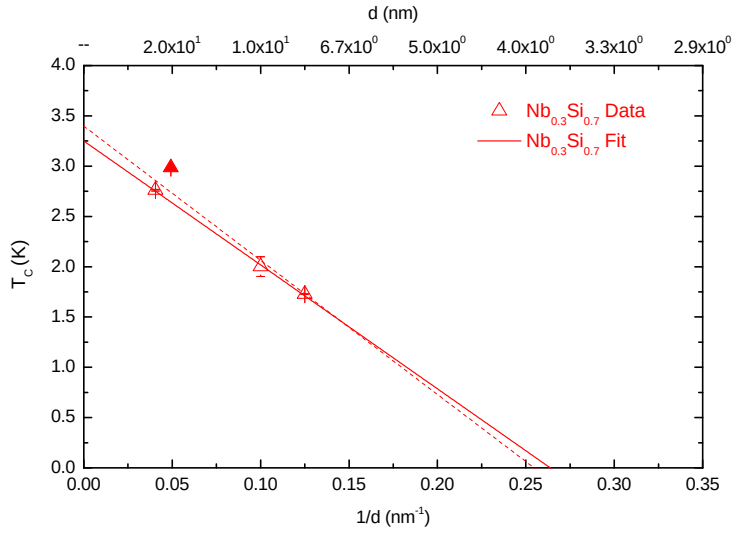

Figure 4.5: Dependence of T_c on inverse film thickness, d, for $Nb_{0.3}Si_{0.7}$ films. The hollow red triangles represent the $Nb_{0.3}Si_{0.7}$ data whilst the solid red indicates fit to the data using linear regression. The solid red triangle represents a data point that appears out of trend and has been omitted from the linear regression. The broken red line indicates the fit to the data when the data point indicated by the solid triangle is included

Figure 4.5 presents this relationship for data from $Nb_{0.3}Si_{0.7}$ films. A linear regression using the least mean square (LMS) method has been applied to the data as indicated by the fit lines in the plot[4]. The point at which the linear fit

[4]We define T_c as $(T(0.9R_N)+T(0.1R_N))/2$. Other definitions of T_c have not shown a substantial variation in the plot characteristic.

crosses the T_c axis is taken to predict the value of T_{c0} in a bulk film of the same composition. Similarly, the crossing point on the $1/d$ axis predicts the critical thickness d_c at which one would expect to see a transition to insulating films.

In section 4.2.1 we discussed the unexpected behaviour and T_c values in the resistive curves for $d = 30\,\text{nm}$ and $d = 20\,\text{nm}$ films shown in Figure 4.1. In Figure 4.5 the value of T_c corresponding to the $d = 20\,\text{nm}$ film sample does not fit the linear characteristic exhibited by the rest of the data. The broken red line indicates a linear fit to the data when including the datapoint for the 20 nm film whilst the solid red line indicates the linear fit to the data when the same point is omitted. Only slight variations are observed for T_{c0} and d_c when compared to the s, however the inclusion of this datapoint generates an adjusted R^2 of 0.886. Omitting this data point from the fit generates an improved R^2 value of 0.999. This could be taken to support the argument that the corresponding sample set for the $d = 20\,\text{nm}$ films could inded be an outlier and have a different composition to the other samples in the measurement.

The resulting reduced data set for the $Nb_{0.3}Si_{0.7}$ film samples shows a linear trend. The relationship between T_c in K and d in nm for these films is found to be $T_c = 3.25 - (12.32/d)$. Extrapolation of the relationship to the axis predicts a T_{c0} for the bulk films of 3.25 K with a standard error of 0.02 K for this particular alloy composition. The fit predicts a critical thickness of 3.8 nm, a value that is in good agreement with reported values of ξ_{GL} [107, 78, 89]. These values correspond to the linear fit indicated by the solid red line.

4.4 Dependence of the Superconducting Transition and Critical Temperature T_c on Film Thickness d in NbN Thin-Films

We present the relationship between the superconducting critical temperature T_c and film thickness d for the NbN films in Figure 4.6. The plot shows a clear linear trend and inverse dependence of T_c on film thickness. A LMS linear regression has

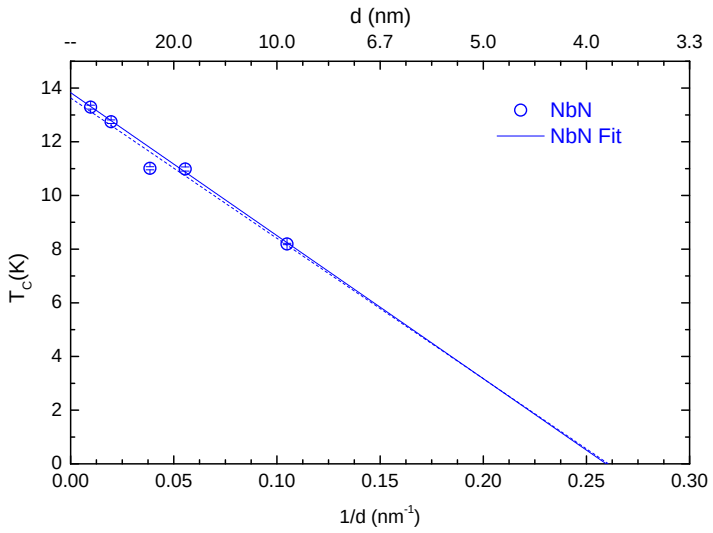

Figure 4.6: The relationship between T_c and 1/d for thin films of NbN with the top x axis indicating the corresponding thickness of each film. Data is represented by the hollow blue circles and the solid blue circle represents a film that exhibits characteristic outlying from the other data. The broken blue line indicates the linear fit to the whole dataset whilst the solid blue line represents the linear fit to the data without the inclusion of the outlying point

---

been used to fit the trend line to the data. The fit line corresponds to a relationship between T_c in K and d in nm of $T_c = 13.6 - (52.3/d)$ for this recipe of NbN. Here, unlike with the results in the $Nb_{0.3}Si_{0.7}$ films, the inclusion of the apparent outlier has very little impact on the overall trend.

The relationship suggests T_{c0} is predicted to be 13.63 K for bulk films. Extrapolation of the relationship to 0 K provides a value of $d_c = 3.85$ nm to be the critical thickness. As with the $Nb_{0.3}Si_{0.7}$ films, this value of d_c is in excellent agreement ranges of ξ_{GL} reported for NbN in the literature [108, 109].

Yong *et al.* report a thickness-tuned SIT in NbN films between 1.3 nm and 1 nm for magnetron sputtered films [110], a third of the result we predict here. Since the SIT is dependent on the disorder within the material as fabricated it is believable that our samples are more disordered than those reported in the literature. This is supported by the fact that Yong *et al.* report T_c values of thicker films to be in the region of 15 K, a value higher than the value of T_{c0} attained here. In addition the

authors assert that an SIT is expected to occur where d is within the range of a few unit cell, reported at 0.44 nm for NbN [110]. Our estimate of d_c falls within such limits.

4.5 The Finkel'stein Model and Elastic Scattering Times as an Indicator of Disorder

A more advanced method of characterising disorder can be found by extending the Finkel'stein model introduced in Section 2.3 to our materials. The model describes the relationship between sheet resistance and the critical temperature in thin films which can also used to extract parameters of interest from data [6, 8]. The model is the completed work originally put forward by Maekawa and Fukuyama [74, 75]. They proposed corrections to the theory of dirty superconductors by Anderson, which looks at localisation and the interplay between Coulomb interactions and disorder. The corrections suggest that as disorder in a 2D system is increased so too is the repulsive Coulomb interaction, whilst the electron density of states in these systems is lowered. These effects combine to suppress long range phase ordering, lowering T_c and ultimately suppressing superconductivity.

The Finkel'stein model has since been used to describe experimental data in thin films of MoGe [6, 8], TiN [80], Nb [77] and various compositions of Nb_xSi_{1-x} [78, 79]. We consider the arrangement of the relationship, as shown in Equation 4.1 [77]. This was introduced in Equation 2.8 but is repeated here for the continuity of our analysis) .

$$\frac{T_c}{T_{c0}} = \exp^{\gamma} \times \left(\frac{\frac{1}{\gamma} - \sqrt{\frac{t}{2} + \frac{t}{4}}}{\frac{1}{\gamma} + \sqrt{\frac{t}{2} + \frac{t}{4}}} \right)^{\sqrt{1/2t}}, \tag{4.1}$$

where $t = R_{\square} \left(e^2/\pi h \right)$ and γ, a fitting parameter given as an indicator of disorder, is related to the elastic scattering time τ by Equation 4.2

$$\gamma = ln \left(\frac{h}{k_B T_{C_0} \tau} \right). \tag{4.2}$$

In this section we apply the Finkel'stein model to the data from our films as a second means of extracting values of T_{c0} for comparison to those predicted in the previous section. We also use the model to identify the γ parameter and consequently the corresponding value of the elastic scattering time. We then use these to estimate the mean free path and coherence lengths in the films to assess the degree and influence of disorder on the low temperature behaviour of these films.

4.5.1 Fitting the γ parameter for films of Nb_xSi_{1-x}

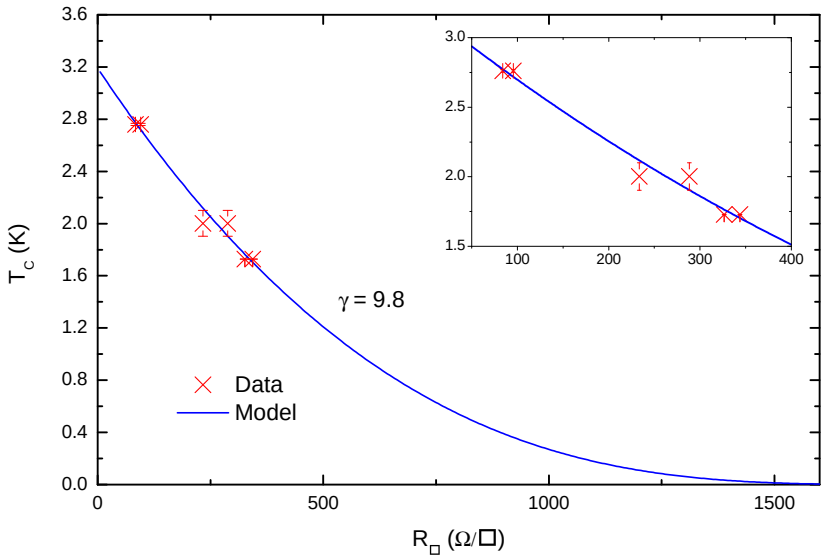

Figure 4.7: Comparison of the data from $Nb_{0.3}Si_{0.7}$ film samples to Finkel'stein's model for disordered superconducting thin films. Inset: The region around the data-points around the data at increased magnification.

From the $R(T)$ data in 4.1 we have extracted corresponding values for $R_\square$ and T_c for each of the film samples. The value of $R_\square$ was calculated using the normal state resistance here defined as the peak resistance of the sample preceding the superconducting transition. The data points are plotted against each other for $Nb_{0.3}Si_{0.7}$ films in Figure 4.7. We use a two parameter LMS method to fit the Finkel'stein model in Equation 4.1 to the data in order to extract the parameters

γ and T_{c0} for our materials.

Figure 4.7 shows the Finkel'stein fit to the data for the $Nb_{0.3}Si_{0.7}$ film set represented by red crosses. The fit to the data generated an adjusted R^2 value of 0.97 and is indicated by the solid blue line[5]. A γ value of 9.8 was generated alongside a value of $T_{c0} = 3.19 \pm 0.09\,\mathrm{K}$ predicted by the fit. This value of T_{c0} is in good agreement with that indicated by the T_c (1/d) trend for this film in Figure 4.5 of 3.25 K, a value that falls within the standard error of the Finkel'stein fit here.

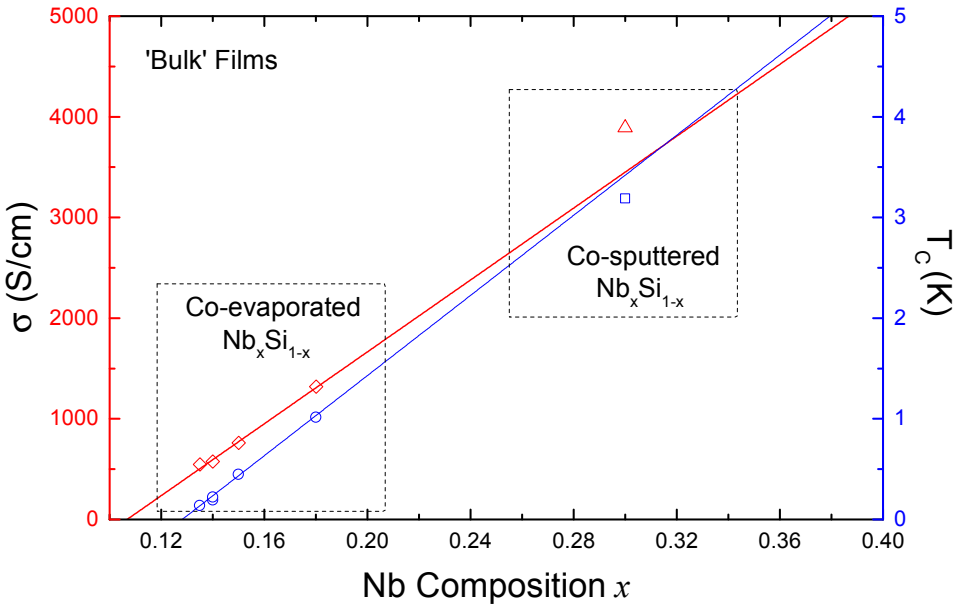

Figure 4.8: Plot comparing bulk values of normal state conductivity and T_c in films of $Nb_{0.3}Si_{0.7}$ against reported trends. The values for conductivity and T_c in co-evaporated films are represented by red diamonds and blue circles respectively. The same parameters extracted from our measurements in co-sputtered $Nb_{0.3}Si_{0.7}$ films are represented by the red triangle for conductivity and the blue square for T_c. The solid red and blue lines represent linear fits to the co-evaporated datapoints. All literature values corresponding to co-evaporated films were reproduced from studies by Crauste *et al.* [89].

To date, values of T_{c0} have not been previously reported for the $Nb_{0.3}Si_{0.7}$

[5]Although it could be argued that this data appears to also exhibit a linear dependence, the Finkel'stein model has been established as an accurate model in describing the relationship between T_c and $R_\square$ for thin superconducting films. For both materials, fits were generated to a tolerance of 1×10^{-9}.

composition in the literature. Figure 4.8 shows the a comparison of the the value of T_{c0} optained to those found for varying compositions by Crauste *et al.* [89]. Values were extracted using the DataThief software package, and indicate linear trends in T_{c0} and conductivity. The figure also shows the datapoints for the $Nb_{0.3}Si_{0.7}$ films studied here.

T_{c0} values of 0.59 K have also been reported for values of $x = 0.15$ [78] and T_{c0} =0.8 K for $x = 0.17$ compositions of Nb_xSi_{1-x} films. Both of these values are considerably lower than that observed here for what are higher Nb compositions. This deviation can clearly be seen in Figure 4.8. However, these values are reported for films deposited using electron beam evaporation which is known to produce smaller grain sizes than those achieved with magnetron sputtering due to the higher energy nature of the process. Van der Zant *et al.* have reported T_{c0} values of 3.9 K for co-sputtered Nb_xSi_{1-x} compositions where $x = 0.42$ [111] . This value is consistent with what we have observed from our data here as we would expect the T_{c0} to be suppressed slightly by the lower Nb composition.

4.5.2 Fitting the gamma γ parameter for films of NbN

Figure 4.9 shows the relationship between T_c and $R_\square$ for the NbN film samples. The red crosses represent the experimental data, whilst the solid line represents the corresponding fit to Finkel'stein's model with an adjusted R^2 coefficient of determination of 0.97 generated. We found the closest convergence to the data for values of $\gamma = 6.4 \pm 0.2$, corresponding to a T_{c0} of 13.54 ± 0.26 K. This value falls within the range reported for NbN [87, 112]. Only limited comparison can be made to films in the literature in the case of NbN, as compositional analysis has not been provided by these authors. Whilst lower than the maximum values reported in the literature, we attribute this to differences in fabrication and composition of these other films. In comparison to the value of T_{c0} predicted in Figure 4.6 the value we calculate through Finkel'stein's model is marginally lower than the 13.6 K found with the previous method but within the tolerance of the standard error found estimated by the model, providing a good agreement between methods.

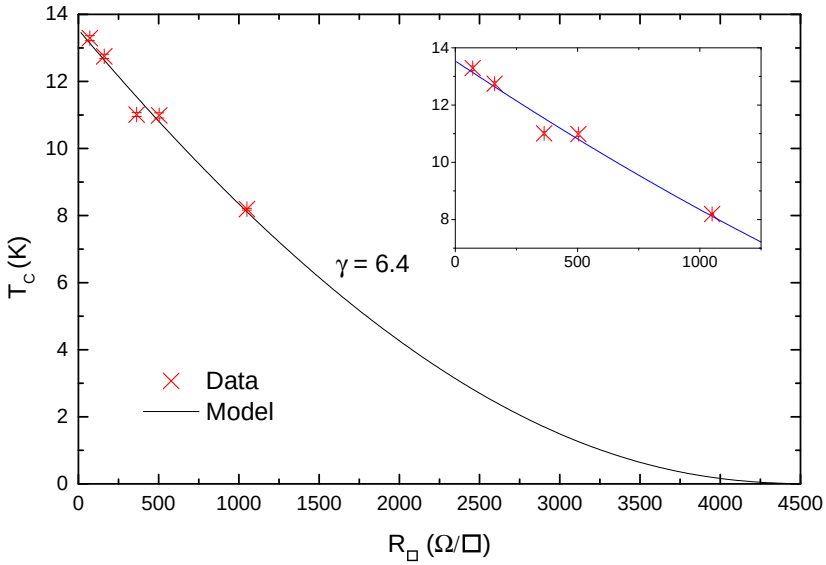

Figure 4.9: Comparison of the data from NbN thin film samples to Finkel'stein's model for disordered superconducting thin films. Inset: The region around the data-points around the data at increased magnification.

4.5.3 Calculation of the elastic scattering time τ and its use in the estimation of coherence length ξ in Nb_xSi_{1-x} and NbN films

Equation 4.2 may be rearranged to find the elastic scattering time τ in terms of γ and T_{c0}, such that

$$\tau = \left(\frac{h}{k_B T_{c_0} e^{\gamma}} \right). \tag{4.3}$$

The superconducting coherence length ξ_{GL} in these materials may subsequently be estimated using the approximation for the dirty limit[6] [77, 113, 67];

$$\xi_{GL} \approx 0.852\sqrt{\xi_0 l} \tag{4.4}$$

[6]In using this approximation, we follow the example of applications in the literature though we recognise that such action is in fact an estimate of $\xi_{GL}(0)$. Application in the literature is unclear on this point and authors appear to have ignored the temperature dependence of the full approximation to the dirty limit.

where ξ_0 is the BCS coherence length of the bulk material and l is the mean free path in the material given by $l = \nu_F \tau$. The coherence length of the bulk material is estimated using the corrected Pippard approximation $\xi_0 \approx (0.18\hbar\nu_F)/(k_B T_{c0})$, [89]. For our calculations we substitute in the values of T_{c0} we have found using the Finkel'stein model.

In this subsection we discuss the outcomes of our calculations a summary of which we present in Table 4.1.

	$Nb_{0.3}Si_{0.7}$	Literature	NbN	Literature
T_{c0} (K)	3.19 ± 0.09	0.2 - 2.5 [111, 107, 79]	13.54 ± 0.26	14.9 [112]
γ	9.8	–	6.4	–
τ (s) ($\times 10^{-16}$)	8.5	1 [78]	56.6	1 [112]
ν_F (m/s)	10^6	$10^5 - 10^6$ [107, 78]	10^5	$10^4 - 10^6$ [114, 112, 115]
l (nm)	0.85	0.27 [107]	0.57	0.1 - 0.6 [112, 115]
ξ_0 (µm)	0.43	5 - 12 [107]	0.01	0.007 ([116])
ξ_{GL} (nm)	16.29	2 - 58 [107, 78, 89]	2.05	3.5 - 8 [108, 109]

Table 4.1: Table showing parameters of interest in the calculation of the dirty-limit coherence length in Nb_xSi_{1-x} and NbN films. Calculations were made using T_{c0}, γ and τ values obtained from the application of Finkel'stein's model to the film data. Relevant values reported for similar films are included for comparison. The values of ν_F for our films have been estimated from those reported for similar compositions and films.

Scattering times τ in Nb_xSi_{1-x} and NbN films

The fit to the $Nb_{0.3}Si_{0.7}$ data identifies a γ parameter value of 9.8 to exhibit the greatest agreement. Using this and the value of T_{c0} we calculate the value of τ corresponding to the $Nb_{0.3}Si_{0.7}$ dataset to be 8.49×10^{-16}s. This value is close to the reference value of 10^{-16}s reported in the literature [78] and appears to indicate an accurate description of the data.

As discussed in Section 4.5.2 the Finkel'stein fit to the critical temperature and sheet resistance data for the NbN samples is shown in Figure 4.9 predicting bulk critical temperature of 13.54 ± 0.26 K. This value of T_{c0} alongside the γ fitting value of 6.4 generated, corresponds to a scattering time of 5.66×10^{-15} s. This value is within acceptable range of the value of 1×10^{-16} s estimated for films by

Ezaki *et al.* [112][7], as indicated in Table 4.1.

The mean free path l in Nb_xSi_{1-x} and NbN films

The mean free path within our films was calculated by substituting the resulting values of the relaxation time in the relation $l = \nu_F \tau$. The parameter ν_F is the value of the Fermi Velocity given by Equation 4.5

$$\nu_F = \frac{\hbar k_F}{m}, \tag{4.5}$$

where m is the effective mass and k_F is the Fermi wave vector, given by $k_F = (3\pi^2 n)^{1/3}$ according to the free electron model. In the latter relation, n represents the carrier density in the system. Field dependence behaviours were not investigated for our samples. As such, the exact carrier densities and corresponding values of the Fermi wave vector k_F and the Fermi velocity ν_F are unconfirmed for these films. Calculations were made using values of ν_F reported in the literature for similar materials, as listed in Table 4.1. These are of the order of $10^5 - 10^6$ m/s for Nb_xSi_{1-x} films and 10^6 m/s for NbN.

The results in the table for values of the mean free path estimations in $Nb_{0.3}Si_{0.7}$. The same calculation as applied to the scattering time for this material generates a value of 0.85 nm. This is relatively close to the value reported in the literature of 0.27 nm. The mean free path is often quoted to be equivalent to the interatomic spacing in the film which should be of the order of several Angstroms. As can be seen our result is within tolerance of this range and what has been previously reported in these materials [107].

For NbN films, the mean free path l has been reported to be within the range of $0.1 - 0.6$ nm [112, 115]. Comparing this range with the value calculated for our films, our results appear in good agreement with the literature. A value of 0.57 nm was calculated using the extracted value of scattering time and the cited value for the Fermi Velocity listed in Table 4.1.

[7]The value of ν_F for [112] was estimated 8×10^5 m/s using $n = 10^{28}\, m^{-3}$ reported in this paper and $\nu_F = (\hbar/m_0)[(3\pi^2)n_e]^{1/3}$

Estimation of the coherence lengths in films of Nb_xSi_{1-x} and NbN

As discussed earlier in this section, Equation 4.4 may be used to estimate the Ginzburg Landau coherence length within the dirty limit. We first use $\xi_0 \approx (0.18\hbar\nu_F)/(k_B T_{c0})$ [89] to approximate the BCS coherence length for the bulk film. The value of ξ_0 found for our $Nb_{0.3}Si_{0.7}$ films is 0.43 µm. This is an order of magnitude smaller than what has been reported in the literature, but still consistent with what we might expect to see. As discussed in Section 4.5.1 and stated in Table 4.1, the literature values cited for Nb_xSi_{1-x} films pertain to films exhibiting lower T_{c0}. Since $\xi_0 \propto T_{c0}^{-1}$ we can expect to see smaller values of ξ_0 in our films. Subsequently, in Table 4.1, we estimate the resulting dirty limit coherence length ξ_{GL} for the $Nb_{0.3}Si_{0.7}$ film set to be 16.3 nm. This value falls well within the reported range of 2-58 nm for Nb_xSi_{1-x} suggesting that Finkel'stein model provides a good description of the behaviour of these films.

For the NbN films, we have estimated the coherence length ξ_0 in the bulk material to be 10 nm, a value in close agreement to 7 nm measured by Semenov *et al.* [116]. The corresponding dirty limit estimate for the coherence length is found to be ~ 2.1 nm using the mean free path calculated from the Finkel'stein Model. This is again within acceptable range of what has been reported in the literature for the Ginzburg Landau coherence length in the dirty limit.

4.6 Conclusion

In this chapter we have grown Nb_xSi_{1-x} films on Si and Al_2O_3 substrates via co-deposition using magnetron sputtering Physical Vapour Deposition. We present the low temperature characteristics of $Nb_{0.3}Si_{0.7}$ films, a composition of Nb_xSi_{1-x} previously unreported in the literature. Incorporation of Si was shown to produce an expected reduction in the superconducting critical temperature for films of $Nb_{0.3}Si_{0.7}$ when compared to pure films of Nb.

Our films exhibit values of T_c that are higher than what might be expected from values reported in the literature. We propose that, aside from composition,

differences in fabrication will be the determining factor as reported critical temperatures in our films have been typically higher than what could be projected in comparison to lower compositions of Nb_xSi_{1-x} fabricated using electron-beam co-evaporation. We also believe that such variations in T_c indicate that there is still further scope for work in understanding the impact of fabrication methods on the characteristics of thin superconducting films, in particular grain size and order if any, and their impact on film behaviour at low temperature.

We have also grown thin films of NbN using magnetron sputtering co-deposition in accordance with a recipe proposed by Glowacka *et al.* [88] which was then adapted to our own equipment. A range of films of different thicknesses were fabricated and characterised at low temperatures. Critical temperatures larger than 13 K were demonstrated, within range of those reported in the literature for comparable films.

The evolution of T_c with film thickness was studied for all films and an inverse dependence was demonstrated in our films. This was used to predict the bulk film critical temperatures T_{c0} for both films with values of 3.25 K and 13.6 K predicted for $Nb_{0.3}Si_{0.7}$ and NbN materials respectively. In addition, the relationship between T_c and d for these films was used to predict the characteristic critical thickness d_c at which we expect to observe an SIT. This was found to be approximately 3.8 nm for $Nb_{0.3}Si_{0.7}$ and 3.9 nm for NbN. We discussed the significance of this lengthscale as an estimator of ξ_{GL} in our films. The values of d_c we have found for our films fit perfectly within the ranges of ξ_{GL} in the literature, as we report in Table 4.1.

A further relationship between T_c and $R_\square$ has been investigated. This was shown to be in agreement with the model put forward by Finkel'stein describing the impact of disorder in thin superconducting films as thickness is reduced. We have analysed the data through the use of the Finkel'stein model and have provided sensible estimates of T_{c0} for both our materials. To our knowledge, this is the first successful application of this model to the behaviour of NbN and $Nb_{0.3}Si_{0.7}$ films. Analysis of the γ term has been used to estimate elastic scattering times

for the two materials. Subsequent calculation of the BCS and Ginzburg-Landau coherence lengths for our films showed a good agreement to the ranges reported in the literature, demonstrating that the Finkel'stein model can be used to accurately describe the behaviour of our materials.

Chapter 5

Hybrid Stencil Etching - A Repeatable Nanowire Fabrication Technique

5.1 Introduction

This chapter is one of two alongside Chapter 6 describing the fabrication and characterisation of our nanowire samples. The two chapters were originally a single chapter but were split to provide greater clarity.

In this chapter we discuss the innovative ways in which other groups have overcome the challenge of nanowire fabrication, ranging from traditional lithographic techniques to the more innovative. We discuss the strengths and weaknesses of existing lithographic techniques and the practicality of their use. We consider the challenges faced in fabrication of nanowires and present the development of our own fabrication technique for the reduction of superconducting thin films to nanowire dimensions.

5.2 Nanowire Fabrication Methods State of the Art

The investigation of the QPS phenomenon has demanded the use of increasingly innovative techniques to fabricate finer wires. Early in the field, the minimum device

widths achievable using nanolithography led many groups to develop techniques that stepped away from conventional nanolithography and employ other methods in order to overcome the limitations on minimum widths of lithographic fabrication. One of the earlier examples of such a technique was that of Giordano and his work in investigation of In nanowires. He utilised a step-edge lithographic technique to create the wires [45], proposing two variations of this technique, both illustrated in Figure 5.1.

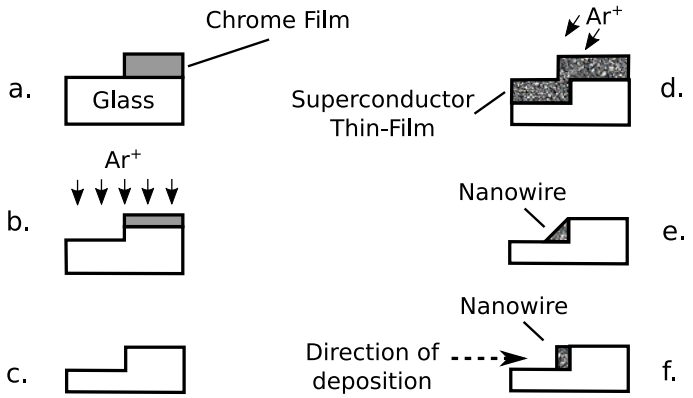

Figure 5.1: Step edge fabrication procedure used by Giordano *et al.* for creating fine metal wires. Adapted from [117].

For both processes, steps **a.-c.** are identical. A chrome masking layer is evaporated across half a glass substrate, as seen in Figure 5.1 **a.**. The substrate is etched (**b.**) using Ar ions to produce a square step and the chrome layer is subsequently removed using a chemical etch (**c.**). At this point the author describes two possible avenues which may be taken. In the first, the step is coated with a film of the desired superconductor **d.** prior to further etching with Ar ion at an angle to the step. The result **e.** is a wedge shaped nanowire formed in the shadow of the step in the slide. For the second method, a superconducting film is deposited onto the step at an angle parallel to the substrate **f.**. This process results in a the deposition of a film along the step edge. A subsequent milling stage may be required to remove any light coating that may have been deposited on the rest of

the substrate. The result is a nanowire formed along the edge of the step.

Giordano reports that both these processes can be used to produce nanowires of down to 30 nm in width and up to 0.5 mm in length, that are uniform both along the length of the wires and in terms of cross section. The author predicts that each process can be used to fabricate wires as small as 10 nm in cross-sectional dimensions. However, the limiting factor stated is that of the edge roughness of the chrome layer, which exhibits a grain roughness of 10-20 nm, as this is transferred to the step edge and consequently the wire itself. Finer-grain masking films of NiCr are suggested as an alternative.

Bezryadin *et al.* [13, 118] describe a method for fabricating nanowires in which they use nanotubes as scaffolds. In their method they grow an oxide and subsequent nitride layer on a silicon substrate. A 100 nm wide slit is patterned into the SiN layer using electron-beam lithography and reactive ion etching and the SiO_2 area beneath the slit undercut using a hydrofluoric acid etch. Carbon nanotubes are then deposited across the slit and the entire sample covered in a 5 nm thick layer of amorphous superconducting film followed by a protective Ge or Si film of 1-2 nm thickness. Finally, a suitable single nanowire is identified using scanning electron microscopy and electrodes are patterned into the superconductor layer using optical lithography and RIE, to provide connections to the nanowire.

Figure 5.2 shows an example of **a.** a 4 nm thick nanowire deposited onto a 2 nm thick carbon nanotube scaffold and **b.** a TEM image of a narrower CNT scaffold wire with a protective Si coating visible as the lighter layer around the wire. The technique was particularly attractive for the investigation of QPS in superconducting nanowires as it produced nanowires well within the 10 nm width range suggested by Zaikin *et al.* [50], for the observation of QPS phenomena. Bezryadin *et al.* report wire thicknesses down to 5.5 nm ($\pm$1 nm), and lengths of 95-185 nm.

For measurements in [12] Zgirski *et al.* utilise Ar ion milling to downsize Al nanowires to dimensions of down to 8 nm in cross-section. The method is described

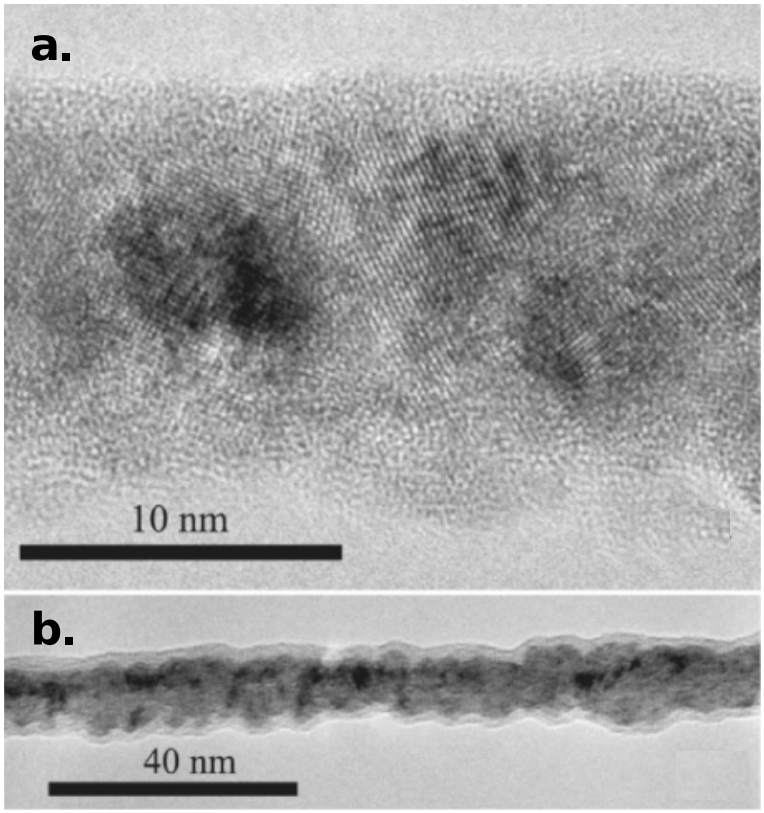

Figure 5.2: TEM images of **a.** A Nb nanowire 4 nm thick deposited onto a 2 nm diameter carbon nanotube scaffold and **b.** a second nanowire coated in a protective Si layer. Image adapted from Rogachev *et al.* [118].

in greater detail in [119]. A low energy Ar broad ion beam at an angle of 40° to the substrate can be used to gently erode the surface of structures such as nanowires, reducing their dimensions and smoothing surface geometry. The method allows for controlled reduction of the wire cross section with an accuracy of 1 nm and, as such, serves as a useful tool in observing the effects of reduced dimensions in the behaviour of nanostructures, as demonstrated by the results of Zgirski and Arutyunov's study in [12].

Finally, Myung-Ho *et al.* [55] built on the scaffold principal presented originally by Bezryadin *et al.* introduced earlier. Their technique once again uses a slit formed by patterning and etching a layer of SiN. A trench is then etched into the SiO_2 sub-layer using hydrofluoric acid. Adhesive tape is then applied across the trench and removed leaving polymer nanostrings suspended across the gap. Amorphous MoGe or Al is sputtered onto the nanostrings to form nanowires. A suitably sized wire is then selected using SEM and thin film electrodes are formed in the metal layer. All other nanowires are severed, leaving only one connected to the electrodes. The authors reported wires of down to 12 nm in thickness, although this thickness is reportedly proportional to the width of the trench.

5.3 Challenges in Lithographic Fabrication

In parallel to the development of these novel techniques, EBL-based nanolithography has also been refined. The two primary methods of device fabrication using EBL nanolithography are illustrated in Figures 5.3 **a.** and **b.**. For lift-off, illustrated in **a.**, a resist layer is applied to the substrate first, into which the nanowire pattern is exposed. After development, a superconducting thin film is applied onto the sample and then the remaining resist and unwanted film lifted off in solvent to leave the nanowire structure.

Where a conventional lift-off fabrication technique is used, wire features as narrow as 50 nm have been reported for ZEP resist [120], and 25 nm (whilst maintaining geometric uniformity) in PMMA [121]. However these techniques

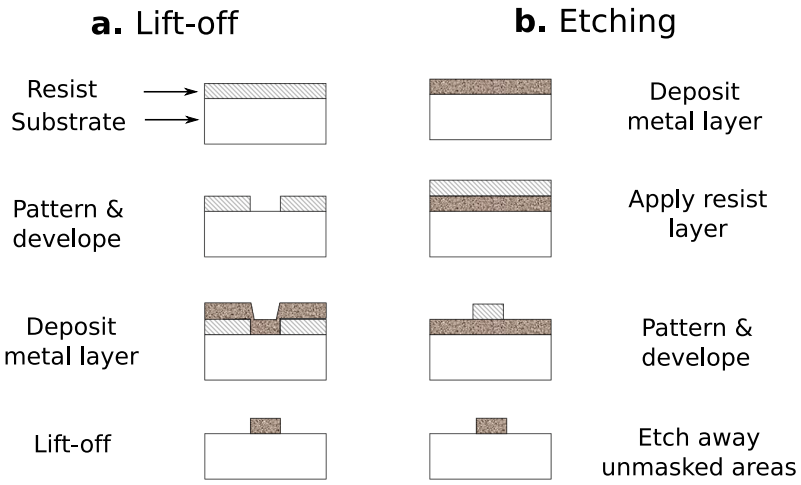

Figure 5.3: Illustration of **a.** lift-off and **b.** etching based fabrication techniques.

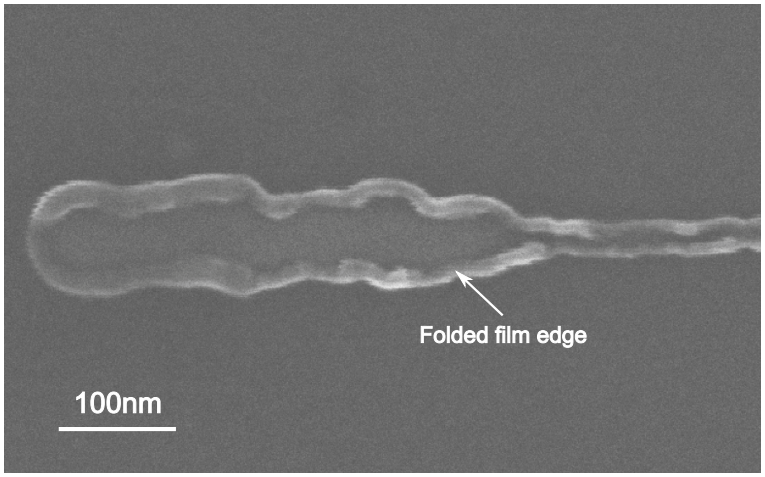

Figure 5.4: SEM image of 'lily pad' folded edge structures resulting from a non-ideal lift-off process. Image courtesy of Dr J Fenton, UCL, 2014.

are heavily limited by the minimum width of the exposure, which in turn can be affected by the capabilities of the EBL system along with factors such as the process temperature, chamber pressure, resist age and substrate material. In addition, fabrication features such as lily-padding may occur which introduce geometric ambiguities with respect to the nanowire structure, as illustrated in Figure 5.4.

Etch-based negative-tone resist techniques offer one solution to this problem. A typical etch based process is illustrated in Figure 5.3 **b.**. As with positive resist, electron beam lithography is used to directly write the nanowire pattern into the negative resist. However, unlike positive-tone resists and lift off, the negative resist is used as a protective mask to transfer the exposed pattern into the superconducting film. Thus, within some tolerance, any over etching will only result in narrower nanowires. Whilst PMMA can also be used as a negative tone resist at higher exposure energies, HSQ has become a popular alternative, forming an etch resistant silicide when exposed. Features of sub-10 nm [122] have been reported in resist only studies with features of 20 nm width reported for studies investigating superconducting nanowires [123, 59].

The primary limitation in the use of HSQ is in its removal after the process. Unlike polymer-based resists, the resulting silicide that defines HSQ as an attractive etch mask is difficult to remove without the use of RIE. A further complication that could be considered in the use of negative resists as etching masks is that the process risks crystallisation of the superconducting film below the resist, during exposure [124]. Such beam induced changes to the structure of the material are undesirable from the perspective of experimental accuracy in materials characterisation as they add uncertainty to investigations. However, the minimum dose required for this to occur according to Remeika *et al.* is $50\,\mathrm{pC\,nm^{-2}}$. This value is significantly higher than the minimum exposure dose of HSQ of $5 \times 10^{-6}\,\mathrm{pC\,nm^{-2}}$ used within our facility.

5.4 Development of the stencilling method

In order to overcome these fabrication challenges during our investigations, we developed our own process for fabricating nanowires from superconducting thin films using EBL. We elected to develop a technique that merged the benefits of ease in fabrication found with positive tone exposures with the favourable feature sizes that can be achieved using negative resists in etch based processes. In this section we discuss the reasoning and development stages that led to the creation of the EBL stencilling fabrication process.

5.4.1 The principle behind EBL stencilling

The fundamental idea behind our process is the use of a stencil based etching approach to fabrication. Figure 5.5 illustrates the simplified process steps. Similar to negative resist processes, we deposit a thin superconductor layer onto a substrate. PMMA 950 A2 is then applied to a depth of 100 nm as a protective layer.

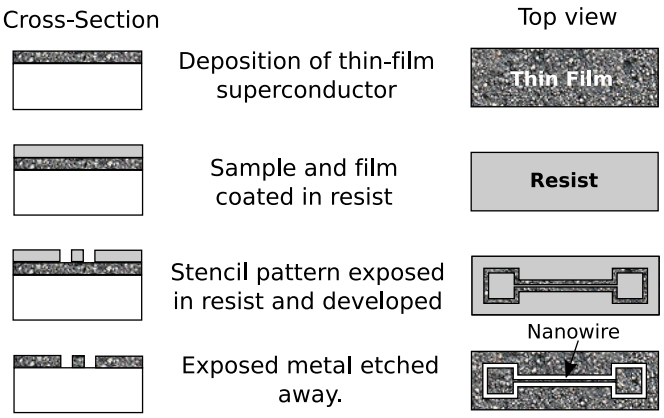

Figure 5.5: Illustration of the stages of stencil fabrication for nanowires. A thin film is deposited onto a substrate and coated in a protective layer of PMMA resist. A stencil pattern is then used to define the edges of the nanowire device in the resist. Following development, the pattern is etched using ion etching techniques to electrically isolate the nanowire from the bulk film.

At this stage the process diverges from standard techniques. We do not write the nanowire pattern into the resist. Instead we use the electron beam to draw a

stencil pattern that defines the nanowire device edges. The resist is developed and the sample is subsequently etched. The etch step transfers the pattern into the thin film layer and electrically isolating a region of film that forms the nanowire device. This is further illustrated in Figure 5.7.

5.4.2 Benefits of the stencilling technique in nanowire fabrication

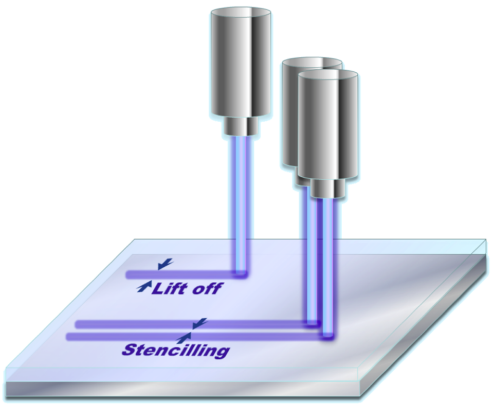

Figure 5.6: Exposure of a substrate in stencil fabrication. The illustration shows the minimum feature benefit of a EBL stencilling over standard exposure and lift off. The minimum features of an exposure are no longer determined by the exposure width.

The use of stencilling results in several benefits over conventional lithographic techniques. Most critically, such a process side steps the limitations of standard techniques that are associated with beam exposure widths. Figure 5.6 illustrates the feature width benefits of stencilling over standard lift-off technique. By defining the edges of the nanowire instead of the nanowire itself, the minimum feature width is no longer determined by the exposure width but instead by how close together the two exposure paths can be positioned. The etch-based nature of the process also simplifies the latter point. Although the stage control in most modern EBL systems is capable of nanometer precision, wider patterns will inherently be narrowed by both proximity exposure and a longer subsequent etch step. This will still occur with our process, but it allows for patterns to be tuned to compensate

for this effect. Thus two phenomena of fabrication that were originally limiting or risk factors, proximity exposure of resist and over etching, can be harnessed to achieve desireable results in our process, as illustrated in Figure 5.7.

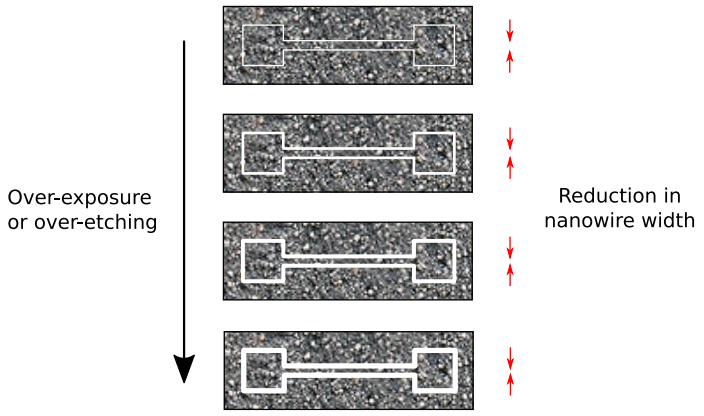

Figure 5.7: Etching of a substrate in stencil fabrication. The illustration shows that over-etching and proximity exposure effects can be tuned to improve minimum feature width for EBL stencilling.

In addition to the feature benefits, any risk of material crystallisation is minimised as the area of superconductor that forms the nanowire is not exposed to energy from the electron beam as it is in a negative resist based processes. Furthermore, since the process is the etch-based as opposed to lift-off, the problem of 'lily-pad' edge folds is also eliminated.

Finally, and possibly the significant argument in favour of using an etch based technique, is the fact that the superconductor thin film is uniformly deposited onto the entire substrate. This serves to reduce stress in the final wire structure.

5.4.3 Full mask EBL exposure

There were two main iterations of the stencilling process, a full-mask process and a subsequent hybrid process. Initially, efforts were focussed on a full mask EBL exposure process in which both the macro-scale connection pads and the fine features of the nanowire were exposed entirely using EBL stencilling.

Pattern design features

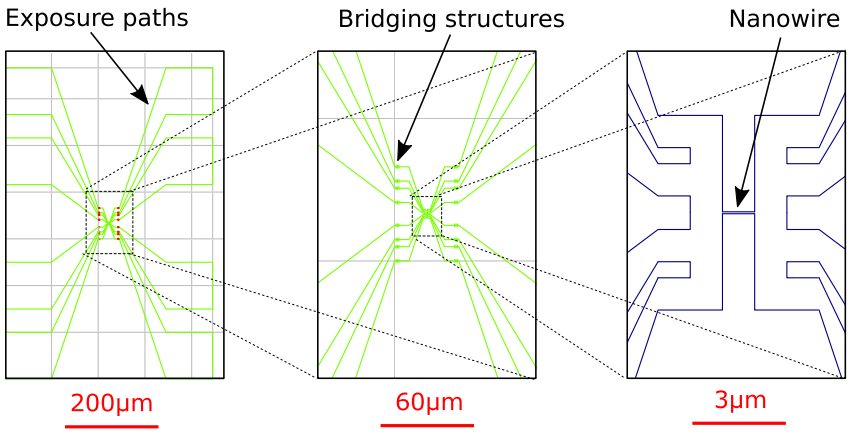

Figure 5.8: The full mask EBL stencil. The figure shows the EBL pattern used to expose the wire and its connection pads, at increasing magnification. The macro-scale exposure path is indicated by the green line whilst a finer feature exposure is indicated by the blue lines at higher magnification. The dashed lines indicate the 100µm ×100µm EBL write-fields into which the pattern is fractured.

Figure 5.8 shows the nanowire design developed for this process illustrated at increasing magnification. The design comprises a nanowire structure formed of eight 100 µm ×100 µm connection pads leading into a nanowire region in the centre.

In order to optimise exposure times, the structure was split into two exposures. The first was a larger aperture exposure for coarser features, shown by the green paths in Figure 5.8. The second, finer aperture exposure was used to define the finer region surrounding the nanowire, indicated by the blue paths in Figure 5.8.

The split nature of the exposure necessitated the inclusion of bridging structures, as indicated in the pattern. These brush-like structures allow an overlay tolerance of ±1 µm in each lateral direction of motion for the beam stage.

Limitations found in implementation

Although successful in defining very narrow regions for nanowires, limitations were found in use of the full-mask process. The two most significant of these were

the low throughput and the EBL write-field capabilities. In terms of throughput, although the double exposure did reduce the over all time required for exposure from that of a single fine aperture, the time taken to expose and develop a single wire pattern in practice was close to seven hours. The timescale coupled with the yield from the subsequent etch process resulted in a very low throughput of devices for this method.

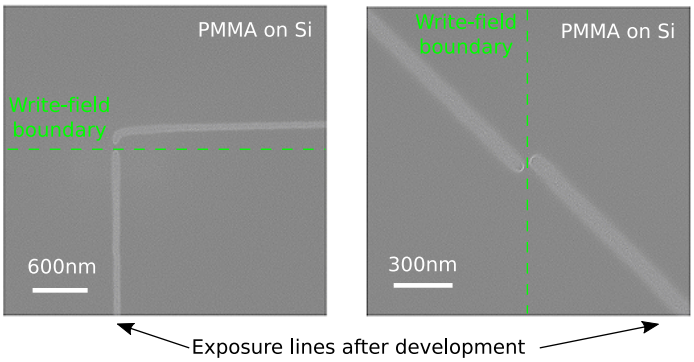

Figure 5.9: SEM images showing examples of discontinuities in the exposure of the nanowire pattern by the EBL. The images show exposed and developed EBL pattern paths in PMMA before any etching. The discontinuities in the exposure were regularly observed features for this iteration of the fabrication process, and resulted in electrical continuity between regions of the nanowire and the bulk film.

Whilst low throughput was a concern, a more fundamental limitation became clear during successive implementations of the process. We observed a limit to the write-field alignment capabilities of the EBL system. Illustrated in Figure 5.9 **a.** and **b.**, we found that, even where the system indicated a perfect alignment between the EBL exposure write-fields, the movement of the stage led to persistent stitching errors in the exposure line at the boundaries of individual write-fields.

The significance of such a process feature to our method was that each break in exposure ultimately represents a bridge in the mask between the nanowire structure and other regions of the film. As such, these discontinuities served as conductive paths to the bulk film on our samples. The feature was found to be particularly

inherent to beam-width exposures. We attempted to widen the exposure paths using a raster pattern in order to induce enough proximity exposure to eliminate this feature. However, the overall pattern spans a large number of write fields and it became impractical to ensure the elimination of these exposure discontinuities from the entire pattern.

5.4.4 The hybrid technique

Given the limitations of the full-mask process, we redeveloped our technique to incorporate a photolithographic step. In this updated process, we would define large scale macroscopic connection pads into the superconductor film using a photomask. This was to leave only the fine detailing involved in the definition of the nanowire for definition by EBL stencilling.

In this section we provide an overview of the design and development considerations of the hybrid stencilling method, discuss the benefits offered over the full EBL exposure method and present some examples of nanowires we have fabricated using this method.

The photomask pattern

Figures 5.10 **a.**- **c.** show the pattern developed and used for the photolithography process step. The mask was developed for use in a positive tone photolithography process step between film deposition and EBL patterning. After film deposition the sample was coated in S1805 photoresist and the macro-scale features defined in the resist layer using photolithography. On development, the solid region retains a resist mask whilst the remaining film is etched away using RIE, leaving pattern structures fabricated from the superconducting film. Each substrate die, illustrated in Figure **a.** is formed of four nanowire 'cores', shown in closer detail in figure **b.**. Each core comprises ten connection pads and lines connecting to a central region of material available to be customised in the subsequent EBL step. The central regions, shown in Figure **c.** measure within the field of a single write-field to avoid any risk of discontinuities in the pattern due write-field boundaries. The

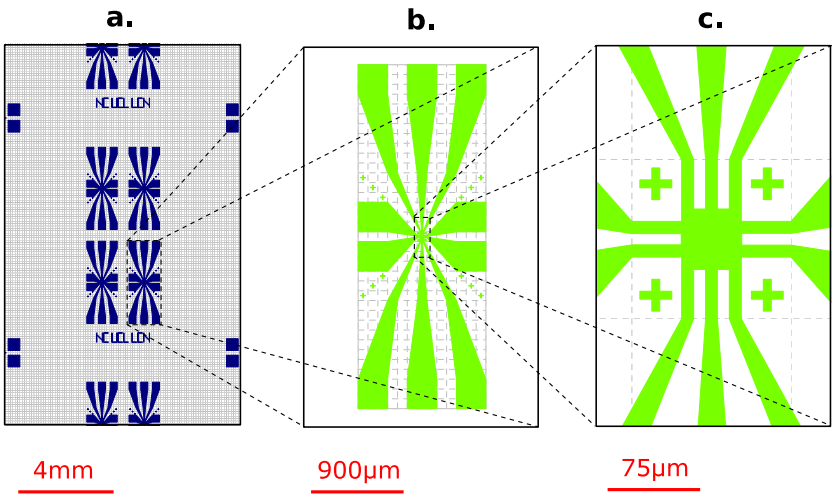

Figure 5.10: Pattern design for the photolithographic stage of the hybrid stencilling technique. **a.** shows a 10 mm×10 mm die on the photomask comprising four nanowire 'cores'. **b.** individual core, comprising ten connection pads leading into a single customisable region of material, shown in **c.**.

---

cross features in the pattern are EBL alignment features allowing the EBL to automatically recognise its position over the pattern and accurately position the EBL pattern over the existing photolithographic pattern.

Overlay and the EBL pattern

Following etching of the photolithographically defined features, substrates are coated in PMMA 950 A2 in preparation for the EBL exposure of the nanowire region. Figure 5.11 **a.** shows the complete EBL pattern for a single core of material. The exposure path is indicated by the blue feature lines in the figure. Figure **b.** show how this pattern overlays onto the centre of the core structure fabricated using photolithography and ion etching. Each central region is patterned into two nanowire devices with dedicated lines for current and voltage measurement. The length of the nanowire is defined as the separation between the two voltage tracks, set at 1µm for this design. The two unconnected leads are used to ensure that the etch step has successfully isolated the nanowire and its leads from the bulk film. Figure **c.** shows how the paths defining a single nanowire of design width 30 nm at

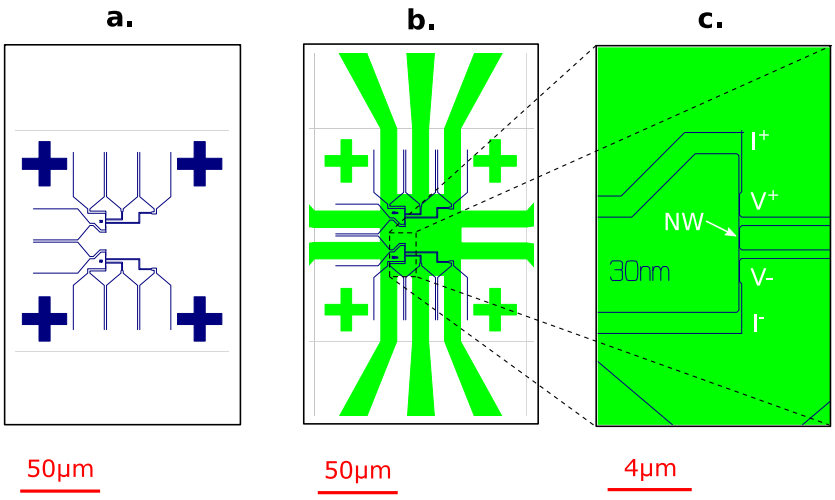

Figure 5.11: Pattern design and overlay for the EBL stage of the hybrid stencilling technique. **a.** the full EBL pattern for a single central region of material and **b.** its overlay onto one of the regions. **c.** shows a single nanowire pattern at higher magnification. The green region indicates the superconductor film whilst the blue lines define exposure paths in the pattern that will electrically isolate the nanowire and its connections from the bulk film.

---

closer magnification. The blue exposure paths define tracks in the customisable central region that, when etched using RIE, electrically isolate the nanowire and tracks to the connection pads.

5.5 Results of the Hybrid Stencilling Technique

In practice, our hybrid process proved to be very reliable for the fabrication of nanowires from superconducting thin films. The main benefits of the process are that the photomask eliminated the issues of write field exposure discontinuities whilst simultaneously allowing a much higher device throughput.

The use of the photomask increased the potential yield of each chip from a single nanowire to eight devices across the four cores, and allowed for substrates to be prepared in advance in batches, greatly reducing the fabrication time required.

In addition, by defining the connections pads and larger features using photolithography, the exposure time for the EBL stage was greatly reduced, with the

time for alignment and exposure of an eight wire device chip taking one hour. Furthermore, the multiple device nature of each chip and the greatly simplified EBL pattern allowed for the dimensions device to be customised. Using this feature, we were able to fabricated devices with a range of nanowire design widths allowing investigation of dimensional effects in wires of the same film.

Figures 5.12 **a.** and **b.** show examples of nanowires made using the stencil method from Nb_xSi_{1-x} and NbN thin films. Nanowires in the range 750 nm to 14 nm were fabricated from 30 nm thick films of $Nb_{0.3}Si_{0.7}$, and in the range of 500 nm to 20 nm were fabricated from 10 nm thick films of NbN. The etched EBL paths are visible in both images with the connections tracks leading into the nanowire regions. Inset in **b.** is an example of a nanowire at higher resolution. The path is clearly defined with the strength of the stencilling process demonstrated by the geometric uniformity across the length of the wire.

Widths of 14 nm and 20 nm respectively for $Nb_{0.3}Si_{0.7}$ and NbN films were the lowest achieved with this process across the attempts made. The primary factors influencing these limits were found to be in the selection of design widths for the EBL pattern and in the granularity of the materials used for the films. Particularly in the case of the wire design widths, as the lower limit is approached we found poorer correlation between the intended widths and the and the width of the fabricated nanowires. We strongly believe that further understanding of the relationship between the design width and the final width as the sub-20 nm range is approached along with a reduction in grain size of the films through fine-tuning of the sputter powers would yield narrower nanowires using this process.

5.6 Summary

In this chapter, we have discussed the novel ways in which other groups have approached the challenge of nanowire fabrication, alongside standard lithographic techniques. We have considered the limitations of standard techniques and the challenges face when fabricating nanowires using etching or lift-off based fabrication

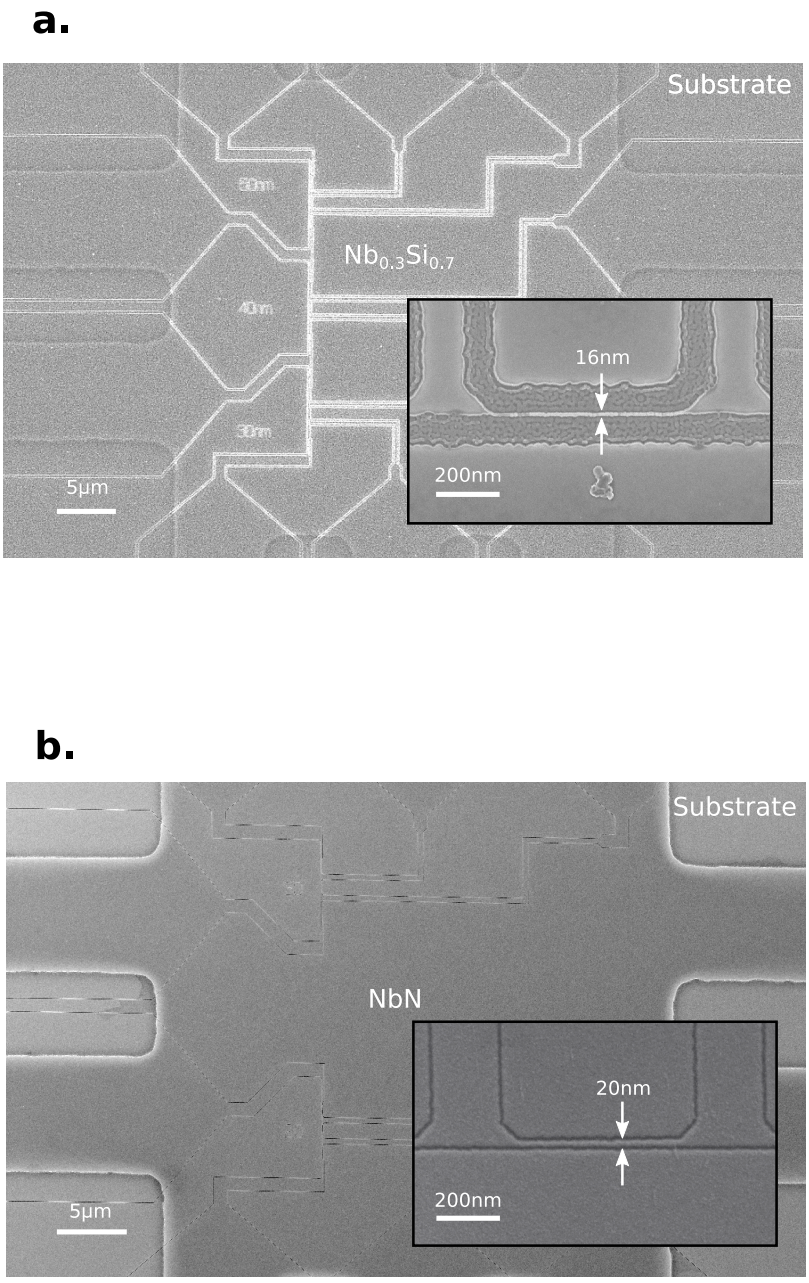

Figure 5.12: SEM images of nanowire device regions in **a.** Nb_xSi_{1-x} and **b.** NbN materials. The EBL exposed paths show clearly as contrast lines over the material region. Inset: Corresponding $Nb_{0.3}Si_{0.7}$ and NbN nanowires at high magnification.

techniques.

We subsequently presented the development of our own repeatable and reliable nanowire fabrication process and shown examples of the results that can be achieved through its use. We have shown how our EBL stencil etching process can be used to overcome the wire-width limitations set by factors such as the beam exposure width and proximity exposures and geometric deformities such as 'lily-pad' folded edges common to lift off techniques. Our process not only overcomes these issues but turns them to the user's advantage. We have shown that it is capable of producing long nanowires below the 20 nm literature average reported for lithographic techniques.

In the next chapter, we present low temperature measurements on a range of nanowires in Nb_xSi_{1-x} and NbN. All the nanowire samples were successfully fabricated using the EBL stencil etch fabrication process we have presented here.

Chapter 6

Disordered Superconducting Nanowires

6.1 Introduction

Following on from our introduction of the hybrid stencil method in Chapter 5, this chapter forms the second part of our work describing the fabrication and characterisation of nanowires from superconducting thin-films.

In Chapter 2 we have shown how models of disorder relate the Ginzburg-Landau coherence length for thin-films and extracted estimates for parameters of interest in our films using these models. In this chapter we look at scaling down the dimension of our films further to create nanowire structures. As discussed in Chapter 1, amorphous materials are desirable for the purposes of weakening the superconducting state and increasing the rate of quantum phase slips [5]. However, controlling the distribution of disorder in these films in order to maintain homogeneous behaviour across them is not trivial. This becomes particularly apparent when patterning these films into nanowires. Even geometrically identical nanowires fabricated from films made in a single deposition tend to exhibit slight variations in behaviour.

We begin by looking at the temperature dependence of resistance in nanowires

of 1 μm in length fabricated from $Nb_{0.3}Si_{0.7}$ and NbN films identical to those investigated in Chapter 4. We discuss the dependence of the superconducting transition on wire widths as dimensions are reduced. Finally, we present a study on the impact of RF filtering on low temperature measurements in nanowire structures and how it can affect superconductivity.

6.2 Temperature Dependence of Resistance in Nb_xSi_{1-x} Nanowires

Nanowires were fabricated from thin films of Nb_xSi_{1-x} and NbN using a combination of photolithography, e-beam lithography and dry etching techniques as detailed in Chapter 3. After reduction to nanowire dimensions, samples were measured initially at 4.2K in liquid ^{4}He, to confirm connectivity. Following confirmation, they were then transferred to the PPMS ^{3}He probe for electrical characterisation at temperatures down to the millikelvin range. For the study on the impact of RF filtering, a dilution refrigerator was used to achieve lower temperatures.

6.2.1 Temperature dependence of $Nb_{0.3}Si_{0.7}$ nanowires & the impact of filtering on measurements

Non-filtered measurements down to 400mK

Four-point measurements were made on nanowires to investigate $I-V$ characteristics at low temperatures and the direct dependence of the wire resistance on temperature. Measurements were performed on the Quantum Design Physical Properties Measurements System using the QD ^{3}He probe insert.

Figure 6.1 shows the dependence of device resistance versus temperature for $Nb_{0.3}Si_{0.7}$ nanowires in a range of wire widths. All wires were fabricated from films of nominally 30 nm in thickness d. The thickness was confirmed using a Dektak step profilometer whilst the nanowire widths were confirmed using an SEM. The wires exhibit a superconducting transition from approximately $T = 3$ K. As the nanowire widths are reduced, broadened transition characteristics are observed. This broadening of the superconducting transition, proportional to the nanowire

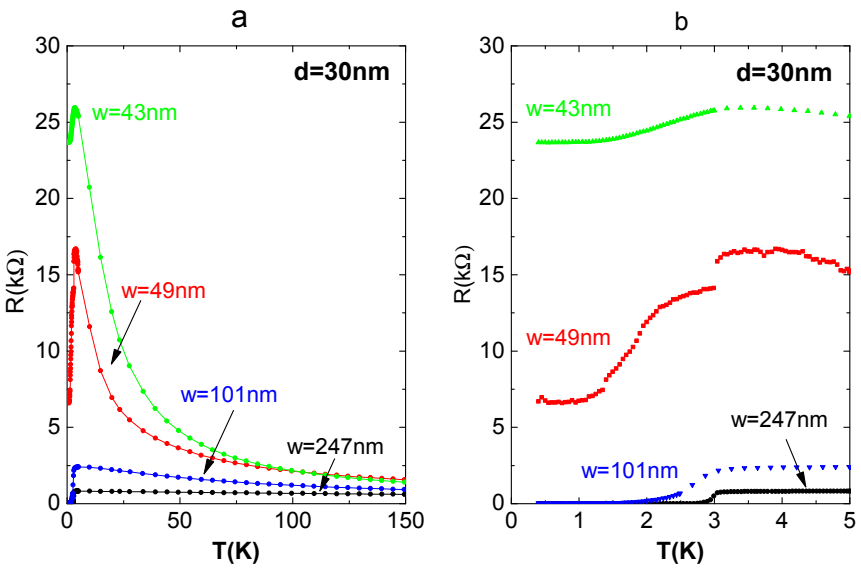

Figure 6.1: Unfiltered measurements to 400 mK of the temperature dependence of $Nb_{0.3}Si_{0.7}$ nanowires. Nanowires with widths w=247 nm, 101 nm, 49 nm and 43 nm, and film thickness d=30nm are presented.

---

width has been noted in previous works [13].

Of particular interest is the unexplained residual resistance below T_c observed for wires of widths narrower than 100nm. Whilst the resistance of the wider samples drops to zero below T_c, the resistance reaches plateaus of 6.6 kΩ and 23.7 kΩ respectively for the 49 nm and 43 nm samples. The origin of these residual resistance plateaus are clarified in Section 6.5.

As widths are reduced, an increasingly insulating characteristic is seen to emerge. Interestingly, the two phenomena appear related as the transition itself appears broadened in the presence of this increasingly insulating behaviour. The insulating trend as width is reduced would suggest that the samples are nearing the dimensions where a full transition to an insulating phase, or SIT, could be expected.

6.3 Low Temperature Characteristics of NbN Nanowires

Superconducting nanowires of NbN were fabricated from thin films of thickness $d \leq 10\,\text{nm}$, using the same fabrication process as for the Nb_xSi_{1-x} nanowires discussed in Section 6.2. The NbN nanowires had a considerably higher T_c than their Nb_xSi_{1-x} counterparts. This allowed for characterisation of their superconducting state at much higher temperatures. Measurements of NbN nanowires were performed at 4.2K in a ^{4}He dewar, with the temperature dependence and $I-V$ characteristics measured.

6.3.1 Temperature dependence of NbN nanowires

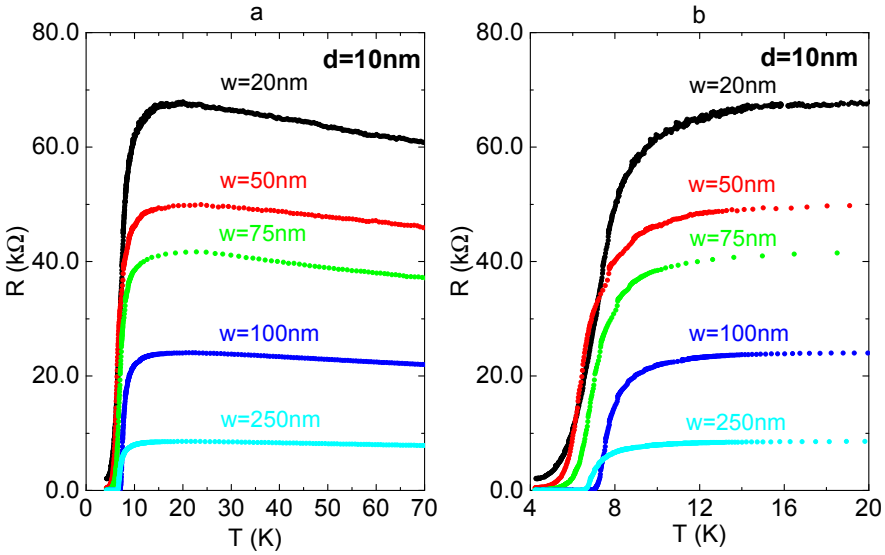

Figure 6.2: **a.** Dependence of resistance on temperature for NbN nanowires. Data for nanowires of thickness $d \leq 10$nm with design widths w of 250nm, 100nm, 75nm, 50nm and 20nm are presented in the plot. The narrowest two sample widths were confirmed using SEM. **b.** Shows the dependence of resistance on temperature for the wires near the transition region.

Figure 6.2 shows the temperature dependance of resistance for NbN nanowires. Plot **a.** shows the overall resistive characteristics of the nanowires. Here the nanowires exhibit a high normal state resistance and a near-insulating characteristic

(indicated by a clearly negative gradient $\mathrm{d}R/\mathrm{d}T$) for $T > T_\mathrm{c}$. As discussed in Chapter 4 this is a good indicator that these nanowires present disordered systems close to the SIT. Both attributes are desirable for the observation of quantum effects and particularly phase slips [84].

In comparison to Figure 6.1, the NbN nanowires exhibit considerably higher normal state resistance. However this is not directly comparable due to the difference in d between the two sets of devices. Looking at resistivity, wires with widths of 50 nm in $Nb_{0.3}Si_{0.7}$ reach a normal state resistivity of $2.5 \times 10^{-3}\Omega$cm, a value identical to wires with equivalent widths in NbN.

Plot **b.** shows the characteristics of the same wires close to the superconducting transition region. Wider samples clearly fall to zero resistance below T_c whilst the narrowest sample appears to reach a resistance of 200 Ω before the base temperature of the cryostat is reached.

A clear scaling of the normal state resistance is observable with reduction of nanowire width, as observed with the Nb_xSi_{1-x} nanowires in Section 6.2 and in nanowires from other materials [13]. In addition, for the nanowires with design widths 50 nm$\leq w \leq$100 nm, T_c is observed to scale with width as expected. The T_c for nanowires with design widths of 250 nm and 20 nm does not appear to scale as predictably as with the other widths. This variation could be due to local inhomogeneities in the material which formed the nanowires with widths w=20 nm and 250 nm. The earlier onset of superconductivity for the 20 nm wide sample suggests a more Nb rich region of the film in that area, however the high normal state resistance does not confirm this in comparison to the w=50nm nanowire.

6.4 Dependence of T_c on nanowire dimensions

In Chapter 4 we demonstrated a linear dependence of T_c on the reciprocal of film thickness for superconducting thin films of $Nb_{0.3}Si_{0.7}$ and NbN. This dependence had been previously demonstrated by other groups in materials of similar dimensions. In this section we present evidence that an inverse proportionality to the characteristic

dimension is also observable for nanowires. Although the link between suppression of T_c and reduced dimension has been documented for nanowire structures [125, 126], to our knowledge only one study has attempted to document an inverse dependence on nanowire width to date [82].

For each of our samples, we have determined the value of T_c using the criterion defined as,

$$T_c = \frac{T(0.9R_n) + T(0.1R_n)}{2} \tag{6.1}$$

where R_n is defined as the normal state resistance for the wires, taken as the peak resistance at the point of the transition to the superconducting state.

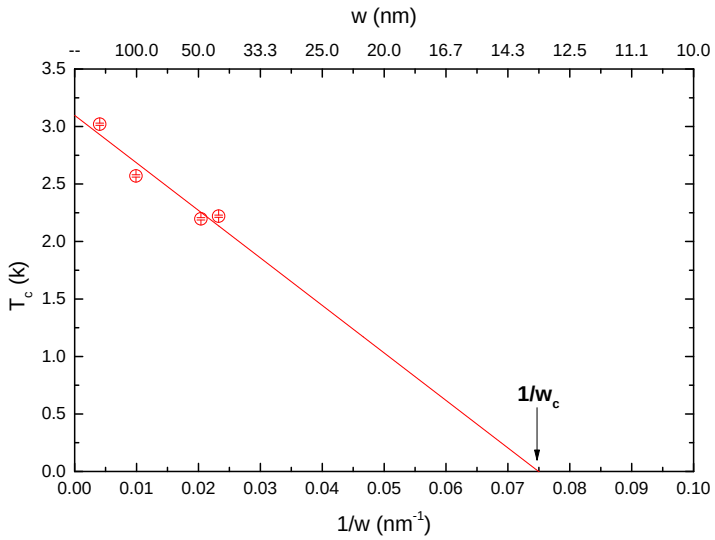

Figure 6.3: Dependence of the wire critical temperature for $Nb_{0.3}Si_{0.7}$ nanowires. Data for nanowires of thickness $d \leq 30$ nm with widths w of 247 nm, 101 nm, 49 nm and 43 nm are represented in the plot by red circles. The solid red line depicts a linear fit to the data.

Figures 6.3 and 6.4 show the variation of transition temperatures with wire width for nanowires of $Nb_{0.3}Si_{0.7}$ and NbN. In Figure 6.3 the data from the $Nb_{0.3}Si_{0.7}$ nanowire samples is represented by hollow red circles whilst the solid line represents a linear fit to the data. A linear dependence in the behaviour of T_c on the inverse width may be observed as indicated by the fit line. Drawing similarities with

work presented in thin films [79, 127] we propose that the points at which this fit intercepts the axes should hold similar significance to in nanowires as they do in thin films, namely a critical width w_c (indicated on the plot) and a bulk T_c, T_{c0}. The 'bulk' T_c value for nanowires T_{c0} in this material is found to be 3.1 K. The width corresponding to the intercept on the 1/w axis is $w_c = 13.3$ nm suggesting that a wire of this dimension from the same film could be expected to undergo an insulating transition. As such, and as discussed in Chapter 4 we take this value to be an estimator of ξ_{GL} in these wires. In comparison to what we have seen in thin films, w_c is approximately 3.5 times larger than the 3.8 nm observed for d_c.

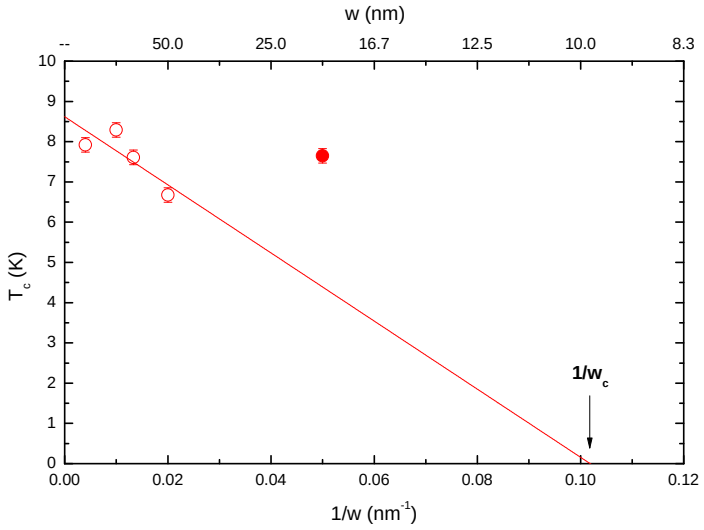

Figure 6.4: Dependence of the wire critical temperature for NbN nanowires. Data for nanowires of thickness $d \leq 10$ nm with widths w of 250 nm, 100 nm, 75 nm, 50 nm, and 20 nm are represented in the plot by hollow red circles. The solid red line depicts a linear fit to the data. The solid red circle, which represents the data for the $w = 20$ nm wire, appears as an outlier and has not been included in the fit[1].

A similar dependence may be observed in the behaviour of the devices from the NbN nanowire set, in Figure 6.4. Though more data is required to confirm the trend, the linear fit to the data indicates a T_{c0} of 8.6 K. According to the fit, the projected critical width at which we should observe an SIT for nanowires in this

[1]Inclusion of the data for the w= 20 nm wire reduces the R^2 coefficient to 0.25. Omission of this data raises this value above $R^2 = 0.5$ indicating a more favourable fit.

material is $w_c = 8.2\,\text{nm}$. This value is expected to be consistent across nanowires made under comparable conditions from the same composition of film. Nanowires of NbN have certainly been reported to superconduct at widths down to 20 nm and below [128, 129]. However, at the time of writing we could find no evidence of reports that could disprove this projection and our own devices as yet have not reached such widths of 8 nm.

The value of w_c found here is approximately twice the value found for the critical dimension d_c in thin films. Given that $\xi_{GL} \propto \sqrt{\xi_{GL} l}$ which in is in turn related to T_c through $\frac{1}{\sqrt{T_c}}$, this increase in the value w_c can be expected given the considerable suppression of T_{c0} observed between the 2D and 1D regimes of this material. Indeed, in comparison to the 5% decrease observed between $Nb_{0.3}Si_{0.7}$ films and nanowires, the variation in T_{c0} from thin films to nanowires of NbN is approximately a 40% reduction. This may indicate a greater degree of disorder in the NbN material than in the $Nb_{0.3}Si_{0.7}$. Such an interjection is made tentatively given the difference in wire thickness between the two materials, and would require further investigation over a range of thicknesses for each material.

6.5 Dilution Refrigerator Measurements Characterising the Impact of Noise on Low Temperature Transport in Nanowires

Our investigations have focussed on the characterisation of material behaviour at temperatures down to 500 mK. As discussed at the start of this chapter and in Chapter 4, the bulk of our measurements were performed either using a dip probe submerged in a liquid helium dewar or in the PPMS system.

The ^{4}He dip probe cryostat

The dip probe provided regular, easy access for measurements down to 4.2 K. The probe itself comprises twelve coaxial dc lines and two rf lines. For the purposes of

our measurements, four point dc measurements are made using an adjustable series resistance to source current. Although it only offers room temperature filtering, the dip probe provided the opportunity for quick characterisation of samples, with a typical temperature dependence at a set current-bias taking between three and five hours.

The QD-PPMS cryostat and limitations in the 1D regime

Infrequent access was available for some of our measurements on the PPMS cryostat. This system provided measurement temperatures down to 500 mK and was the primary tool with which $Nb_{0.3}Si_{0.7}$ film and nanowire samples were characterised, due to their lower T_c on comparison to NbN. The ^{3}He measurement puck for the PPMS comprised four pairs of unfiltered copper dc lines for two simultaneous four-point measurements. The system offered a great deal of control in measuring samples, with the capability to stabilise temperatures before taking each measurement. This did, however, increase measurement time, with an average, detailed thermal cycle lasting approximately 36 hours.

On moving to the 1D regime, unexpected characteristics began to emerge in the low temperature behaviour of the samples. This manifested particularly in the resistive plateaus such as those visible in Figures 6.1 **a.** and **b.**. The behaviour was observed for NbN nanowires to a lesser degree, but it was particularly pronounced for $Nb_{0.3}Si_{0.7}$ nanowires. In both materials, the behaviour can be seen to become increasingly pronounced in nanowires of smaller widths

Our initial belief was that the cooling power of the PPMS was not sufficient to observe a full transition to the superconducting state in smaller nanowire devices[2]. On this basis, measurement time on a dilution refrigerator was sought in order to investigate the behaviour of wires at lower temperatures, which should be able to suppress the influence of local thermal effects.

This was kindly granted by Prof. John Morton at UCL, for the purpose of this

[2]It was believed that the larger features in the wires, such as the pads and tracks, were undergoing a transition whilst the smaller features remained normal due to suppressed T_c.

investigation and a limited set of $Nb_{0.3}Si_{0.7}$ nanowire samples were subsequently characterised on an Oxford Instruments Triton 200 cryogen-free dilution refrigerator (DR). Samples were shielded from the external environment by successive Faraday cages formed by the puck enclosure at the level of the mixing chamber, and the body of the refrigerator itself. All lines to the sample were shielded, and unused lines were capped or earthed appropriately. No further internal filtering was present within the DR for the duration of the measurements. This setup provides a complete enclosure for our samples and good reduction of the influence from external noise.

$I - V$ characteristics of the nanowire samples were investigated at low temperatures to assess the impact of filtering on nanowire behaviour. Measurements were made at a base temperature of 115 mK.

6.5.1 Dilution measurement setup

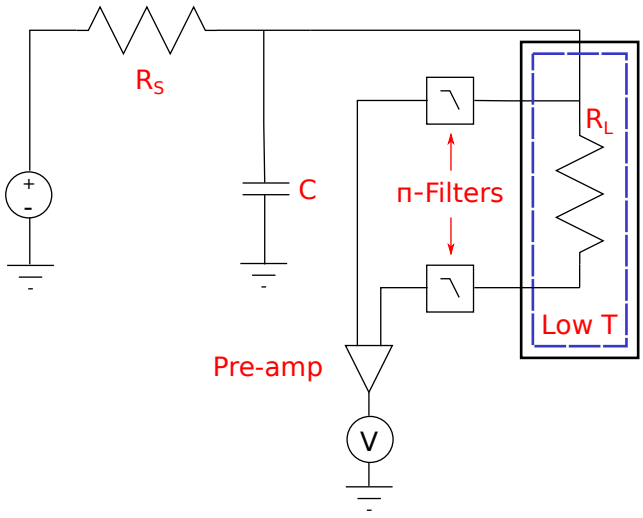

Figure 6.5: Measurement circuit schematic illustrating the set up used to current bias nanowire samples within the Dilution Refrigerator. A room temperature series resistor and shunt capacitance was used to form an RC filter applied to the current bias line in succession to the voltage source. The dashed box indicates the sample puck on the mixing plate at mK temperatures. Tusonix 4209-053LF π filters, rated at 5500 pF, were used between the sample and the voltage preamp to suppress EM/RF interference propagating back to the sample via the voltage leads.

Figure 6.5 illustrates the setup used for the measurements. A Yokogawa GS200

DC Voltage/Current source was used with a series resistance R_s to source current to the samples at low temperature. A shunt capacitance C combined with the series resistance were used to form a low pass filter. In addition, π filters were applied to the measurement lines at room temperature, between the sample and the voltmeter. A Keithley 2400 Source Meter was used to monitor the voltage drop across the nanowire samples during characterisation. Values of R_s and C were varied to investigate the impact of low pass filtering on the measurement output.

6.5.2 Variation of nanowire behaviour in response to the RC time constant

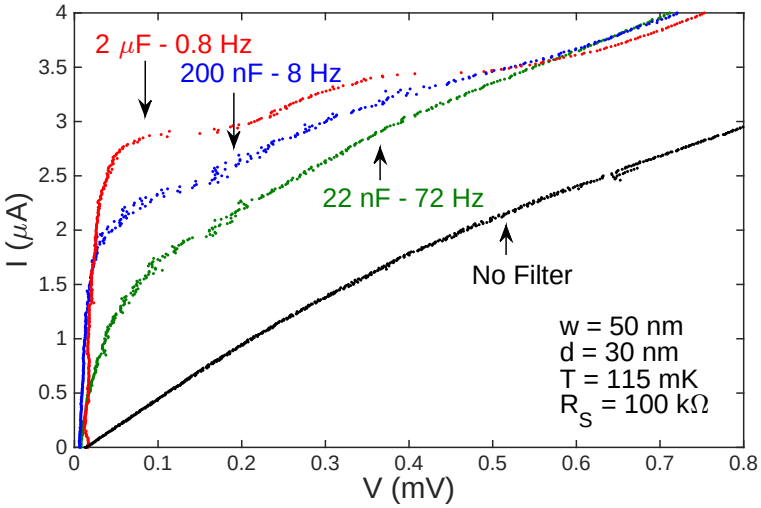

Figure 6.6: $I-V$ characteristics of a 49 nm wide $Nb_{0.3}Si_{0.7}$ nanowire at 115 mK. The series resistance R_s was constant in order to maintain the noise associated with series resistance. The capacitance C was varied in order to investigate the impact of the filter bandwidth on the nanowire $I-V$ characteristics.

Figure 6.6 shows the $I-V$ characteristics of a 49 nm $Nb_{0.3}Si_{0.7}$ nanowire at 115 mK. The bandwidth of the RC low-pass filter was varied to investigate the impact of filtering on the $I-V$ characteristics of the nanowire. R_s was held at 100 kΩ to maintain the noise associated with the series resistance constant.

Without filtering, the $I-V$ characteristic shows no sign of superconductivity, exhibiting a near ohmic resistance characteristic of approximately 220 Ω, as high-

lighted by the black datapoints. The green line depicts data from the setup where a 22 nF capacitance was used, corresponding to a frequency cutoff of 72.3 Hz. Here a change in the $I-V$ begins to appear, however it is not clearly defined as a critical current feature until the bandwidth is further reduced. As the cutoff frequency is reduced, the I_c feature becomes more pronounced, with a value of approximately 2.8 µA.

6.5.3 Impact of the series resistance on nanowire behaviour

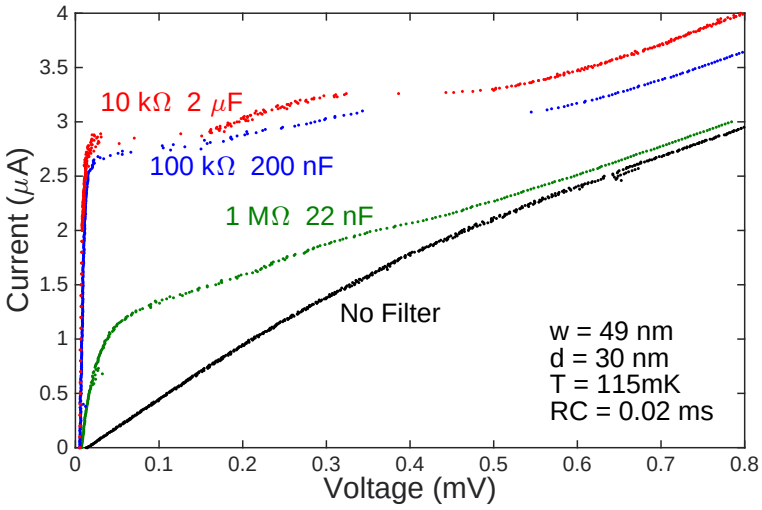

Figure 6.7: $I-V$ characteristics of a 49 nm wide $Nb_{0.3}Si_{0.7}$ nanowire at 115 mK. During the measurement the bandwidth of the RC filter was maintained with an RC time constant of 0.02 ms. The noise associated with series resistance was investigated by varying the value of R_s.

Similarly Figure 6.7 shows the results of the investigation into the impact of resistance on the measurement of a 49 nm $Nb_{0.3}Si_{0.7}$ nanowire at 115 mK. The value of C was adjusted to hold the RC time constant fixed at 20 µs whilst the value of R was investigated. Again, the black data points show the ohmic behaviour of the wire before any filtering is applied. The dark green line shows the data when filtering is applied. A poorly defined I_c feature begins to emerge in the $I-V$ at approximately 1.25 µA. As the value of R is reduced the critical current feature becomes sharper and more defined, and the critical current value increases by more

than a factor of 2. For a series resistance of R_s =10 kΩ, the lowest series resistance investigated, the sample exhibits an I_c of approximately 2.8 μA.

6.5.4 Origins of dependence on filtering

The origin of this dependence on filtering indicates a susceptibility to noise in the measurement. This becomes evident from the $I-V$ plots in Figure 6.6 where superconductivity is restored as the bandwidth of the filter is reduced from the unfiltered regime to the smallest cutoff frequency of approximately 1 Hz. Where a dependence on a series resistance is observed for a constant bandwidth in Figure 6.7, one would deduce that the primary contributor to noise in a measurement is thermal in the form of room temperature Johnson noise. This type of thermal noise arises due to the voltage fluctuations caused by the Brownian motion of electrons in the resistive material. For a resistance R at temperature T, the mean square voltage variance $\bar{v_n}^2$ associated with thermal noise for a bandwidth f_{bw} would be given by:

$$\bar{v_n}^2 = 4k_B T R f_{bw}. \tag{6.2}$$

The equivalent for mean square current variance $\bar{i_n}^2$ is given by:

$$\bar{i_n}^2 = \frac{4k_B T f_{bw}}{R}. \tag{6.3}$$

R (kΩ)	C (nF)	f_{bw} (Hz)	v_n (nV)	i_n (pA)
10	2000	7.96	35	3.6
100	200	7.96	113	1.1
1000	22	7.23	342	0.3

Table 6.1: Table comparing estimates for the voltage and current noise contributions to the $I-V$ curves plotted in Figure 6.7. Calculations are made assuming a room temperature of 293 K.

Table 6.1 shows the respective variation in current and voltage noise for each of the RC combinations used in Figure 6.7, as calculated using Equation 6.2 and

Equation 6.3. We assume the contribution from the high input resistance on the voltmeter is negligible in comparison to the series resistance, as the resulting cut-off frequency should be well below that associated with R_s[3]. All calculations are made assuming a room temperature of 293 K. As can be seen in the table, the voltage noise associated with the resistor is indeed reduced as one might expect from the Johnson noise relationships given above. Likewise, the current noise associated with the series resistance is also affected, increasing as the resistance is decreased. Interestingly, the curve corresponding to the 10 kΩ resistor in Figure 6.7 does exhibit visibly broader variation for current than the curves corresponding to the other resistors. However, the scale of the broadening appears to be larger than the pA ranges predicted by our estimates.

Comparing the voltage and current noise calculated in each of these cases to the plots in Figure 6.7, the values calculated do not appear to account for the drastic change in the $I - V$ characteristic. However, these values are calculated with respect to the bandwidth allowed by the RC filter cutoff frequency. Thus, they represent the respective voltage and current noise at these bandwidths but not the noise characteristic of the setup during the unfiltered measurement.

The unfiltered measurement was taken whilst sourcing current through a series resistance of 100 kΩ. The supply to the nanowire current contact, encompassing the connection from the voltage source to the resistor and the subsequent connection the the DR breakout box, were made using BNC connector cables. Since no further filtering was applied we assume that the bandwidth for unfiltered measurement is determined by the BNC connections to the resistor and DR. We use a bandwidth of 1 GHz for the BNC cables and connectors, a value taken from the technical datasheet for these cables [130]. The corresponding estimates for the voltage and current noise for such a measurement are calculated to be 1.3 mV and and 12.7 nA. These values are far more substantial in comparison to those listed for the filtered configurations in Table 6.1. The mV of voltage noise attributed to the unfiltered

[3]The Keithley 2400 series is rated with an sense impedance of $> 10^{10}\Omega$

BNC cables could provide a plausible explaination for the variation in the I-V characteristics observed between the filtered and unfiltered measurements in Figure 6.7.

6.6 Conclusions

In this chapter we have presented the low temperature characteristics of nanowires fabricated from thin films of $Nb_{0.3}Si_{0.7}$ and NbN. The temperature dependence of the resistance for all samples presented an increasingly insulating behaviour as dimensions were confined through the reduction of widths. This behaviour demonstrates commonly observed increases in the manifestation of disorder in the electrical characteristics of materials as the current path is confined. Superconductivity was confirmed for 1 µm long wires of widths down to 43 nm in $Nb_{0.3}Si_{0.7}$ and 20 nm in NbN.

We have reported on a linear characteristic in the relationship between nanowire T_c and the reciprocal of the wire width w. To our knowledge there is only one other report of a dependence of nanowire T_c on width. As we described in Chapter 2, Graybeal *et al.* present a dependence in MoGe nanowires where they observe a normalised departure ofT_c proportional from the 2D value that is proportional to w^{-2} [82]. The authors interpreted the power two dependence to be an indicator that their wires are still in the two-dimensional limit. The behaviour of our nanowires is consistent with w^{-1}. Following the logic put forward by Graybeal *et al.*, this could suggest that our samples are within the one-dimensional limit for these materials. Such an implication for our samples is particularly important with respect to their use in the investigation of QPS phenomena.

Based on similar relationships observed for thin films, we have identified a critical width w_c by projection of the characteristic to its intercept on the 1/w axis and a bulk T_c projection. The projection for T_{c0} was estimated to be 3.1 K for $Nb_{0.3}Si_{0.7}$ and 8.3 K for NbN. Both projections show an expected suppression of T_{c0} on confinement to nanowire dimensions from thin films. The projections for

$Nb_{0.3}Si_{0.7}$ wires in close agreement with the respective values of 3.2 K found for thin films using the Finkel'stein approximation in Chapter 4. The predicted T_{c0} in NbN nanowires shows a considerably larger suppression from the 13.5 K film value, which could be attributed to a greater impact of disorder observed here due to the smaller thickness of the nanowires when compared to the $Nb_{0.3}Si_{0.7}$ counterparts.

A residual resistance plateau characteristic was observed in nanowires of w<100 nm for $Nb_{0.3}Si_{0.7}$ and w<75 nm for NbN. Similar residual resistance characteristics have been observed by other groups and were attributed to quantum effects through the application of models such as those of Giordano [52] and Golubev and Zaikin [50, 12]. However, in dilution refrigerator measurements we have used room temperature low pass filters to restore superconductivity to one of our samples[4][5] which showed that quantum effects were not responsible for the resistive state observed in our samples. We demonstrated that a significant variation in the voltage signal can be expected due to room temperature Johnson noise which will contribute to the observed resistive state observed in the nanowire. The result of this study demonstrates the necessity of well filtered measurement environments when measuring superconductivity in nanometre scale devices.

Our NbN nanowires were shown to maintain high values of T_c even at reduced dimensions when compared to wires of similar widths from $Nb_{0.3}Si_{0.7}$. This is an attractive characteristic for practical purposes of measurements as these values of T_c should allow for isolation from the influence of thermally driven phenomena such as TAPS on more detailed measurements at lower temperatures.

In the next chapter we compile the results of our investigations in characterisation of these materials and study the feasibility of incorporating nanowire

[4]It can be argued that the residual resistance observed in the unfiltered measurements does not match the resistance observed in the plataeu in Figure 6.1. However, both the measurement temperature and the measurement setup are different here. The measurement electronics of the PPMS system will have a different noise characteristic to those of the Kiethley and Yokogawa sources used in the dilution refrigerator measurements. Our results suggest that room temperature measurement noise must be taken into consideration when measuring smaller wires.

[5]In the first instance, this result may only impact our earlier conclusions based on the temprerature dependence for narrower samples in the $Nb_{0.3}Si_{0.7}$ material. Larger wires did not exhibit a residual resistance. NbN samples do not appear to exhibit the same susceptibility to this effect.

devices made from these materials into a device for the investigation of quantum phenomena in superconducting nanowires.

Chapter 7

Feasibility Study on the Integration of Superconducting Nanowires into a Current-Standard QPS Circuit

7.1 Introduction

As described in Chapter 2 an important area of application for superconducting nanowires is the investigation of Quantum Phase Slip phenomena and related behaviours. In the previous two chapters we have demonstrated our capability to fabricate and manipulate thin superconducting films, tuning characteristic behaviours and creating nanowire structures below 20 nm in size. We now look at the feasibility of integrating our nanowire structures into circuits, and the possibility to recreate the current-dual of the Shapiro step experiment theorised by Mooij and Nazarov [3].

We begin by giving a brief overview of these predictions and the origins of the equivalent circuit we will be studying. We then present a study using data gathered in Chapters 4 and 5. Here we model the impact of the circuit elements on critical

parameters of the QPS phenomenon, optimising quality factors and characteristic energies. We proceed to designing a physical realisation of the circuit, and show our prototype alongside preliminary measurements made.

7.2 The Mooij-Nazarov Prediction

7.2.1 Flux-Charge duality

As discussed in Chapter 2, Mooij and Nazarov [3] suggest that a 1D superconducting nanowire will behave as the exact dual of the Josephson junction, at temperatures well below T_c. Such a nanowire or QPS junction should therefore yield an effect akin and dual to the Josephson charge tunneling. By exchanging the complementary quantum variables of phase and charge the authors generate a set of relationships describing the proposed QPS system from the relationships known for the Josephson effect. A summary of interchangeability between the critical parameters for the two structures is made in Table 7.1.

The authors cite earlier work by Büchler *et al.* who theorised that QPS could be coherent and go on to demonstrate duality based on the suggestion that the low-temperature physics of QPS junction would reduce to that of a Josephson junction in a host circuit.

Josephson junctions	QPS junction	Parameter Relation
Elementary charge e	Flux quantum Φ_0	$e \leftrightarrow \Phi_0$
Capacitance C	Inductance L_k	$C \leftrightarrow L_k$
Coupling energy E_J	Phase slip energy E_S	$E_J \leftrightarrow E_S$
Charging energy E_C	Inductive energy E_L	$E_C \leftrightarrow E_L$
Critical current I_c	Critical voltage V_c	$I_c \leftrightarrow V_c$

Table 7.1: Table summarising the interchangeability of parameters between the Josephson model and the QPS model.

7.2.2 The fundamental parameters in a QPS system

As with the Josephson effect, certain parameters are important to the design of a QPS circuit. Mooij and Nazarov derive these from their Josephson counterparts to be the phase slip amplitude or energy E_S, the inductive energy E_L, the critical voltage V_c, the kinetic inductance L_k, the plasma frequency ω_p, the characteristic

frequency ω_c and the quality factor Q_{qps}.

The phase slip energy E_S and the inductive energy E_L

The phase slip energy is introduced as E_S and is dual to the Josephson coupling energy E_J. Mooij and Nazarov approximate this to be $E_S/h = 100\,\text{GHz}$ for a 1μm nanowire. We may estimate E_S from $E_S = \Gamma_{qps}\hbar$. Introduced in equation 2.5, Γ_{qps}, the rate of QPS events in the nanowire is given by [58]:

$$\Gamma_{qps} = 1.5m\frac{L_{nw}}{\xi_{GL}}\sqrt{\frac{R_q}{R_\xi}}\frac{k_B T_c}{\hbar}\exp^{-0.3n\frac{R_q}{R_\xi}}. \tag{7.1}$$

Here, L_{nw} is the length of the nanowire, R_ξ is defined as the normal state resistance of a length ξ_{GL} of wire and m and n are constants of order 1. ξ_{GL} and R_q have been previously defined as the Ginzburg-Landau coherence length and the resistance quantum respectively.

The inductive energy E_L is dual to the charging energy E_C in a Josephson junction. For a Josephson junction with junction capacitance C_k, $E_C = 2e^2/C_k$ where e is the elementary charge. Given the duality of the QPS system with the Josephson system, Mooij and Nazarov suggest the interchangeability of the Cooper pair charge with the flux quantum $2e \leftrightarrow \Phi_0$ and the junction capacitance with the kinetic inductance in a superconducting nanowire $C \leftrightarrow L_k$ (the kinetic inductance is defined later in this section). This gives E_L to be,

$$E_L = \frac{2\Phi_0^2}{L_k}. \tag{7.2}$$

For $E_S \ll E_L$, the phase is well defined and only small amplitude (or "weak") phase slips are expected to occur. For the limit where $E_L \ll E_S$ the charge is well defined and large amplitude (or "strong") phase slips are expected to be observable.

The critical voltage V_c

For a conventional Josephson junction, where $E_C \ll E_J$, a zero-voltage state exists where the phase of the junction is trapped in a potential minimum of the

washboard potential. These minima exist provided the critical current I_{c} of the junction is not exceeded, where I_{c} is defined by $I_{\mathrm{c}} = 2\pi E_J/\Phi_0$. Using the similarity of the two systems Mooij and Nazarov consider a dual washboard potential for the charge variable. In this model the charge may be trapped in minima instead of the phase, resulting in a zero current insulating state provided that a critical voltage threshold V_{c} is not exceeded. By duality, V_{c} is shown to be given by:

$$V_{\mathrm{c}} = \frac{2\pi E_{\mathrm{S}}}{2e}. \tag{7.3}$$

The kinetic inductance L_{k}, capacitance C_{k} and the resulting QPS plasma frequency ω_{p}

Josephson tunnel junctions exhibit a shunt capacitance due to the parallel-plate like geometry of the junction structure. A kinetic inductance L_{k} will also be observed when the system is driven, due to the kinetic energy of the electrons in the system. The combination generates a resonance at a plasma frequency ω_{p}, given by $\omega_p = \sqrt{2E_J E_C}$. The nanowire geometry of a QPS junction implies a kinetic inductance coupled with a kinetic capacitance C_{k}. For a system with critical voltage V_{c} and charge q, the kinetic capacitance is given by $C_{\mathrm{k}} = 2e/(2\pi V_c \cos 2\pi q)$.

For the purposes of this work we use the estimation of L_{k} as provided by Webster *et al.* [62] based on an earlier article by Mattis *et al.* [131]. For a length of superconductor with normal state resistance R_N, superconducting energy gap Δ and critical temperature T_{c}, the kinetic inductance at $T \to 0$ is estimated by

$$L_{k,0} = \frac{\hbar R_N}{\pi \Delta_0} \approx 0.18 \times \frac{\hbar R_N}{k_B T_c} \tag{7.4}$$

where $\hbar$ and k_B are the reduced Planck constant and the Boltzmann constant respectively. The resulting resonance of the QPS system is given by

$$\omega_p = \sqrt{2E_{\mathrm{S}}E_{\mathrm{L}}} = \sqrt{\frac{\pi V_{\mathrm{c}}}{eL_{\mathrm{k}}}}. \tag{7.5}$$

Both E_{S} and L_{k} are proportional to the wire length [3] whilst E_{L}, from Equation 7.2, is inversely proportional to L_{k}. Thus the plasma frequency remains constant irrespective of the length of the wire.

The quality factor $Q_{\mathbf{qps}}$

Driven at its plasma frequency a Josephson junction will exhibit an environmental impedance linked to its own capacitance and the inductance of wiring connections. For a QPS nanowire junction, Mooij and Nazarov propose that, for a wire with series resistance R_{s}, this environmental impedance will lead to a plasma oscillation quality factor Q_{qps} that may be rewritten as

$$Q_{\mathrm{qps}}^2 = \frac{\pi V_{\mathrm{c}} L_{\mathrm{k}}}{2eR_{\mathrm{s}}^2} = 2\pi^2 \frac{E_{\mathrm{S}}}{E_{\mathrm{L}}} \left(\frac{R_{\mathrm{q}}}{R_{\mathrm{s}}}\right)^2 . \tag{7.6}$$

The significance of the series resistance R_{s} will be discussed in the following section.

7.2.3 Equivalent circuits & further considerations

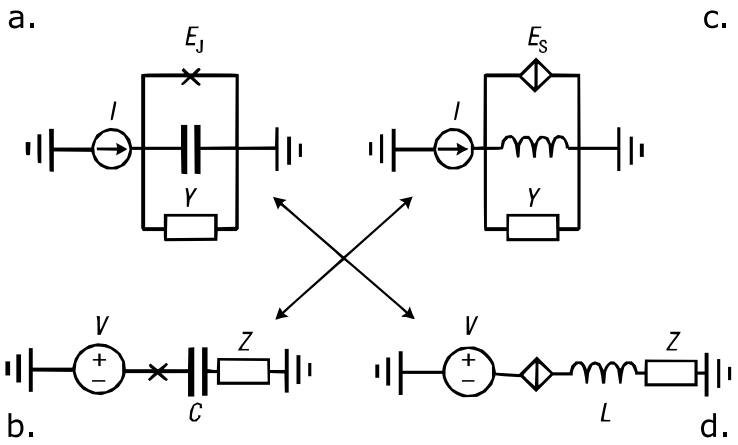

Figure 7.1: Josephson and QPS junction equivalent circuits based on the duality of the two systems. **a** shows a current-biased Josephson junction, **b** a voltage-biased Josephson junction, **c** a current-biased QPS junction and **d** a voltage-biased QPS junction. Circuits **a** and **d**, and **b** and **c** respectively are exact duals of each other. Adapted from Mooij and Nazarov [3]

Four circuits are shown in Figure 7.1 comprising two well-known Josephson junction setups and two QPS junction setups that Mooij and Nazarov propose as

equivalents [3]. Of particular interest to this feasibility study is the relationship between circuits **a** and **d**. The current-biased Josephson junction has been used to demonstrate Shapiro steps (i.e. steps at constant voltage) which have provided the scientific community with a voltage standard of a few parts in 10^{11}, a value whose accuracy remains unrivalled to date. Based on the duality of the Josephson and QPS systems Mooij and Nazarov proposed that a voltage-biased QPS nanowire junction, depicted in Figure 7.1 as struck-through diamond, should display equivalent "Shapiro-like" steps at constant current when an rf voltage is applied. For a frequency of ν, these steps are predicted to be given by $I_n = 2ne\nu$, where n is an integer. Following the Josephson voltage standard, this would generate steps separated by 26 nA with an applied frequency of 80 GHz.

Achieving non-hysteretic behaviour & the necessity of R_s

Mooij and Nazarov make several recommendations to create QPS devices that do not exhibit hysteretic $I-V$ behaviour. The first is in relation to the amplitude of the applied RF signal V_ac. Non-hysteretic behaviour is expected for signals where $V_\mathrm{ac}/V_\mathrm{c} \approx 1/Q_\mathrm{qps}$.

Devices that exhibit a low quality factor are also recommended. High values of Q_qps are expected to give rise to hysteretic behaviour and frequencies that are unrealistic for measurements. Mooij and Nazarov recommend the inclusion of a high series resistance R_s in the device in order to limit hysteretic behaviour since Q_qps is inversely proportional to R_s.

The ratio $E_\mathrm{S}/E_\mathrm{L}$ & the necessity of an inductor line

We have already discussed the fact that large strong phase slips are expected to occur in the regime $E_\mathrm{S} \gg E_\mathrm{L}$. The ratio $E_\mathrm{S}/E_\mathrm{L}$ then becomes a useful indicator for assessing the suitability of a QPS device. In the first instance, Mooij and Nazarov suggest this ratio cannot be smaller than 4 in order for the charge to be well defined. Using the second form of Equation 7.6, this ratio implies a series resistance in excess of 60 kΩ for a quality factor of 1.

In a Josephson junction, the reduction of junction area serves to lower the ratio E_J/E_C. Likewise it can be expected that wires that are shorter in length are expected to have a lower ratio E_S/E_L than longer QPS wires. However, it has been observed that QPS can destroy superconductivity completely in particularly long wires, causing a transition into the insulating state. As such a balance must be struck, with wires of 1 μm in length recommended as a benchmark [3].

The ratio may be further maximised by reducing E_L with respect to E_S. The inclusion of a wider section of wire has been proposed to effectively lower E_L. This has the added benefit of reducing the plasma frequency for more practical measurement without affecting E_S. Physically this manifests itself as an inductor line element of the same superconducting material as the QPS junction.

7.3 Simulations of the QPS system

We present simulations of the QPS critical parameters discussed in the previous section. All calculations were made using Matlab to model the relationships we introduced in the previous section. The calculations were made using parameter values extracted from data in our investigations in Chapters 4 and 5. Estimations for Γ_{qps} were made assuming a nanowire width of 10 nm and length of 1 μm. The value of critical voltage V_c was calculated using the values of E_S modelled on our films. The inductance was calculated based on a length of 900 μm which was set as a benchmark based on initial design estimates.

7.3.1 Relationship of E_S/E_L on film thickness and kinetic inductances

Figure 7.2 shows the relationships between the ratio of E_S/E_L with inductor width for devices made in $Nb_{0.3}Si_{0.7}$ and NbN from **a.** $d = 10$ nm and **b.** $d \simeq 20$ nm thick films respectively. Both highlight a linear dependence on the inverse proportionality of the energy ratio to the inductor width. A comparison of the two materials against each other shows that devices fabricated from $Nb_{0.3}Si_{0.7}$ offer a higher energy ratio than those fabricated from NbN in our compositions.

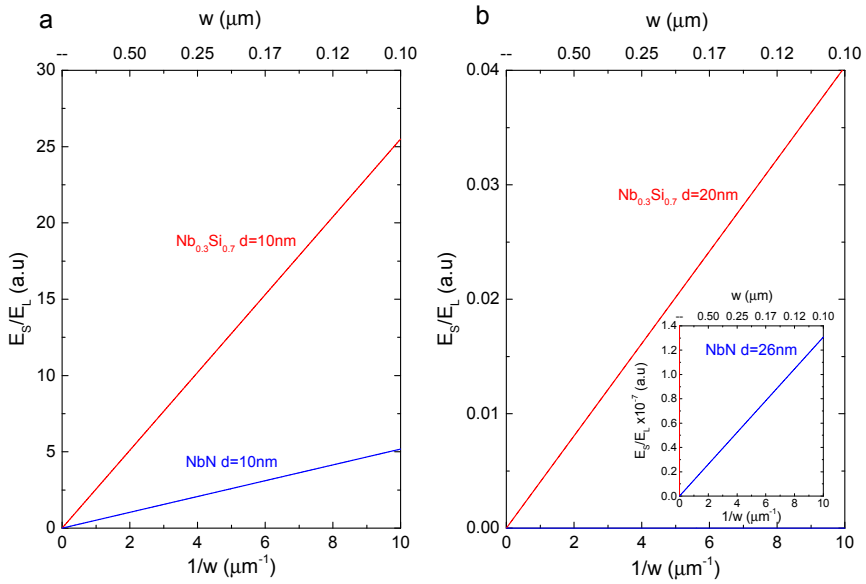

Figure 7.2: Modelled data on the relationship between E_S/E_L and inductor width L for $Nb_{0.3}Si_{0.7}$ and **b.** NbN materials. Plot **a.** presents the modelled relationship for the $d = 10$ nm films from each material, while plot **b.** shows the modelled relationship for the $d = 20$ nm $Nb_{0.3}Si_{0.7}$ film, with the $d = 26$ nm NbN film shown inset. The relationships are modelled based on the experimental data gathered in Chapter 4. E_S is calculated assuming a nanowire width of 10 nm and length of 1 μm for both films.

Comparing the results for different film thicknesses, the model predicts a more favourable ratio of E_S/E_L for thinner films. This suggests that the cross sectional dimensions of the inductive elements in the circuit should be minimised by design in order to generate more desirable ratios.

7.3.2 Optimisation of the quality factor

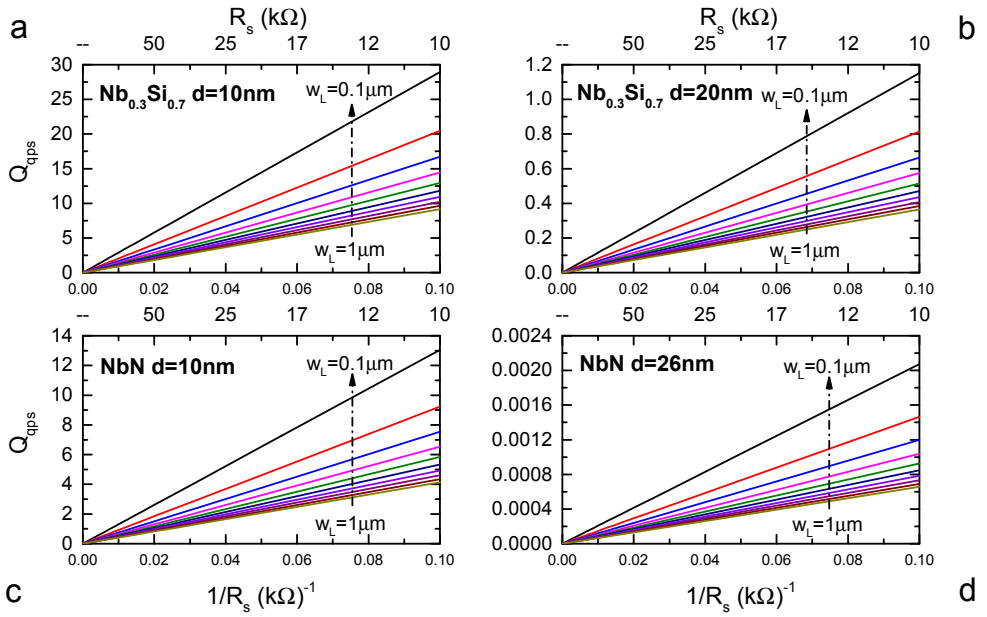

Figure 7.3: Modelled dependence of the quality factor on series resistance and inductor width in a QPS circuit. Plots **a.** and **b.** show the relationship in devices made from $Nb_{0.3}Si_{0.7}$ films for $d = 10$ nm and $d = 20$ nm respectively. Plots **c.** and **d.** show the same relationship for devices from NbN films with $d = 10$ nm and $d = 26$ nm respectively. Each plot shows the quality factor for inductor widths w_L =100 nm to w_L =1 μm for structures in the respective materials.

Figures 7.3**a.-d.** show the relationship between the modelled circuit quality factor and circuit series resistance for $Nb_{0.3}Si_{0.7}$ and NbN films. Each figure presents the relationships for a set range of inductor line widths and adjacent figures compare data for a thinner and thicker film sample.

The results suggest that higher Q factors are attainable from circuits fabricated using thinner films in each material. As discussed in Section 7.2.2 Kautz [132] suggested that high Q factors are to be avoided in order to limit hysteretic behaviour

in the final circuits. We have already established from the results presented in Section 7.3.1 that thinner films are preferable for maximising the phase slip energy ratio. Since the results show an inverse proportionality on both inductor width and series resistance, we may maximise the series resistance and inductor width in order to limit the expected Q factor in the final circuit.

Plot **a.** and and plot **c.** show the relationship between Q_{qps}, $R_{\square}$ and w_{L} for the thinnest films of $Nb_{0.3}Si_{0.7}$ and NbN. On comparison of the two plots, devices made from films of NbN are predicted to offer lower quality factors than those made from films of $Nb_{0.3}Si_{0.7}$. As discussed in Section 7.2.2, $Q < 1$ is desirable for the observation of dual Shapiro steps. To remain within this limit in plot **c.**, a series resistance of over 100 kΩ is required.

7.3.3 Optimisation of ω_p

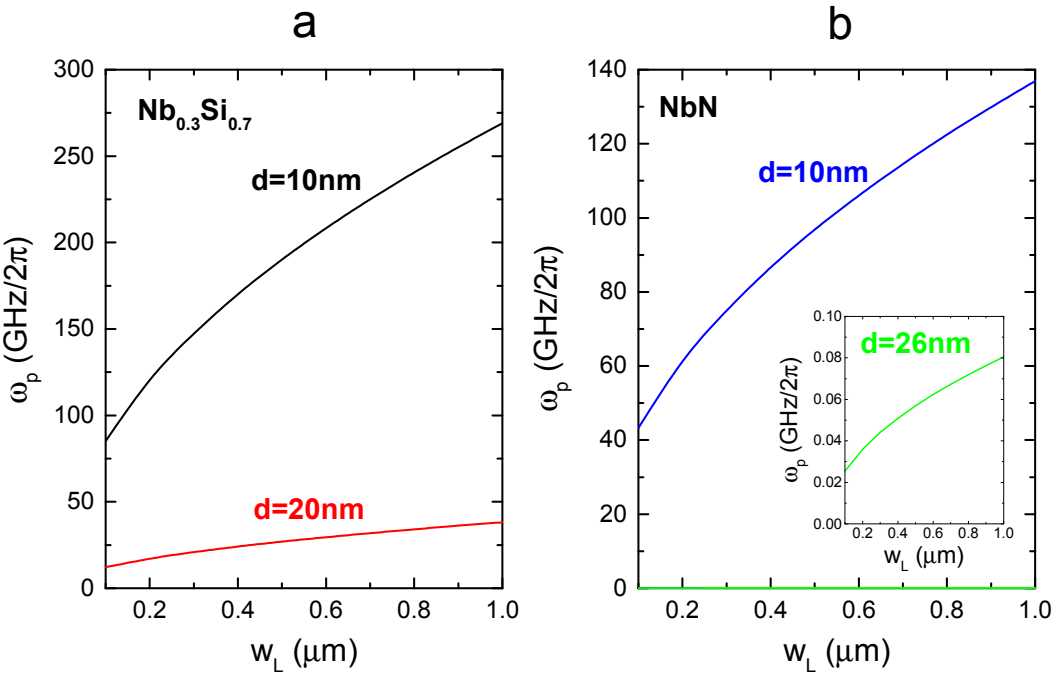

Figure 7.4: Simulated dependence of the plasma frequency on inductor width for inductor film thickness d. **a.** illustrates this relationship for QPS circuits from $Nb_{0.3}Si_{0.7}$ films, whilst **b.** illustrates the relationship for circuits using NbN films.

Figure 7.4 shows the results of the simulated relationship between ω_{p} and

the inductor line width, comparing the results for **a.** $Nb_{0.3}Si_{0.7}$ and **b.** NbN. In each case, ω_p can be minimised by minimising the value of w_L, although the use of thicker films is predicted to generate lower plasma frequency ranges. This is consistent with the inverse dependence of ω_p on L_k and L_k's direct proportionality on the normal state resistance of the superconducting film.

For practicality in the measurement, a lower frequency is desirable. NbN offers lower ranges of ω_p with the curve corresponding to films with thicknesses of $d = 26\,\text{nm}$ (inset) predicting values below 80 MHz.

7.3.4 Selection of materials and dimensions for design

Based on the results of the preceding sections we may now discuss and select optimised parameters and materials for the circuit prototype.

Parameter selection

In section 7.3.1 we presented the results of simulations on the E_S/E_L ratio. Here we found that higher ratios may be attainable when using thinner films for the fabrication of the superconducting elements. This aligns well with our fabrication process which is a dry etching technique that relies on PMMA as a resist material. The slow etch rate of Nb films coupled with the comparatively poor etch resistance of polymer resists further increases the need for thin superconductor layers.

In addition to using a thinner film, the results of the simulations for E_S/E_L demonstrate the inverse dependence of E_S/E_L on inductor width. Minimising the width of the inductor line is predicted to lead to considerable improvements in the E_S/E_L ratio. However, we must also consider that Mooij and Nazarov suggest that E_S/E_L must have a value greater than four for observable quantum behaviour [3]. For the 10 nm thick films of $Nb_{0.3}Si_{0.7}$, a ratio of four is seen for values of $w_L < 0.75\,\mu\text{m}$. In comparison, ratios in excess of four are seen in NbN films where $w_L < 0.15\,\mu\text{m}$.

There is a practical lower limit to the inductor width. The relationship between predicted quality factor in the circuit and the inductor width is also an inverse

proportionality. However, as discussed in the previous section, lower values of Q_{qps} are desirable to limit hysteretic behaviour and (as shall be explained) for the observation of dual Shapiro steps. As such, there is a tradeoff between maximising $E_{\mathrm{S}}/E_{\mathrm{L}}$ and minimising Q_{qps} to within a reasonable range.

We therefore selected a benchmark width of 100 nm for the inductor line width. According to our simulated estimates from Figures 7.2 and 7.4, this should provide $E_{\mathrm{S}}/E_{\mathrm{L}}$ ratios of between 5-25, and plasma frequencies of between 45-100 GHz, the final value in each case dependent on the material selected.

In the selection of the value of R_{s} in the circuit, consideration must be given to the impact of the selection on the circuit quality factor. We have discussed that Q must be minimised in order to limit hysteretic behaviour predicted by Mooij and Nazarov. They do not define a set limit for this but do recommend circuit series resistance should be kept above 60kΩ. For the Josephson voltage standard, phase locking to an applied rf signal at a known frequency permits the observation of Shapiro steps relative to that frequency. Kautz [132] recommends that in order to prevent chaotic behaviour arising in such systems and preventing phase locking, the quality factor of such a circuit should be kept below 1. The results in Figure 7.3 show that the circuit Q factor may be minimised using higher values of R_{s}. For an inductor of width 100 nm, this criterion results in values of $R_{\mathrm{s}} \geq 300\,\mathrm{k\Omega}$ for $Nb_{0.3}Si_{0.7}$ and $R_{\mathrm{s}} \geq 100\,\mathrm{k\Omega}$ NbN based QPS circuits.

Material selection

For the selection of the material our simulations have predicted that $Nb_{0.3}Si_{0.7}$ could offer more favourable ratios of $E_{\mathrm{S}}/E_{\mathrm{L}}$ than NbN for film thicknesses of 10 nm. However, the use of $Nb_{0.3}Si_{0.7}$ would result in a factor two increase in the expected plasma frequency and would also serve to maximise the value of Q_{qps}.

Another consideration that we take in the selection of the material for the first prototype is the values of T_{c} for each of the materials. A high T_{c} is more desirable in terms of measurement practicality as it allows for a wider gap between

the transition temperature and the measurement base temperature of the cryostat. This in turn reduces the influence of thermal fluctuations in the measurement. Here, our NbN films have demonstrated a considerable advantage with T_c values of 8.2 K for a 10 nm thick film compared to 2 K in our $Nb_{0.3}Si_{0.7}$ films, as documented in Chapter 4.

Finally, of considerable importance to our final selection, is the recent publication of experimental work by Peltonen *et al.* [16], demonstrating that QPS can be observed in NbN with the use of a QPS qubit structure. Although recommended as suitable systems for the observation of QPS, the phenomena have yet to be demonstrated in Nb_xSi_{1-x}. This gives strong support to the choice of NbN as the material for the first current-standard prototype circuit we fabricate.

7.4 Design

7.4.1 Resistor design

In [62] Webster *et al.* document the measurement of a similar QPS device for the observation of Shapiro-like steps in current. In this measurement the steps were washed out due to heating of the sample by the on-chip resistors that provide the high value of R_s for the circuit.

In order to minimise the heating generated by on-chip resistors for our prototype we have chosen to move away from the standard bar structure resistor used in previous designs. Fundamentally, we chose to design our resistor structures to increase the surface area of the resistor in order to maximise dissipation of heat into the substrate. We do this by employing a meander. With the limitation of confining each resistor into a single EBL 100 µm ×100 µm write-field, we have used a Matlab algorithm to generate meander paths for resistive values within specified ranges. We have selected benchmarks of 100 kΩ and 300 kΩ resistive structures for our circuit, both of which should generate Q factors which will fulfil the required values discussed in Section 7.3.4.

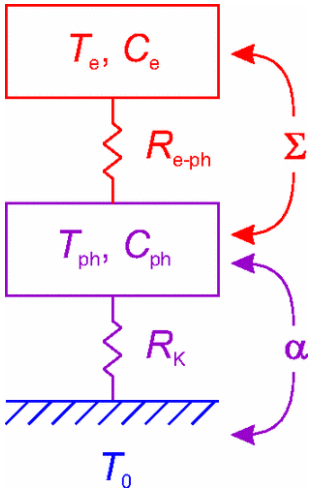

Figure 7.5: Illustration of the lumped element model for resistive heating as developed in Webster *et al.* [62].

7.4.2 Estimating resistor heating

Webster *et al.* [62] present a model for estimating circuit heating by resistors using a lumped element model shown in Figure 7.5 adapted from an earlier work by Roukes [133]. An in-depth treatment of the model may be found in the original paper. Here we give a summary.

In the illustration, $\mathrm{T_e}$ and $\mathrm{T_{ph}}$ represent electron and phonon temperatures. The electronic and phonon heat capacities are represented by C_e and C_ph. R_{e-ph} is the thermal resistance of the heat transfer between the electron sea and the lattice whilst R_K is the Kapitsa thermal boundary resistance between the resistor material lattice and the substrate. Σ and α represent the electron-phonon and resistor-substrate coupling constants respectively.

For the purposes of this section we consider the dependency of electron temperature on the I^2R dissipative power as a result of resistor heating, as given by the model. For a resistive structure with a resistance R, driven at a current I, this dependency is

$$T_\mathrm{e}^5 = T_\mathrm{ph}^5 + \frac{I^2 R}{\Sigma\Omega} \tag{7.7}$$

where Ω is the volume of the resistor. The phonon temperature T_{ph} is dependent on the substrate temperature T_0 and is given by

$$T_{\mathrm{ph}}^4 = T_0^4 + \frac{I^2 R}{\alpha A} \tag{7.8}$$

where A is surface area of the resistor. As can be see from both equations the inverse dependence on the resistor volume Ω and resistor surface area A (through the phonon temperature T_{ph}) should allow for reduction of the overall electron temperature if the area of substrate covered by the resistor is increased. Using the surface area and volume of the meander resistors from our design we have used these equations to predict the resistive heating within our circuits.

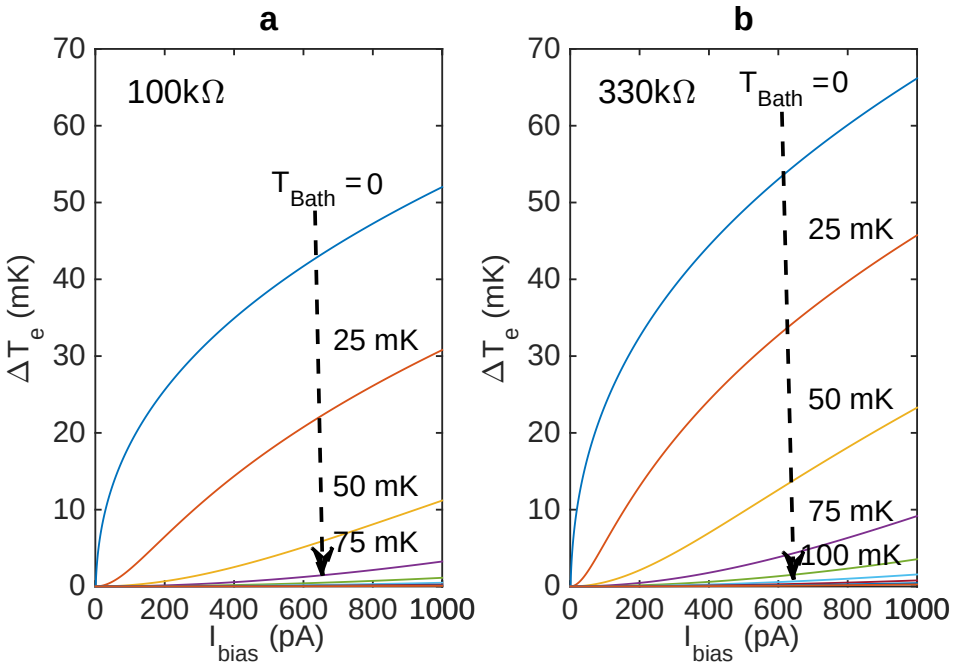

Figure 7.6: Modelled electron variation of temperature in **a.** 100 kΩ and **b.** 330 kΩ meander resistor structures designed to fit in a 100 µm ×100 µm write-field area. ΔT_{e} is given by $T_{\mathrm{e}}(I_{\mathrm{bias}}) - T_{\mathrm{e}}(0)$. The model used is based on a lumped element model adapted to this resistor design from [62]. The gradated plots correspond to different bath temperatures in the circuit for zero current bias. The vertical dashed arrows indicate the increase in bath temperature.

Figure 7.6**a.** and **b.** show the predicted change to electron temperatures for

100 kΩ and 330 kΩ meander resistors respectively. The results are based on the resistor area and volume for CrO_x meander resistors of thickness 100nm with a sheet resistance 0.92 kΩ/□. The CrO_x sheet resistance was taken from measurements on thin-film bar structures of CrO_x deposited according to the recipe we present in [17]. Webster *et al.* predict the appearance of the first two QPS dual-Shapiro steps within the pA range [62].

From the modelled plots, it appears that any contribution to the electron temperature is in the low mK range, becoming negligible as the bath temperature reaches 75 mK. Assuming a measurement temperature of 25-30 mK the simulated contributions to the electron temperature are in the range 30-45 mK at maximum bias current, depending on the resistor selected.

However, even this may be minimised if the cooling power of the equipment is taken into account. If we consider heating as the full power dissipated by the resistors, the I^2R values for these resistances for as high as 200 nA driving current is 4 nW and 13.2 nW respectively for a 100 kΩ and a 330 kΩ resistor. The cooling power of the dilution refrigerator in which we measured our prototype is 240 mW at 100 mK. This value is well in excess of these two estimates.

7.4.3 Chip design

Our prototype circuit follows the voltage biased QPS circuit design proposed by Mooij and Nazarov. The circuit is intended for characterisation using filtered dc lines in a 4-point measurement arrangement. For our design we placed a series resistance on each line, along with an inductor line either side of the nanowire element. This symmetrical layout was implemented to facilitate ac measurement of the circuit, should it be required. In comparison to the circuit used in [62], our initial circuit will not incorporate an RF line connection through an interdigitated capacitor in order to limit complexity in the first instance. Instead, we will be using a radial and loop antenna set up to irradiate the sample once a critical voltage feature is confirmed. This omission allows for a more compact design and more space for multiple devices in order to increase yield.

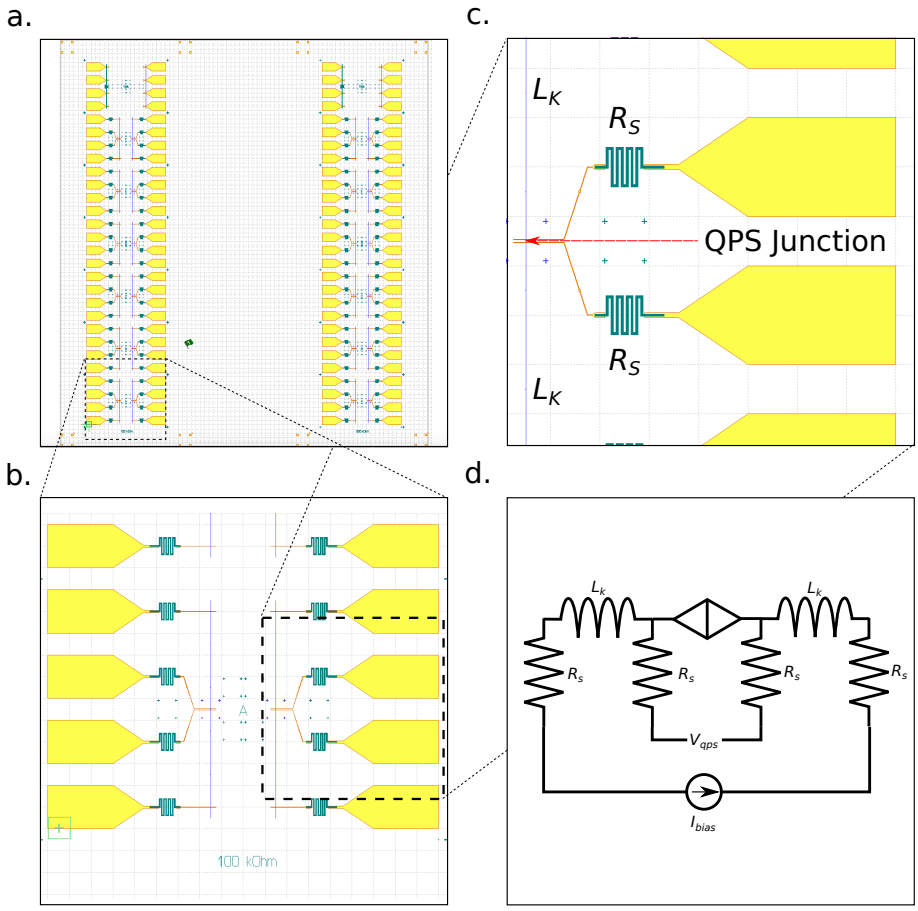

Figure 7.7: GDSII Layout of the QPS chip prototype design in **a** with zoom of single pair of devices in **b.**. Au is represented in yellow, CrO_x in dark grey and the NbN inductor line is shown in blue. **c.** shows the equivalent circuit to the device.

Figure 7.7 shows the chip design that was settled on. The pattern, designed to fit on a 10 mm×10 mm substrate die comprises two sets of two columns of devices. The left set incorporates devices with resistors of R_s =100 kΩ on each contact whilst the right set incorporates the same circuit design with R_s =330 kΩ. The columns contain 12 devices each. Each device comprises four Au contact pads that connect to a 100 nm wide, 900 µm long NbN inductor line through the CrO_x meander resistors. The inductor line itself incorporates 10 µm × 10 µm pads at the boundary of each EBL write field to avoid exposure breaks at the stitching boundary. This is explained in more detail in Chapter 3. The central contact pads connect to a smaller central region of the inductor line, within which a masked dry etch will is used to reduce the inductor line to a 1 µm long nanowire of the desired width.

7.5 Prototype

7.5.1 The first fabricated chip

Figure 7.8 shows an SEM image of one of the devices fabricated according to the design in Figure 7.7. The prototypes were fabricated on a p-type silicon substrate die of 10 mm× 10 mm dimensions without deliberate oxidation of the surface before deposition.

For the prototypes, all lithography was done using EBL techniques, as detailed in Chapter 3. To minimise contamination of the NbN material through processing, the CrO_x resistors were deposited first using a lift-off mask. The NbN inductor line is then deposited through a PMMA lift-off mask before a Au cap layer is used to deposit the connector pads and interconnect wires. A ten second Ar^+ plasma ash was found to be necessary before each deposition in order to reduce the formation of poor material boundaries and resulting high contact resistance.

After deposition of the interconnects, the inductor line was reduced to nanowire dimensions using a Ne beam on a Carl Zeiss Orion Nanofab Helium Ion Microscope and FIB system. This was done with the help of Dr James Sagar, who kindly

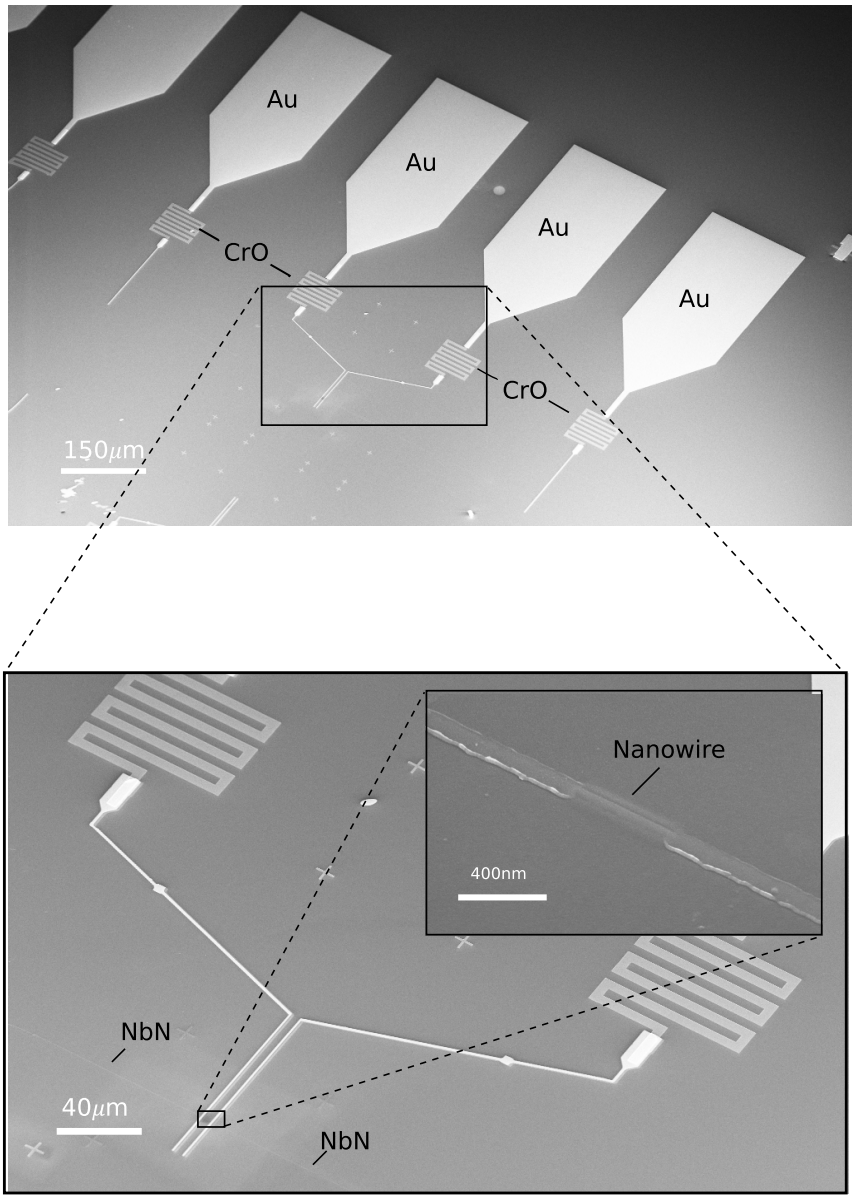

Figure 7.8: SEM image of a device on one of the prototype samples with higher magnification of the inductor and nanowire regions. The inset shows the region of the inductor line reduced to a nanowire using a Ne focussed ion beam.

performed the delicate final etching step. An SEM image of one of the etched nanowires is shown in the inset of Figure 7.8.

7.5.2 Measurement and considerations

Measurement stages

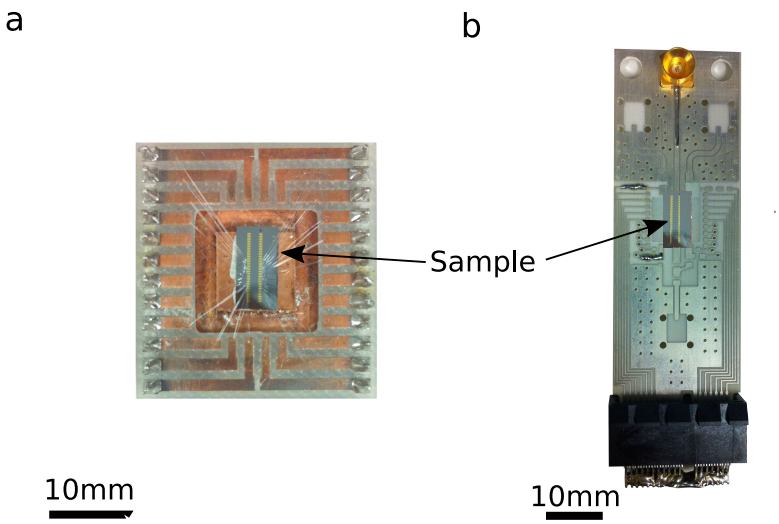

Figure 7.9: QPS chip samples as mounted on sample mounts for initial wet measurement **a** and later for measurement in the dilution refrigerator **b**.

Successfully fabricated samples were first measured for connectivity in liquid helium at 4.2 K. The first fully connected prototype was then taken for measurement in an Oxford Instruments Triton 200 cryogen-free dilution refrigerator, a model capable of base temperatures of 30 mK. Measurement time on the refrigerator was kindly provided by Prof. John Morton and the measurements were made with the help of Dr Jonathan Burnett and Dr Matias Urdampilleta, both colleagues at the London Centre for Nanotechnology.

The prototype contained four devices confirmed to be connected, corresponding to positions A, C, D and E. The widths of the nanowires in each of these devices measured 25 nm, 43 nm, 35 nm and 20 nm respectively. Each was connected through a 100 kΩ CrO_x resistor on each contact line.

In the dilution refrigerator these devices were measured via dedicated DC lines.

In order to reduce measurement noise and propagation of noise down the lines and to the sample, attenuators are used at each stage of the refrigerator leading down to the mixing plate. The lines themselves are clad in conductive foam used to further reduce noise. Within the sample puck, the lines are fed through Cu powder filters and a final RC low-pass filter before being connected to the sample mount and the sample itself.

Measurement setup and complications

Early in the measurements on the DR, characterisation of the CrO_x resistors revealed resistances in the MΩ range at 30 mK, considerably higher than had originally predicted[1]. The long voltage settling time in the circuit response to current biasing meant that the implementation of any lock-in measurement techniques could not be used. A Yokogawa GS200 DC voltage/current source was used to source current to samples whilst a Keithley 2400 Source Meter was used to measure the voltage across the sample after amplification through a Stanford Research SR560m Voltage Amplifier. National Instruments Labview was used to control the individual modules during the measurements whilst also logging the data.

Early measurement data noted a periodic current feature in the sweeps. Subsequent testing of the circuit of the individual equipment modules revealed the Yokogawa current source was generating 4 mV voltage spikes at intervals of 10 nA. The module was replaced and further measurements were executed using a Keithey 6220 Precision Current Source.

The measurements themselves required large idle periods to allow the device to settle for each bias current. Since sampling was employed to minimise noise in the measurements, the measurement for each datapoint would take between five and fifteen minutes depending on how fast the device would settle. The Labview

[1]The CrO_x resistor material was characterised extensively as part of our work in [17]. However, this work did not cover the effects of subsequent annealing of the material. We believe that the repeated baking of the material during fabrication of subsequent layers may have increased the oxygen content in the CrO_x. Small increases in the O/Cr ratio were shown to increase the resistance of the material by orders of magnitude by Nash *et al.* [17]. Such a mechanism would support the increase observed here

script was set up to observe when the sampled data had reached a tolerance of 4% variation before taking the datapoint as an average. Each data point taken for a plot represents the settled average of 200 measurements. As such current-voltage sweep took between one and ten hours to acquire, depending on the resolution and the number of data points taken.

7.5.3 $I-V$ Characteristic of 25 nm wide QPS nanowire device at 30mK

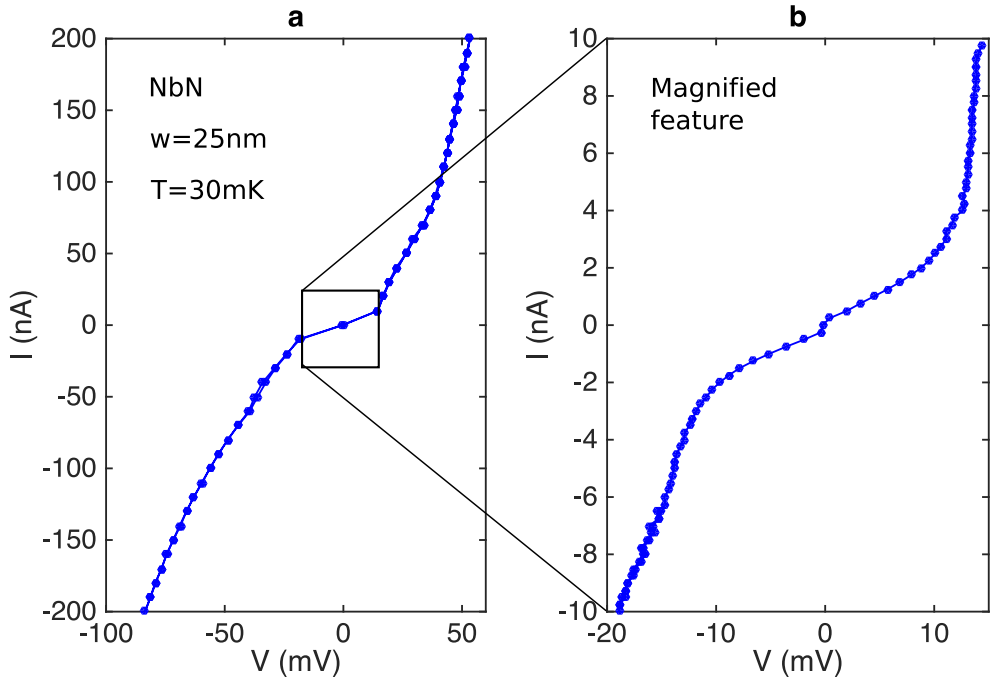

Figure 7.10: $I-V$ characteristic of QPS device C at 30 mK. The device was centred on a NbN nanowire less than 25 nm in width. Plot **a.** shows a coarser scan across a broader current range whilst **b.** was a finer resolution overnight run across the central current range.

Figure 7.10 shows the $I-V$ characteristics of device C, corresponding to a device with a nanowire 45nm wide by 1µm long. Plot **a.** shows a coarse sweep of the sample through a relatively wide current range. An asymmetry to the behaviour is observable. We attribute this to settling of the circuit over time. Given the long measurement time for each point and the high series resistance, it is believable

that the characteristic would drift over long measurements. An interesting feature appears present between -25 mV and 25 mV. At such large current measurement step values, the resolution of the sweep here could disguise a feature in the central region. The $I - V$ range of the feature is so small that higher resolution were required. One of the later overnight measurements on the sample is displayed in plot **b.**, showing the sample across a finer range of bias current values with a more clearly defined change in the $I - V$ characteristic.

At this stage we believe that the feature observed could be a sign of a QPS critical voltage, however this is difficult to confirm without further measurements. The $I - V$ does exhibit a genuine characteristic for a finite voltage range of the order of millivolts as observed by Webster *et al.* [62] and predicted by Mooij and Nazarov [3]. Approximating this value to 12 mV from plot **b.**, this generates a frequency corresponding to E_S of approximately 1 THz, a value comparitively large to the 1-10 kHz cited for Giordano by Zaikin *et al.* [50], albeit a range given for wires from a different material. However, the arguments against would be that these observations and predictions were made for Nb_xSi_{1-x}, not NbN and that a perfect zero-current state is not truly observed here.

The long settling time of the circuit prevented further characterisation of the cicuit, including its' temperature dependence behaviour. Although this could have been investigated across a small range using the dilution refridgerator, further measurements on this device were unfortunately prevented when the devices failed following a power outage during measurement of the sample. Subsequent measurements could not confirm connection to any of the devices.

7.6 Conclusion

In this chapter we have considered the dependencies of QPS parameters on the physical attributes of the superconducting material from which they are fabricated. We have then used values extracted from our measurements on 2D films to estimate these dependencies for QPS circuits we might fabricate using these materials and

used the results to select the benchmark values for series resistance and inductor widths that should optimise the circuits for the observation of QPS phenomena. We have also used the results of the simulations in our selection of the superconducting material for use in our prototype circuit.

We developed a solution to the heating issues faced in prior attempts [62] by maximising the surface area of the resistors used for the circuit. We did this by designing and implementing meander resistors generated using a script to fit our requirements. Using parameters from our previous measurements on CrO_x we were able to use the same lumped element model used by Webster *et al.* to model heating in our modified resistor design and demonstrate that the use of meander structures for resistors should minimise any contribution to circuit heating to a negligible level.

Based on the results of the modelled systems, we were able to select benchmark parameters and designed a new prototype chip comprising 24 QPS circuit devices. These chips were fabricated with one prototype sample confirmed measurable. This sample was subsequently measured in a dilution refrigerator at 30 mK and found to exhibit an $I - V$ characteristic that could indicate the presence of a critical voltage feature. The devices on the sample unfortunately failed before further measurements could be made.

In the final chapter, we present the conclusions drawn from our analysis and discuss areas of further work whose relevance to the field has been identified during our investigations.

Chapter 8

Conclusion & Future Work

8.1 Conclusions

The observation of QPS presented itself to be a formidable challenge to the research community across the last 20 years. There was a seven year gap between the prediction of the Mooij-Harmans qubit [58] and the direct observation of coherent quantum phase slips in a physical realisation of the device was reported [5]. Over this time, it has become increasingly clear that disordered systems where superconductivity is considerably weakened close to the point of the SIT are favourable environments for observation of QPS phenomena [84, 5]. The high resistivity of such materials are believed to enhance their characteristic rate of QPS [11].

Previous works have often relied on existing experimental data to estimate characteristic superconducting parameters for materials in their experiments. Whilst this is often necessary due to time constraints or limitations in resources, small variations in fabrication can manifest as distinct deviations from literature reported values, particularly as dimensions are reduced. We argue a necessity in the careful identification of key characteristics of superconducting materials in order to better understand these systems. Confirming these characteristics not only allows for greater reproducibility of results but also for more accurate predictions of their

behaviour as environments in which quantum effects may be observed.

During the course of this thesis we have documented the interplay between disorder and dimension in two superconductors of particular interest to the investigation of QPS phenomena. We have not only provided measures of this disorder in our compositions of Nb_xSi_{1-x} and NbN, but we have demonstrated the dependence of T_c and $R_\square$ on disorder as dimensions are scaled down.

This has allowed us to provide a clearer understanding of how superconductivity will change for these materials as they are scaled down in dimension. For two-dimensional films we have investigated the relationship between T_c and $R_\square$ and made clear estimations of the Ginzburg-Landau coherence length and the mean free path using our analysis. We have shown an inverse proportionality between T_c and the sample thickness, observable for both Nb_xSi_{1-x} and NbN. We have used this analysis to predict the critical film thickness, the point at which the film thickness is believed to be comparable to the mean free path. It is at this dimension where an SIT is expected to occur.

However, the predicted dual to the Josephson junction and the system in which QPS are observable is a nanowire. Thus we proceeded to investigate if the relationship between dimension and disorder may be observed in the one-dimensional regime. In order to investigate this, a reliable nanowire fabrication technique was required.

As we saw, whilst many novel, non-lithographic techniques have been employed in the fabrication of superconducting nanowires, these often result in a wide range of lengths and cross-sectional morphologies which can complicate the analysis of transport measurements. For lithographic techniques that traditionally rely on EBL lift-off, the minimum exposure width will determine the minimum achievable wire width. The exposure is dependent not only on the physical beam diameter at the point of exposure, but also factors such as the age of the resist, mechanical vibrations during exposure and the amount of scatter both in the resist and the film. All of these can serve to broaden exposures and the final wires. We developed

and presented an innovative solution to this problem by inverting the process and creating a stencil etch technique. By defining the edges of the nanowire rather than the nanowire itself, we demonstrated that any of the aforementioned factors only serve to reduce the final width rather than increase it, pushing the wire further into the limit of the QPS regime.

We employed our technique to fabricate nanowires from both $Nb_{0.3}Si_{0.7}$ and NbN films. These were nominally 1μm in length in a range of widths for the purposes of our investigation. We characterised their behaviour at low temperatures and demonstrated that the disorder related dependence of T_c on dimension could be observed for width in both of these materials, with T_c inversely proportional to the width. To our knowledge, the only previous observation of such a relationship in superconducting nanowires was a dependence on w^{-2}[82]. The authors argued the power of two dependence indicated their samples were still in a two dimensional-limit. Accordingly, our observations suggest that our samples in both materials are within the one-dimensional limit.

In addition, this result also allows the identification of the critical width dimension. As with the critical film thickness, this length can be used as an indicator of the mean free path and the dimension at which we may expect to see an SIT. Tuning wires of these materials within range of these dimensions will increase the level of disorder and should increase the rate of QPS occurrence.

As the dimensions of wires were reduced, a residual resistance plateau could be observed for some of the smaller wires. A study of one of these samples in a dilution refrigerator revealed that the highly resistive nature of narrower wires resulted in a susceptibility to current noise. We used room temperature RC filtering to attenuate the noise and show that superconductivity could be restored in these samples. Through the study we demonstrated the importance of well filtered measurement environments and the effect of noise in the characterisation of nanowires.

We proceeded to use the characteristics obtained from our investigations along

with existing QPS theory to make predictions of how these materials will behave in a QPS system. According to our predictions, we presented our argument in favour of the use of NbN and proceeded to design and fabricate a prototype QPS circuit based on our calculations. We presented measurement data made on this device, the first of its kind for this experiment in several years. A promising feature in the voltage was observed, but without characterisation in further detail, it remains inconclusive if this was truly a critical voltage pointing to QPS.

8.2 Future Work

Over the course of our investigations we have noted several factors that offer opportunity for further understanding in the field as well as opening avenues into related areas of study. We divide these into two primary sections based on our investigations, thin films and nanowires.

8.2.1 Further investigations in thin-films

Investigation of process parameters on the tuning disorder in superconducting thin films.

In the development of our thin film superconductors we have observed variation in the behaviour of our films that can be tuned not only with the material composition but also by the fabrication process and parameters itself. In Chapter 4 we have identified deviations in the transition temperature of our sputtered Nb_xSi_{1-x} films in comparison to trends reported for films fabricated using co-evaporation techniques. In Chapter 4, Figure 4.8 illustrates such deviations in a comparison of conductivity and transition temperatures between our co-sputtered $Nb_{0.3}Si_{0.7}$ and values in co-evaporated films of Nb_xSi_{1-x}. The data for the co-sputtered films shows a clear deviation from the trends in both parameters, as indicated by the solid red and blue fit lines.

The size of the grains that form a superconducting film is heavily affected by process type and parameters. We do not propose to change our deposition method but do believe that grain size is a determining factor in the behaviour of the final

film. This is particularly important since grain boundaries are characteristically defects in the material. As such, process type and process parameter selection can affect the level of disorder exhibited. We recommend an investigation into the impact of process parameters on film grain size and ultimately the $R_{\square}$ and T_{c} characteristics of the material. Tuning beam energy and the chamber pressures in a sputtering process will allow a degree of control over the energy of the sputtered atoms arriving at the surface of the substrate. By quantifying this relationship more carefully in our process it should be possible to tune disorder and the resulting film behaviour.

8.2.2 Further investigation in nanowires

During the fabrication and measurement of superconducting nanowires in both $\mathrm{Nb}_x\mathrm{Si}_{1-x}$ and NbN, one of the main challenges identified is the control and limitation of the impact of local material inhomogeneity on nanowire samples. This impact manifests in variation of behavioural characteristics between nanowire samples fabricated from single films that complicates characterisation and analysis. To some degree, the use of error bars and fitting algorithms can reduce this impact but it will remain a factor inherent to nanowires created using top down fabrication.

In this subsection we propose two devices that would improve measurement flexibility in the characterisation of dimensional effects in superconducting nanowires whilst reducing the impact of variation between samples due to local material variations. The first device focusses on characterising the dependence of nanowire behaviour and superconductivity on nanowire length and may be directly applied to our existing stencil method. The second device proposes the use of a gate induced field to tune the conduction path rather than physically reduce its dimensions, to enable more controlled investigations of the reduction of channel cross-section and disorder.

Dependence of disorder on length in superconducting nanowires

As was introduced in Equation 7.1, the rate of QPS phenonema in a nanowire is directly proportional to the length and inversely proportional to the width and thickness of the wire. This inverse proportionality on cross-sectional dimensions provided significant motivation in the focus of our investigations on disorder as superconductors are reduced in width and thickness. However the dependence of disorder and a demonstration of this proportionality on the third dimension, that of nanowire length, was not investigated.

Work by Lau *et al.* [52] has investigated the variation in the temperature dependence of resistance versus length in 100 nm-1 μm long MoGe nanowires prepared using the carbon nanotube scaffold fabrication technique developed by Bezryadin *et al.* [13]. Lau *et al.* describe the behaviour of resistance normalised to sample length using the LAMH and MQT theoretical models. A similar dependence was later investigated in longer nanowires ranging between 1-100 μm in pure Nb by Xu and Heath [134]. Given the length of these devices, this work represents one of the best examples of uniformity in superconducting nanowires, with samples reportedly atomically straight, down to widths of 10 nm. Here the authors are able to describe much of the low temperature resistive behaviour in their samples using the TAPS model alongside QPS models adapted from works from Giordano and Lau [45, 52].

These existing studies present a good insight to the behaviour of nanowires of different lengths, but a fundamental issue that is not addressed is material variation between samples. Even where nanowires have been fabricated from the same thin film or in the same deposition step, we may expect small variations in material disorder that may result in changes in the low temperature transport behaviour for nanowire dimensions.

In order to overcome this ambiguity we propose a uncomplicated device based on a single long ($\sim 50\,\mu$m) superconducting nanowire, illustrated in Figure 8.1. By applying connection taps at several points along the wire, the same wire may be measured at different length-scales depending on what connections are selected.

Any un-used taps may be left as electrical floating points to limit their influence on the current path during measurement. Figure 8.1 **b.** illustrates how such a design could be easily applied using our current nanowire stencil-etch method.

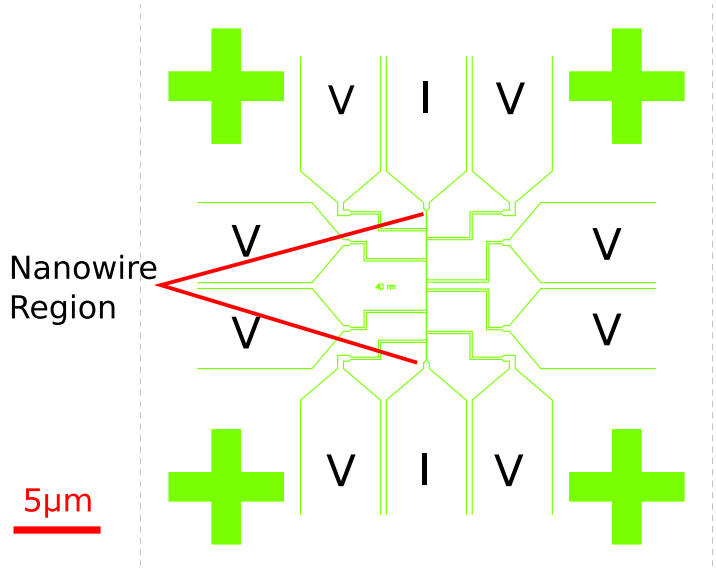

Figure 8.1: Etch pattern for the the proposed extended-path device for the investigation of length effects on superconducting nanowire behaviour. The pattern is ready for use with the existing stencil etch technique.

Field-tuned QPS nanowire conduction channels

In Chapter 2 we discussed an elegant technique by Zgisrki *et al.* [12, 54] for Ar milling of nanowire structures allowing the measurement of the same sample at successively reduced cross-sectional dimensions. Such a reduction technique provides an attractive option in controlling the variation between successive measurements in size related effects. However, ion milling is a physical sputtering technique. Although superconductivity is widely considered to be unaffected by Ar, due to the elements' inert nature, Ar ion beam techniques do cause structural alterations to samples, preferentially thinning amorphous material over crystalline [135], and inducing the formation of silicides through the intermixing of Si substrate atoms for higher beam energies [136]. In the one dimensional regime, such alterations will have result in more significant variations to the behaviour of samples.

We propose the use of a superconducting nanowire field effect device as a solution for this challenge. The incorporation of a gate to create a field-effect tuneable nanowire transistor nanowire device will allow the user to tune the dimensions of the conduction channel without any change to the material structure, disorder or composition. Investigations into gate-tuned superconducting nanowire channels have already been demonstrated, most comparably in the QPS single-charge transistor by Hongisto *et al.* [59], and in topological superconductors, using superconducting banks to proximitise semiconductor nanowires [137]. However, none have reported on the use of such a device in the investigation of disorder in reduced dimensions.

Figure 8.2 illustrates three potential gate configurations for such a device. In **a.**, the application of a field using a top-gate configuration should provide the most uniform reduction of the conduction channel given the morphology of the gate. From a fabrication perspective, this method presents the least complexity to implement using an EBL step to define the gate path and connection pad and subsequent deposition of a SiN dielectric and normal metal or superconductor gate material. However, given the nanoscale dimensions of the superconducting wire, should the configuration result in complications due to the proximity effects, configurations **b.** and **c.** propose the use of a back-gate or capacitively coupled parallel gate configurations respectively, each of which should eliminate any proximitisation of the nanowire by the dielectric or the gate materials.

The added virtue of such a device is that, much like our stencilling method, it represents a side-step workaround to limitations in the fabrication of ultra-narrow nanowires. With the Ginzburg-Landau coherence lengths in our films reported to ranges of 2-16 nm in Chapter 4 and measurements indicating coherence lengths of between 8-14 nm in nanowires from the same films in Chapter 6, the onus on ever smaller dimensions and uniformity of samples increases. Provided a uniform field characteristic is achieved, a field controlled conduction channel could offer uniform reduction but also eliminate the requirement for ultra-narrow nanowire fabrication.

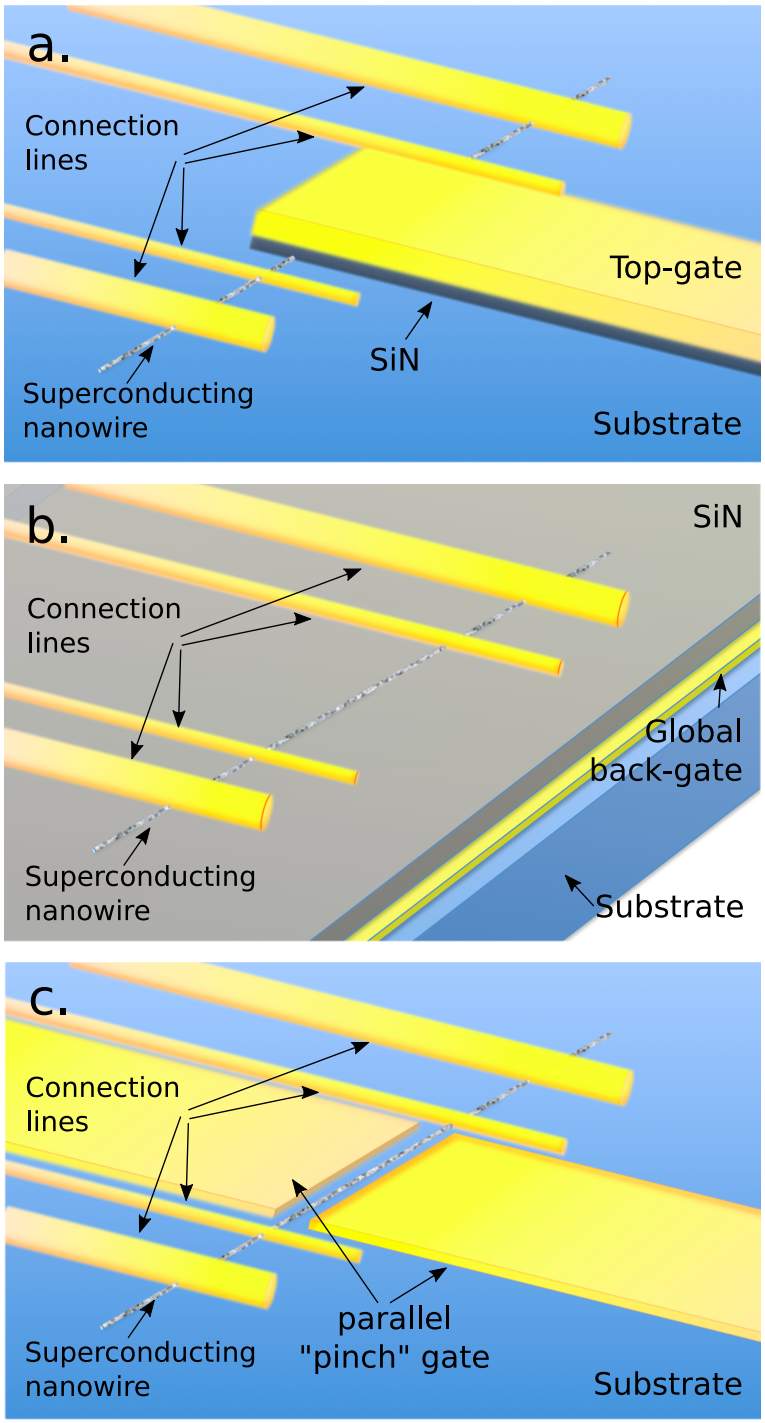

Figure 8.2: Illustration showing the three potential gate configurations of a field effect device for the investigation of dimensional effects and disorder in nanowires. **a.** corresponds to a top-gate configuration whilst **b.** illustrates a global back gate design. **c.** shows a parallel "pinch" gate configuration.

Such devices could allow the investigation of narrower conduction channels from larger nanowires at cross-sectional dimensions that are less complicated to fabricate.

Bibliography

[1] K. M. Rosfjord et al. "Nanowire Single-photon detector with an integrated optical cavity and anti-reflection coating". *Appl. Phys. Lett. Appl. Supercond. Phys. Rev. A OSA Appl. Supercond. IEEE Trans. Appl. Supercond*, **79**, 15, 626–630, 2001.

[2] S. Miki et al. "Large sensitive-area NbN nanowire superconducting single-photon detectors fabricated on single-crystal MgO substrates". *Appl. Phys. Lett.*, **92**, 6, 2008.

[3] J. E. Mooij and Y. V. Nazarov. "Superconducting nanowires as quantum phase-slip junctions". *Nat. Phys.*, **2**, 169–172, 2006.

[4] C. Cirillo et al. "Superconducting nanowire quantum interference device based on Nb ultrathin films deposited on self-assembled porous Si templates". *Nanotechnology*, **25**, 42, 425205, 2014.

[5] O. V. Astafiev et al. "Coherent quantum phase slip". *Nature*, **484**, 7394, 355–358, 2012.

[6] A. M. Finkel'stein. "Superconducting transition temperature in amorphous films". *JETP Lett.*, **45**, 1, 46–49, 1987.

[7] M. P. A. Fisher. "Quantum Phase Transitions in Disordered Two-Dimensional Superconductors". *Phys. Rev. Lett.*, **65**, 7, 923–927, 1990.

[8] A. M. Finkel'stein. "Suppression of superconductivity in homogeneously disordered systems". *Phys. B Condens. Matter*, **197**, 1-4, 636–648, 1994.

[9] D. B. Haviland, Y. Liu and a. M. Goldman. "Onset of superconductivity in the two-dimensional limit". *Phys. Rev. Lett.*, **62**, 18, 2180–2183, 1989.

[10] Y. Ivry et al. "Universal scaling of the critical temperature for thin films near the superconducting-to-insulating transition". *Phys. Rev. B*, **90**, 21, 214515, 2014.

[11] K. Y. Arutyunov, D. Golubev and A. Zaikin. "Superconductivity in one dimension". *Phys. Rep.*, **464**, 1-2, 1–70, 2008.

[12] M. Zgirski, K.-P. Riikonen, V. Touboltsev and K. Arutyunov. "Size dependent breakdown of superconductivity in ultranarrow nanowires." *Nano Lett.*, **5**, 6, 1029–33, 2005.

[13] A. Bezryadin, C. Lau and M. Tinkham. "Quantum suppression of superconductivity in ultrathin nanowires". *Nature*, **404**, 6781, 971–4, 2000.

[14] W. Li, J. C. Fenton, C. Gu and P. A. Warburton. "Superconductivity of ultra-fine tungsten nanowires grown by focused-ion-beam direct-writing". *Microelectron. Eng.*, **88**, 8, 2636–2638, 2011.

[15] W. Ning et al. "Superconductor–Insulator Transition in Quasi-One-Dimensional Single-Crystal Nb 2 PdS 5 Nanowires". *Nano Lett.*, **15**, 2, 869–875, 2015.

[16] J. T. Peltonen et al. "Coherent flux tunneling through NbN nanowires". *Phys. Rev. B*, **88**, 1–5, 2013.

[17] C. R. Nash, J. C. Fenton, N. G. N. Constantino and P. A. Warburton. "Compact chromium oxide thin film resistors for use in nanoscale quantum circuits". *J. Appl. Phys.*, **116**, 224501, 2014.

[18] H. K. Onnes. "Further experiments with liquid helium D - On the change of the electrical resistance of pure metals at very low temperatures, etc V The disappearance of the resistance of mercury". *K. Ned. Akad. van Wet.*, **14**, 113–115, 1911.

[19] W. Meissner and R. Ochsenfeld. "Ein neuer Effekt bei Eintritt der Supraleitfahigkeit". *Naturwissenschaften*, **21**, 44, 787–788, 1933.

[20] F. London and H. London. "The Electromagnetic Equations of the Supraconductor". *Proc. R. Soc. A Math. Phys. Eng. Sci.*, **149**, 866, 71–88, 1935.

[21] V. Ginzburg and L. Landau. "On the theory of superconductivity". *Zh. Eksp. Teor. Fiz.*, **20**, 1064–1082, 1950.

[22] L. Gor'kov. "Microscopic derivation of the Ginzburg-Landau equations in the theory of superconductivity", 1959.

[23] W. Keesom and A. Keesom. "New measurements on the specific heat of liquid helium". *Physica*, **2**, 1-12, 557–572, 1935.

[24] L. Landau. "The Theory of Phase Transitions". *Nature*, **138**, 3498, 840–841, 1936.

[25] M. Tinkham. *Introduction to Superconductivity.* Dover Publications, 2nd edition, 1996.

[26] J. Bardeen, L. N. Cooper and J. R. Schrieffer. "Theory of Superconductivity". *Phys. Rev.*, 1957.

[27] H. Frohlich. "Interaction of Electrons with Lattice Vibrations". *Proc. R. Soc. A Math. Phys. Eng. Sci.*, **215**, 1122, 291–298, 1952.

[28] T. Van Duzer and C. W. Turner. *Principles of Superconductive Devices and Circuits.* Prentice Hall, 2nd edition, 1998.

[29] A. B. Pippard. "An Experimental and Theoretical Study of the Relation between Magnetic Field and Current in a Superconductor". *Proc. R. Soc. A Math. Phys. Eng. Sci.*, **216**, 1127, 547–568, 1953.

[30] D. R. Tilley and J. Tilley. *Superfluidity and Superconductivity.* IOP Publishing, Bristol, 3rd editio edition, 1990.

[31] D. Shoenberg. "Superconducting Colloidal Mercury". *Nature*, **143**, 3619, 434–435, 1939.

[32] J. N. Rjabinin and L. W. Shubnikow. "Magnetic Properties and Critical Currents of Supra-conducting Alloys". *Nature*, **135**, 3415, 581–582, 1935.

[33] A. A. Abrikosov. "On the Magnetic Properties of Superconductors of the Second Group.pdf". *Sov. Phys. JETP*, **5**, 6, 1174–1183, 1957.

[34] P. W. Anderson and J. M. Rowell. "Probable observation of the superconducting Josephson tunneling effect.pdf". *Phys. Rev. Lett.*, **10**, 6, 230–232, 1963.

[35] C. P. Poole Jr, H. A. Farach and R. J. Creswick. *Superconductivity.* Academic Press Limited, first edition, 1995.

[36] I. S. Grant and W. R. Phillips. *Electromagnetism.* John Wiley & Sons Ltd, second edi edition, 1990.

[37] C. Hamilton, R. Kautz, R. Steiner and F. Lloyd. "A practical Josephson voltage standard at 1 V". *IEEE Electron Device Lett.*, **6**, 12, 623–625, 1985.

[38] W. C. Stewart. "Current-voltage characteristics of Josephson junctions". *Appl. Phys. Lett.*, **12**, 8, 277–280, 1968.

[39] D. E. McCumber. "Effect of ac impedance on dc voltage-current characteristics of superconductor weak-link junctions". *J. Appl. Phys.*, **39**, 7, 3113–3118, 1968.

[40] W. Little. "Decay of persistent currents in small superconductors". *Phys. Rev.*, **156**, 2, 396–403, 1967.

[41] N. D. Mermin and H. Wagner. "Absence of ferromagnetism or antiferromagnetism in one or two dimensional isotropic heisenberg models". *Dalton Transactions*, **17**, 3715–22, 1966.

[42] J. Langer and V. Ambegaokar. "Intrinsic resistive transition in narrow superconducting channels". *Phys. Rev.*, **164**, 2, 498–510, 1967.

[43] S. E. Lyshevski. *Dekker Encyclopedia of Nanoscience and Nanotechnology.* CRC Press, Cambridge, third edition, 2014.

[44] B. Josephson. "Possible new effects in superconductive tunnelling". *Phys. Lett.*, **1**, July, 251–253, 1962.

[45] N. Giordano. "Evidence for Macroscopic Quantum Tunneling in One-Dimensional Superconductors", 1988.

[46] R. D. Parks and R. P. Groff. "Evidence for Thermodynamic Fluctuations in a Superconductor". *Phys. Rev. Lett.*, **18**, 10, 1–4, 1967.

[47] J. E. Lukens, R. J. Warburton and W. W. Webb. "Onset of quantized thermal fluctuations in "one-dimensional" superconductors". *Phys. Rev. Lett.*, **25**, 1180–1184, 1970.

[48] D. Golubev and A. Zaikin. "Thermally activated phase slips in superconducting nanowires". *Phys. Rev. B*, **78**, 14, 1–8, 2008.

[49] A. J. Van Run, J. Romijin and J. E. Mooij. "Superconduction Phase Coherence in Very Weak Aluminium Strips.pdf". *J. Appl. Phys.*, 1987.

[50] A. Zaikin, D. Golubev, A. van Otterlo and G. Zimányi. "Quantum Phase Slips and Transport in Ultrathin Superconducting Wires". *Phys. Rev. Lett.*, **78**, 8, 1552–1555, 1997.

[51] G. Schön. "Superconducting nanowires". *Nature*, **404**, April, 948–949, 2000.

[52] C. Lau et al. "Quantum Phase Slips in Superconducting Nanowires". *Phys. Rev. Lett.*, **87**, 21, 19–22, 2001.

[53] M. Zgirski and K. Arutyunov. "Experimental limits of the observation of thermally activated phase-slip mechanism in superconducting nanowires". *Phys. Rev. B*, **75**, 17, 13–16, 2007.

[54] M. Zgirski et al. "Ion beam shaping and downsizing of nanostructures". *Nanotechnology*, **19**, 5, 055301, 2008.

[55] M.-H. Bae et al. "Current-phase relationship, thermal and quantum phase slips in superconducting nanowires made on a scaffold created using adhesive tape." *Nano Lett.*, **9**, 5, 1889–96, 2009.

[56] S. Khlebnikov. "Quantum phase slips in a confined geometry", 2008.

[57] D. Golubev and A. Zaikin. "Coulomb Interaction and Quantum Transport through a Coherent Scatterer". *Phys. Rev. Lett.*, **86**, 21, 4887–4890, 2001.

[58] J. E. Mooij and C. J. P. M. Harmans. "Phase-slip flux qubits". *New J. Phys.*, **7**, 2005.

[59] T. T. Hongisto and a. B. Zorin. "Single-charge transistor based on the charge-phase duality of a superconducting nanowire circuit". *Phys. Rev. Lett.*, **108**, 9, 1–5, 2012.

[60] K. Y. Arutyunov et al. "Quantum phase slip phenomenon in ultra-narrow superconducting nanorings." *Sci. Rep.*, **2**, 293, 2012.

[61] K. A. Matveev, A. I. Larkin and L. I. Glazman. "Persistent current in superconducting nanorings." *Phys. Rev. Lett.*, **89**, 9, 096802, 2002.

[62] C. H. Webster et al. "NbSi nanowire quantum phase-slip circuits: Dc supercurrent blockade, microwave measurements, and thermal analysis". *Phys. Rev. B*, **87**, 1–12, 2013.

[63] F. Altomare and A. M. Chang. *One-Dimensional Superconductivity in Nanowires*. Wiley-VCH Verlag GmbH & Co. KGaA, Weinheim, Germany, 2013.

[64] J. D. Plummer, M. D. Deal and P. B. Griffin. *Silicon VLSI Technology: Fundamentals, Pracice & Modelling*. Prentice Hall, New Jersey, first edition, 2000.

[65] P. Drude. "Zur Elektronentheorie der Metalle". *Ann. Phys.*, **306**, 3, 566–613, 1900.

[66] J. Singleton. *Band Theory and Electronic Properties of Solids*. Oxford University Press, Oxford, seventh edition, 2001.

[67] N. W. Ashcroft and D. N. Mermin. *Solid State Physics*. Harcour Inc., 1976.

[68] A. D. Lagendijk, B. Van Tiggelen and D. S. Wiersma. "Fifty years of Anderson localization". *Phys. Today*, **62**, 24–29, 2009.

[69] P. W. Anderson. "Absence of diffusion in certain random lattices". *Phys. Rev.*, **109**, 5, 1492–1505, 1958.

[70] P. A. Lee and T. V. Ramakrishnan. "Disordered electronic systems". *Rev. Mod. Phys.*, **57**, 2, 287–337, 1985.

[71] A. F. Ioffe and A. R. Regel. "Progress in Semiconductors". *Prog. Semicond.*, **4**, 237, 1960.

[72] P. Anderson. "Theory of dirty superconductors". *J. Phys. Chem. Solids*, **11**, 1-2, 26–30, 1959.

[73] B. T. Matthias, H. Suhl and E. Corenzwit. "Ferromagnetic Superconductors". *Phys. Rev. Lett.*, **1**, 12, 449–450, 1958.

[74] S. Maekawa and H. Fukuyama. "Localization Effects in Two-Dimensional Superconductors". *J. Phys. Soc. Japan*, **51**, 5, 1380–1385, 1981.

[75] S. Maekawa, H. Ebisawa and H. Fukuyama. "Upper critical field in two-dimensions superconductors". *J. Phys. Soc. Japan*, **52**, 4, 1352–1360, 1983.

[76] D. Sherman et al. "Effect of Coulomb interactions on the disorder-driven superconductor- insulator transition". *Phys. Rev. B - Condens. Matter Mater. Phys.*, **89**, 3, 1–7, 2014.

[77] C. Delacour et al. “Persistence of superconductivity in niobium ultrathin films grown on R-plane sapphire”. *Phys. Rev. B - Condens. Matter Mater. Phys.*, **83**, 1–8, 2011.

[78] O. Crauste et al. “Thickness dependence of the superconductivity in thin disordered NbSi films”. In “J. Phys. Conf. Ser.”, volume 150, page 042019. 2009.

[79] O. Crauste et al. “Destruction of superconductivity in disordered materials : a dimensional crossover”. *Phys. Rev. B*, **060203**, 90, 1–5, 2014.

[80] N. Hadacek, M. Sanquer and J.-C. Villégier. “Double reentrant superconductor-insulator transition in thin TiN films”. *Phys. Rev. B*, **69**, 2, 1–7, 2004.

[81] S. Khlebnikov and L. P. Pryadko. “Quantum phase slips in the presence of finite-range disorder”. *Phys. Rev. Lett.*, **95**, 10, 1–4, 2005.

[82] J. M. Graybeal, P. M. Mankiewich, R. C. Dynes and M. R. Beasley. “Apparent Destruction of Superconductivity in the Disordered One-Dimensional Limit”. *Phys. Rev. Lett.*, **59**, 23, 2697–2700, 1987.

[83] H. Ebisawa, H. Fukuyama and S. Maekawa. “Superconducting Transition Temperature of Dirty Thin Films in Weakly Localized Regime”. *J. Phys. Soc. Japan*, **54**, 6, 2257–2268, 1985.

[84] J. Fenton, C. Webster and P. Warburton. “Materials for superconducting nanowires for quantum phase-slip devices”. In “Condens. Matter Mater. Phys. Conf.”, volume 012024, pages 1–3. 2011.

[85] L. Dumoulin et al. “Nb-Si thin films as thermometers for low temperature bolometers”. *J. Low Temp. Phys.*, **93**, 3-4, 301–306, 1993.

[86] A. Pourret et al. “Observation of the Nernst signal generated by fluctuating Cooper pairs”. *Nat. Phys.*, **2**, October, 2006.

[87] S. P. Chockalingam et al. “Superconducting properties and Hall effect of epitaxial NbN thin films”. *Phys. Rev. B - Condens. Matter Mater. Phys.*, **77**, 21, 2008.

[88] D. M. Glowacka et al. “Development of a NbN Deposition Process for Superconducting Quantum Sensors”. *Submitt. to arXiv*, page 4, 2014.

[89] O. Crauste et al. “Effect of annealing on the superconducting properties of a-Nb_{x}Si_{1-x} thin films”. *Phys. Rev. B*, **87**, 14, 144514, 2013.

[90] R. Cabanel, J. Chaussy, J. Geneste and J. Mazuer. “Correlations between sputtering parameters, composition and resistivity of granular NbN films.” *Thin Solid Films*, **185**, 145–150, 1990.

[91] A. Baunemann et al. “Mixed amido/imido/guanidinato complexes of niobium: potential precursors for MOCVD of niobium nitride thin films.” *Dalton Transactions*, **28**, 3715–22, 2008.

[92] A. Lichtenberger, D. Lea and F. Lloyd. “Investigation of etching techniques for superconductive Nb/Al-Al/sub 2/O/sub 3//Nb fabrication processes”. *IEEE Trans. Appiled Supercond.*, **3**, 1, 2191–2196, 1993.

[93] S. Yasin, D. G. Hasko and H. Ahmed. “Comparison of MIBK / IPA and water / IPA as PMMA developers for electron beam nanolithography”. *Microelectron. Eng.*, **62**, 745–753, 2002.

[94] H. P. Büchler, V. B. Geshkenbein and G. Blatter. “Quantum fluctuations in thin superconducting wires of finite length.” *Phys. Rev. Lett.*, **92**, 6, 067007, 2004.

[95] W. M. Roach et al. “Niobium thin film deposition studies on copper surfaces for superconducting radio frequency cavity applications”. *Phys. Rev. Spec. Top. - Accel. Beams*, **15**, 6, 1–6, 2012.

[96] D. F. Santavicca et al. “Antenna-coupled niobium bolometers for terahertz spectroscopy”. *IEEE Trans. Appl. Supercond.*, **17**, 2, 412–415, 2007.

[97] C. Nones et al. “High-impedance NbSi TES sensors for studying the cosmic microwave radiation”. *Astron. Astrophys.*, **17**, 1–6, 2012.

[98] Y. Atik et al. “Characterization of NbSi TES on a 23-pixel array”. *IEEE Trans. Appl. Supercond.*, **19**, 3, 481–483, 2009.

[99] J. S. Lehtinen, K. Zakharov and K. Y. Arutyunov. “Coulomb Blockade and Bloch Oscillations in Superconducting Ti Nanowires”. *Phys. Rev. Lett.*, **109**, 18, 187001, 2012.

[100] L. Ponta, A. Carbone and M. Gilli. "Resistive transition in disordered superconductors with varying intergrain coupling". *Supercond. Sci. Technol.*, **24**, 1, 2011.

[101] F. Smits. "Measurement of Sheet Resistivities With the 4-Point Probe". *Bell Syst. Tech. J.*, pages 711–718, 1958.

[102] R. Schneider, A. G. Zaitsev, D. Fuchs and H. V. Löhneysen. "Superconductor-Insulator Quantum Phase Transition in Disordered FeSe Thin Films". *Phys. Rev. Lett.*, **108**, 25, 257003, 2012.

[103] S. A. Wolf. "Properties of superconducting rf sputtered ultrathin films of Nb". *J. Vac. Sci. Technol.*, **13**, 1976, 145, 1976.

[104] J. Simonin. "Surface term in the superconductive Ginzburg-Landau free energy: Application to thin films". *Phys. Rev. B*, **33**, 11, 7830–7832, 1986.

[105] W. M. Chen. "Nanosuperconductor YBa 2 Cu 3 O y". *Supercond. Sci. Technol.*, **13**, 580–583, 2000.

[106] M. D. Stewart et al. "Enhanced suppression of superconductivity in amorphous films with nano-scale patterning". *Phys. C*, **469**, 13, 774–777, 2009.

[107] C. A. Marrache-Kikuchi et al. "Thickness-tuned superconductor-insulator transitions under magnetic field in a-NbSi". *Phys. Rev. B - Condens. Matter Mater. Phys.*, **78**, 14, 1–6, 2008.

[108] B. P. Martin, editor. *New Frontiers in Superconductivity Research.* Nova Science Publishers Inc, 2006.

[109] M. Chand et al. "Phase diagram of the strongly disordered s-wave superconductor NbN close to the metal-insulator transition". *Phys. Rev. B - Condens. Matter Mater. Phys.*, **85**, 1, 2012.

[110] J. Yong et al. "Robustness of the Berezinskii-Kosterlitz-Thouless transition in ultrathin NbN films near the superconductor-insulator transition". *Phys. Rev. B - Condens. Matter Mater. Phys.*, **87**, 18, 1–8, 2013.

[111] H. van der Zant, J. Jongste, H. Zandbergen and J. Mooij. "Thin amorphous superconducting niobium-silicon films with high normal state resistivity". *Phys. B*, **165-166**, 1525–1526, 1990.

[112] S. Ezaki et al. "Localization and interaction effects in ultrathin epitaxial NbN superconducting films". *J. Phys. Condens. Matter*, **24**, 47, 475702, 2012.

[113] N. A. H. K. Rao, J. C. Garland and D. B. Tanner. "Thermodynamic transition of small superconducting particles", 1984.

[114] M. Hajenius et al. "Low noise NbN superconducting hot electron bolometer mixers at 1.9 and 2.5 THz". *Supercond. Sci. Technol.*, **17**, 5, S224–S228, 2004.

[115] M. Mondal et al. "Enhancement of the finite-frequency superfluid response in the pseudogap regime of strongly disordered superconducting films." *Sci. Rep.*, **3**, 1357, 2013.

[116] A. D. Semenov, G. N. Gol'tsman and A. A. Korneev. "Quantum detection by current carrying superconducting film". *Phys. C Supercond. its Appl.*, **351**, 4, 349–356, 2001.

[117] D. E. Prober, M. D. Feuer and N. Giordano. "Fabrication of 300-Åmetal lines with substrate-step techniques". *Appl. Phys. Lett.*, **37**, 1980, 94–96, 1980.

[118] A. Rogachev and A. Bezryadin. "Superconducting properties of polycrystalline Nb nanowires templated by carbon nanotubes". *Appl. Phys. Lett.*, **83**, 3, 512–514, 2003.

[119] M. Zgirski, K. P. Riikonen, V. Touboltsev and K. Y. Arutyunov. "Quantum fluctuations in ultranarrow superconducting aluminum nanowires". *Phys. Rev. B*, **77**, October 2007, 1–6, 2008.

[120] Y. Korneeva et al. "New generation of nanowire NbN superconducting single-photon detector for mid-infrared". *IEEE Trans. Appl. Supercond.*, **21**, 3 PART 1, 323–326, 2011.

[121] J. S. Lehtinen. "Quantum fluctuations in superconducting nanostructures". Ph.D. thesis, University of Jyvaskyla, 2014.

[122] B. Cord. "Achieving sub-10-nm resolution using scanning electron beam lithography". *PhD Thesis MIT*, 2009.

[123] F. Marsili et al. “Single-photon detectors based on ultranarrow superconducting nanowires”. *Nano Lett.*, **11**, 5, 2048–2053, 2011.

[124] M. Remeika and a. Bezryadin. “Sub-10 nanometre fabrication: molecular templating, electron-beam sculpting and crystallization of metallic nanowires”. *Nanotechnology*, **16**, 8, 1172–1176, 2005.

[125] D. Meidan, Y. Oreg and G. Refael. “Sharp Superconductor-Insulator Transition in Short Wires”. *Phys. Rev. Lett.*, **98**, 18, 1–4, 2007.

[126] G. C. Tettamanzi et al. “Superconducting transition in Nb nanowires fabricated using focused ion beam.” *Nanotechnology*, **20**, 46, 465302, 2009.

[127] L. Zhou, A. A. Khajetoorians, J. Wiebe and R. Wiesendanger. “Superconductivity of lanthanum revisited: enhanced critical temperature in the clean limit”. *J. Phys. Condens. Matter*, **425703**, 1–11, 2014.

[128] J. K. W. Yang, V. Anant and K. K. Berggren. “Enhancing etch resistance of hydrogen silsesquioxane via postdevelop electron curing”. *J. Vac. Sci. Technol. B Microelectron. Nanom. Struct.*, **24**, 6, 3157, 2006.

[129] F. Marsili et al. “Cavity-Integrated Ultra-Narrow Superconducting Nanowire Single-Photon Detector Based on a Thick Niobium Nitride Film”. *Quantum Electron. Laser Sci. Conf.*, **1**, QTu3E.3, 2012.

[130] Radiall. “Technical Data Sheet Radiall PN:R284C0351026 BNC”, 2007.

[131] D. C. Mattis and J. Bardeen. “Theory of the anomalous skin effect in normal and superconducting metals”. *Phys. Rev.*, **111**, 2, 412–417, 1958.

[132] R. L. Kautz. “Noise, chaos, and the Josephson voltage standard”. *Reports Prog. Phys.*, **59**, 8, 935–992, 1999.

[133] M. L. Roukes et al. “Hot electrons and energy transport in metals at millikelvin temperatures”. *Phys. Rev. Lett.*, **55**, 4, 422–425, 1985.

[134] K. Xu and J. R. Heath. “Controlled Fabrication and Electrical Properties of Long Superconducting Nanowire Arrays”. *Nano Lett.*, **8**, 1, 136–141, 2008.

[135] M. Mitome. “Ultrathin specimen preparation by a low-energy Ar-ion milling method”. *J. Electron Microsc. (Tokyo).*, **62**, 2, 321–326, 2013.

[136] T. Kanayama, H. Tanoue and T. Tsurushima. “Formation Kinetics of Niobium and Molybdenum Silicides Induced by Ion Bombardment”. *Jpn. J. Appl. Phys.*, 1984.

[137] M. T. Deng et al. “Anomalous zero-bias conductance peak in a Nb-InSb nanowire-Nb hybrid device”. *Nano Lett.*, **12**, 12, 6414–6419, 2012.